International
Progress Report

IPR-08-12

Äspö Hard Rock Laboratory

DECOVALEX III, Task 1

Modelling of FEBEX in-situ test

Coupled thermo-hydro-mechanical analys of the buffer and the rock

Lennart Börgesson
Clay Technology AB

Jan Hernelind
FEM-Tech AB

Jan-Erik Ludvigsson
Geosigma AB

January 2004

Svensk Kärnbränslehantering AB
Swedish Nuclear Fuel
and Waste Management Co

Box 250, SE-101 24 Stockholm
Phone +46 8 459 84 00

Äspö Hard Rock
Laboratory

Report no.
IPR-08-12
No.
F84K
Author
Lennart Börgesson
Jan Hernelind
Jan-Erik Ludvigsson
Date
January 2004
Checked by
Rolf Christiansson
Date
2008-06-10
Approved
Anders Sjöland
Date
2008-06-17

Äspö Hard Rock Laboratory

DECOVALEX lll, Task 1

Modelling of FEBEX in-situ test

Coupled thermo-hydro-mechanical analys of the buffer and the rock

Lennart Börgesson
Clay Technology AB

Jan Hernelind
FEM-Tech AB

Jan-Erik Ludvigsson
Geosigma AB

January 2004

Keywords: Thermal, Hydraulic, Mechanical, Finite element, Modelling, Rock, Tunnel, Excavation, Bentonite, Buffer, Interaction

Abstract

The excavation of the test tunnel and the first 1000 days of the FEBEX experiment have been modelled in the framework of the international project DECOVALEX. The modelling has been performed in three stages where different predictive results have been requested and organized as Tasks A, B and C. Task A concerns hydro-mechanical modelling of the rock with prediction of the effect of excavation of the FEBEX tunnel. Task B concerns thermo-hydro-mechanical prediction of the buffer material during the first 1000 days after installation. Task C concerns thermo-hydro-mechanical prediction of mainly the rock response to the installation and heating during the first 1000 days.

The authors have modelled these processes with the finite element code ABAQUS including the specially made models of water unsaturated buffer materials. The element mesh for the rock modelling in tasks A and C is a large 3D model with the dimensions 600x150x300 m^3 and for Task C divided into sub meshes with different density of elements. In ABAQUS it is possible to combine and connect two quite different element meshes, which allows building of a model with very large dimensions and yet catch the processes in small parts of the model. For Task B a special element mesh with very dense element division was used and the rock hydraulically only modelled as a boundary condition with constant water pressure.

The modelling for tasks A and C included all steps in the FEBEX experiment, i.e. the excavation, buffer and canister placement, heating of the canisters and the subsequent wetting and swelling of the buffer material, temperature increase and mechanical and hydraulic response in the rock. The water pressure, temperature and displacements in the rock have been measured in some points and the results were compared with the measurements.

The predictions and comparisons with measurements of the **rock behaviour** yielded the following results:

The temperature predictions were as expected very good. It is generally known that temperature is rather easy to predict.

The hydraulic predictions were not so good although the change in water pressure in the near field rock was well predicted. The main reason for the discrepancy is that the measured initial water pressure before installation of the buffer was lower than could be achieved with the modelling. The conclusion is that there is a skin effect with different properties in the rock boundary around the drift that is not included in the model. Another small discrepancy was that the predicted reduction in water pressure of between 50 and 300 kPa in the boreholes during the first months was not observed in the measurements. The reasons for the latter discrepancy can be e.g.

- a difference in behaviour of the modelled and real contact between the buffer and the rock. The negative pore pressure in the buffer might not be distributed to the rock if the water flow in the rock mainly takes place in fractures instead of in the rock matrix as modelled

- a delayed rock/buffer interaction caused by the slot between the rock and the buffer

- measurement problems that may be induced by the large water volume and possible air pockets between the packers in the boreholes

The results of the mechanical predictions are ambiguous. The range in predicted change of total stress in the near field rock is in good agreement with the range of measured stress but the correlation between prediction and measurement in the specific points are poor. There are two possible main reasons for the discrepancies and both are probably part of the explanation:

- The rock model is not accurate enough, since the real rock structure is more complicated than the model.
- It is difficult to measure stresses and strains in rock and the results may be unreliable

The modellings of the **buffer behaviour** were mainly done for task B but also included in task C. They showed that the thermo-hydro-mechanical predictions agreed rather well with measurements in both models. The following conclusions can thus be drawn:

- The influence of the rock on the wetting of the buffer is insignificant, which means that the rock provides the buffer with the required water flow but also that the water pressure built up in the rock/buffer interface is not so high that it influences the wetting. The reason is that the hydraulic conductivity is much higher in the rock than in the buffer and that the overall water pressure in the rock is low compared to the suction in the buffer.
- The fair agreement in results between the large integrated model and the specific buffer model showed that the buffer and near field rock processes can be captured in a large model, thanks to the ability of the code ABAQUS to connect structures with different element mesh and element density.

Sammanfattning

Borrningen av försökstunneln och de första 1000 dagarna av FEBEX-försöket har modellerats inom ramen för det internationella projektet DECOVALEX. Modelleringen har gjorts i tre stadier där olika predikteringar har efterfrågats och organiserats som uppgifer (Task A, B och C). Task A innebar hydro-mekanisk modellering av berget med prediktion av responsen på tunneldrivningen. Task B innebar termo-hydro-mekanisk prediktion av buffertens funktion under de första 1000 dagarna efter installationen. Task C innebar termo-hydro-mekanisk prediktion av i huvudsak bergets respons på installationen och uppvärmningen under de första 1000 dagarna.

Författarna har modellerat dessa processer med finita-element-programmet ABAQUS som även innehåller de specialgjorda materialmodellerna för vattenomättade buffertmaterial. Elementnätet för bergmodelleringen i Task A och C är en stor 3D-modell med dimensionerna 600x150x300 m^3. Nätet har i Task C uppdelats i undernät med olika elementtäthet. I ABAQUS är det möjligt att kombinera och sätta samman två helt olika elementnät, vilket gör det möjligt att bygga en modell med mycket stora dimensioner och likväl fånga processerna i små delar av modellen. För Task B gjordes en specialmodell med mycket tät elementindelning och berget modellerades hydrauliskt enbart som ett randvillkor med konstant vatatentryck.

Modelleringen av THM-processerna i **berget** och jämförelser med uppmätta värden gav följande resultat:

Som förväntat var temperaturprediktionerna bra. Det är väl känt att det i allmänhet är tämligen enkelt att prediktera temperatur.

De hydrauliska prediktionerna var inte lika bra, även om prediktionerna av förändringen i vattentryck i närfältberget var goda. Huvudskälet till diskrepansen är att det mätta ursprungliga vattentrycket före installationen av bufferten var lägre än vad som erhölls vid modelleringen. Slutsatsen är att det finns en närzon i bergytan runt orten med andra egenskaper, som inte är modellerad. Ytterligare en mindre diskrepans är att den predikterade minskningen av vattentrycket på mellan 50 och 300 kPa i berget under de första månaderna inte hade observerats i mätningarna. Anledningarna till det senare kan vara flera, t.ex.

- en skillnad mellan modellerad och verklig kontakt mellan buffert och berg. Det negativa portrycket i bufferten kanske inte sprider sig till berget om vattenflödet i berget huvudsakligen äger rum i sprickor istället för i bergmatrisen såsom modellerats
- att samverkan berg/buffert försenas p.g.a. av spalten mellan berget och bufferten
- mätproblem som kan ha uppstått p g a den stora vattenvolymen och eventuella luftfickor mellan packers i borrhålen

Resultaten från de mekaniska prediktionerna är tvetydiga. Storleken hos den predikterade ändringen av totalspänningen i närfältberget överensstämmer väl med uppmätta spänningar, men korrelationen mellan predikterade och uppmätta spänningar i de specifika punkterna är svag. Det finns två möjliga huvudorsaker till diskrepanserna, och troligtvis är förklaringen delvis att finna i båda:

- Bergmodellen är inte tillräckligt detaljerad eftersom verkliga bergstrukturen är mer komplicerad än i modellen
- Det är svårt att mäta spänningar och töjningar i berg och resultaten kan vara otillförlitliga

Modelleringen av THM-processerna i **bufferten** gjordes i huvudsak i Task B men var även inkluderade i Task C. Resultaten visade att prediktionerna stämde väl överens med mätningarna för båda modellerna. Följande slutsatser kunda alltså dras:

- Inverkan av berget på bevätningen av buffereten är insignifikant, vilket betyder att berget förser bufferten med erforderligt vatenflöde men också att vattentrycks-uppbyggnaden i berg/buffert kontakten inte är så hög att den påverkar bevätningen. Orsaken är hydrauliska konduktiviteten är mycket högre i berget än i bufferten och att det totala vattentrycket i berget är lågt i jämförelse med sugpotentialen i buffereten.
- Modellering av THM-processerna i bufferten kan göras med relativt stor tillförlitlighet under de villkor som råder i FEBEX, dvs en buffert utan stora spalter och ett berg som förser buffereten med erforderligt vatten.
- Den hyggliga överensstämmelsen mellan resultaten från den stora integrerade modellen och den specifika buffertmodellen visade att processerna i buffereten och närfältsberget kan fångas i en stor modell tack vare möjligheten i ABAQUS att förbinda strukturer med olika elementnät och elementtäthet.

Contents

1 Introduction

Measurement results from some of large scale field tests have been submitted to the international project DECOVALEX III (DEvelopment of COupled models and their VALidation against EXperiments) in order to get an experimental basis for developing and testing coupled models describing Thermo-Hydro-Mechanical (THM) processes. DECOVALEX III Task 1 includes a full-scale field test of a deposition tunnel in the Grimsel Test Site in Switzerland. The test is named FEBEX and is conducted by ENRESA for testing the Spanish concept for nuclear waste disposal in crystalline rock.

The exercise of Task 1 was to predict the performance of the buffer material and the near field rock during the first 1000 days of the test period. In order to make the calculations stepwise and to understand the rock behaviour the predictions have been divided into the following 3 parts /1-1/:

Part A. Hydro-mechanical modelling of the rock.

Prediction of the hydro-mechanical effect of drilling the test tunnel before installation of the buffer.

Part B. Thermo-hydro-mechanical analyses of the bentonite behaviour.

Prediction of the thermal, hydraulic, and mechanical response of the bentonite barrier from the heating of the simulated canisters and the wetting from the rock, but without considering the hydraulic behaviour of the rock.

Part C. Thermo-hydro-mechanical analyses of the rock.

Prediction of the thermal, hydraulic, and mechanical response of the rock from the heating, the swelling pressure and flow resistance or suction of the bentonite.

The tasks are described in reports provided by ENRESA and UPC /1-1, 1-2, 1-3/.

2 FEBEX in-situ test

2.1 General

The FEBEX (Full-scale Engineered Barriers Experiment in Crystalline Host Rock) project is a multinational project that is co-financed by the European commission and ENRESA. Phase 1 of the project lasted from 1994 to 2001. The test was installed at the Grimsel Test Site, an underground laboratory in Switzerland operated by NAGRA. The experiment is based on the Spanish reference concept of deep geological storage in crystalline host rock. In this concept, steel canisters containing the conditioned waste are placed along the axis of horizontal galleries drilled in a rock formation and an engineered barrier, made of high density compacted bentonite blocks, is placed in the annular space left /2-1/.

2.2 Site description

The Test Site is located at an elevation of 1730 m above sea level, around 450 m beneath the Juchlistock mountain in the granitic rocks of the Aare Massif in central Switzerland. The ion concentration n in the ground water is thus very low and does not need to be considered.

The Grimsel Test Site (GTS tunnel) is located in a tunnel system, which branches off from the main access tunnel (KWO tunnel) to the underground power station of the KWO (Kraftwerke Oberhasli AG). The GTS tunnel (also named the Laboratory tunnel) has a diameter of 3.5 m and a length of almost 1000 m. It was excavated in 1983.

Figure 2-1 shows the Grimsel Test Site area and the different experiments running. The location of the FEBEX tunnel is also shown /2-1/.

Extensive characterisation of the rock has been done. The structure and hydrology of the rock will be described in chapter 5.

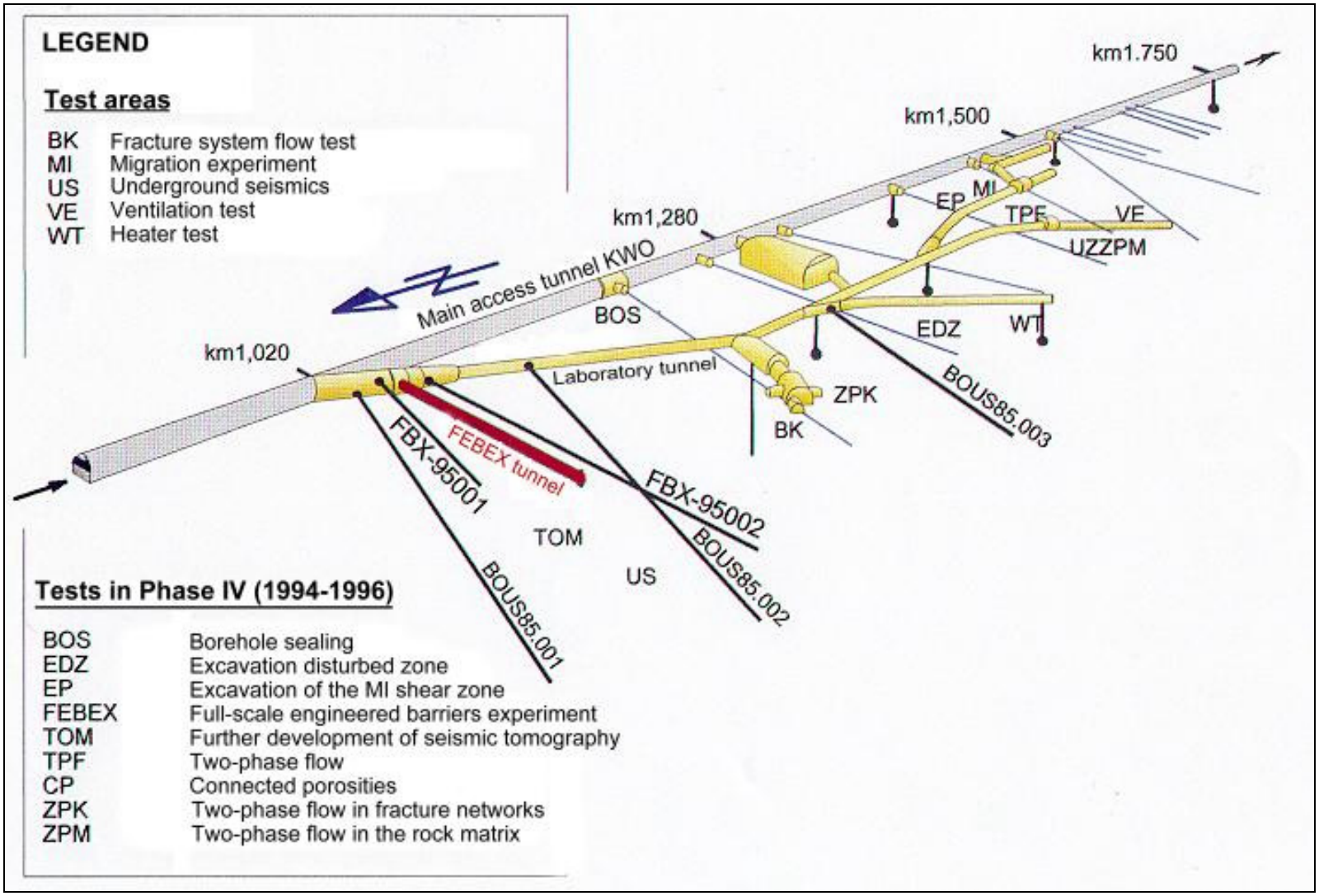

Figure 2-1. *Grimsel Test Site area and location of the FEBEX test /2-1/.*

2.3 Test layout

A brief summary of the test will be given /2-1/.

The FEBEX tunnel has the diameter 2.28 m and the length 71.4 m. It was drilled with a tunnel boring machine in September and October 1995. The FEBEX test is performed in the inner 20 meters of the drift. The test, which is shown in Figure 2-2, consists of two 4.54 m long heaters embedded by a buffer material of high density compacted bentonite blocks. The canisters are enclosed in a perforated steel liner for installation reasons. Outside the buffer material 17 m from the end of the drift a concrete plug is built. Altogether 632 instruments are placed in the rock, bentonite and heaters. The heaters are heated with a power that is regulated to yield a maximum temperature of 100 degrees in the buffer. Figure 2-3 shows the test with the measuring sections.

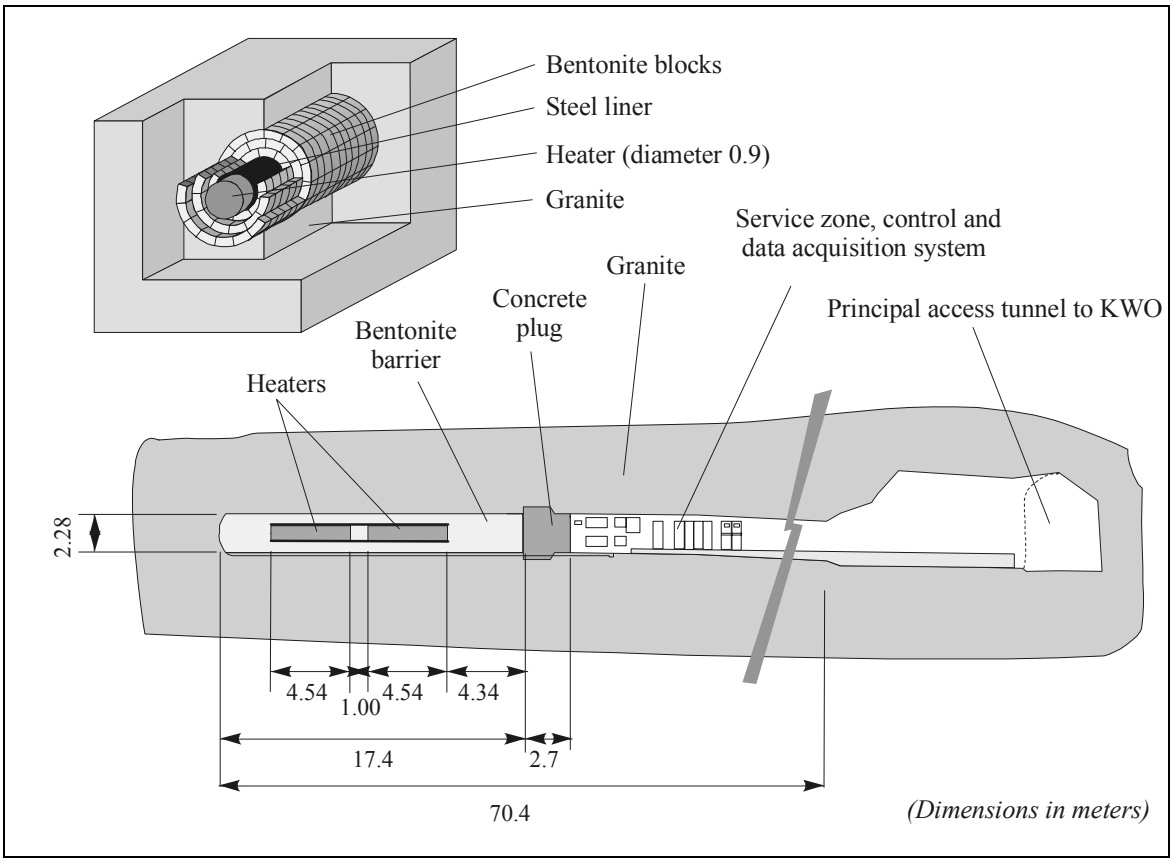

Figure 2-2. *Overview of the FEBEX test* /2-1/.

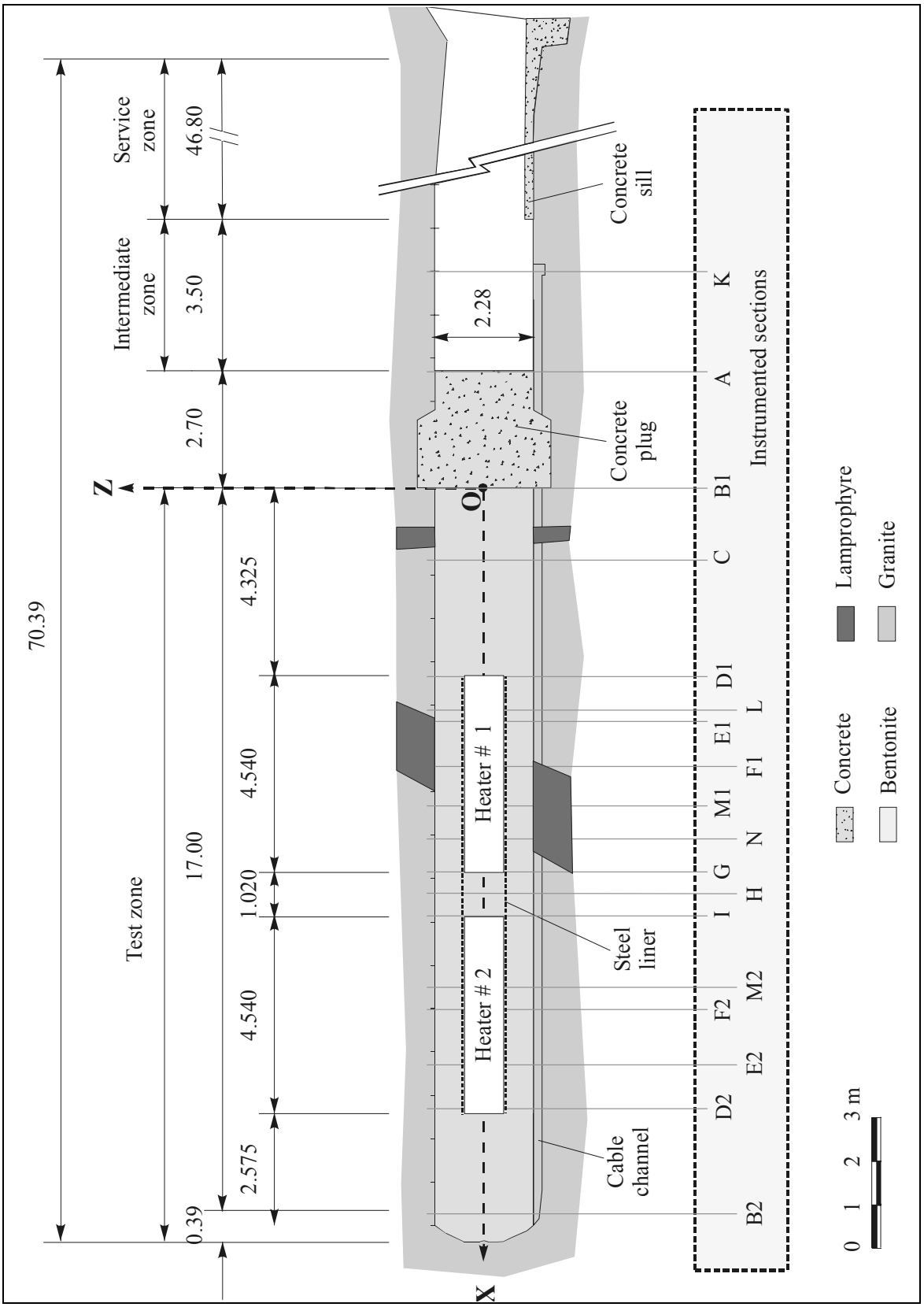

Figure 2-3. *Test site with dimensions and measuring sections* /2-1/.

3 Description of tasks

3.1 Introduction

The project was divided into three different parts with different tasks.

Part A implied the task to formulate a hydro-geological model of the rock and to perform a simulation of the excavation of the FEBEX drift. The hydraulic response of the excavation in terms of pore water pressure changes in the rock and seepage into the drift was to be predicted.

Part B implied modelling of the thermo-hydro-mechanical behaviour of the buffer material with prediction of the development of temperature, stress and relative humidity with time in some points where transducers had been installed. Since only the buffer and canister were included in the model, the rock was assumed to act as a mechanically stiff boundary with the water pressure 0, i.e. unlimited water available at the buffer boundary. The rock was only included in the temperature calculation.

For part C the task was to model the integrated THM function of the rock, the buffer and the canisters.

3.2 Description of PART A: Hydro-mechanical modelling of the rock before test installation

Part A implied the task to create a hydro-geological model of the rock and to perform a simulation of the excavation of the FEBEX drift. The hydraulic response of the excavation in terms of pore water pressure changes in the rock and seepage into the drift were to be predicted.

The following work and results were accomplished:

- Identification and characterisation the most important geological features to be included in hydrogeological models of the FEBEX site scale and –experimental scale and description of the overall piezometric head conditions together with suggested initial conditions for the modelling.
- Preparation of a hydro-mechanical model of the host rock near the FEBEX tunnel with a description of the model and the calibrations made for the model.
- Prediction of the total water inflow into the test part of the tunnel. The predicted inflow 100 days after start of the excavation was requested.
- Prediction of the pore water response during the excavation of the tunnel. The water pressure in two measuring sections (3 and 4) in the borehole FEBEX-95002 (see chapter 5) as a function of time during the excavation and 14 days after was requested. The borehole runs parallel to the FEBEX tunnel at the distance about 3.8 m from the centre of the tunnel. Section 4 is located 50-61 m from the drift opening and section 3 is located 62-74 m from the drift opening.

3.3 Description of PART B: Thermo-hydro-mechanical modelling of the buffer material after test installation

The requirement of part B was to predict the THM processes during the first 1000 days of the experiment without considering the hydraulic properties of the rock. The following results were requested (the sections refer to Figure 2-3):

- Evolution of the heating power of both heaters as a function of time
- Distribution of relative humidity in radial direction in three sections (E1, H and E2) at four different times
- Distribution of relative humidity in axial direction along two lines (LG1 at the radius 1.08 m and RC1 at the radius 0.81 m) at two times
- Evolution of relative humidity with time at three points in sections H1 and H
- Distribution of temperature in radial direction in two sections (D1 and G) at two different times
- Distribution of temperature in axial direction along two lines (LG1 and RC1) at two times
- Evolution of temperature with time at one point in sections D1 and G
- Evolution of total stress with time at three points in section E2 and one point in section B2

3.4 Description of PART C: Thermo-hydro-mechanical analysis of the rock after test installation

3.4.1 General

The Task of part C was to predict temperature, water pressure, total stress and displacement results in specified points in the rock. These points correspond to locations of gauges installed in boreholes in the rock around the test drift.

A three-dimensional view of all the boreholes drilled is shown in Figure 3-1 /1-1/. A Cartesian co-ordinate system is also shown. The origin is located at the intersection of the tunnel axis and the contact plane between the concrete plug and the bentonite buffer. Positive X axis is directed along the tunnel axis towards the other end of the test section. The Z axis is vertical, pointing upwards and the Y axis is perpendicular to the X-Z plane in the position as indicated in Figure 3-1.

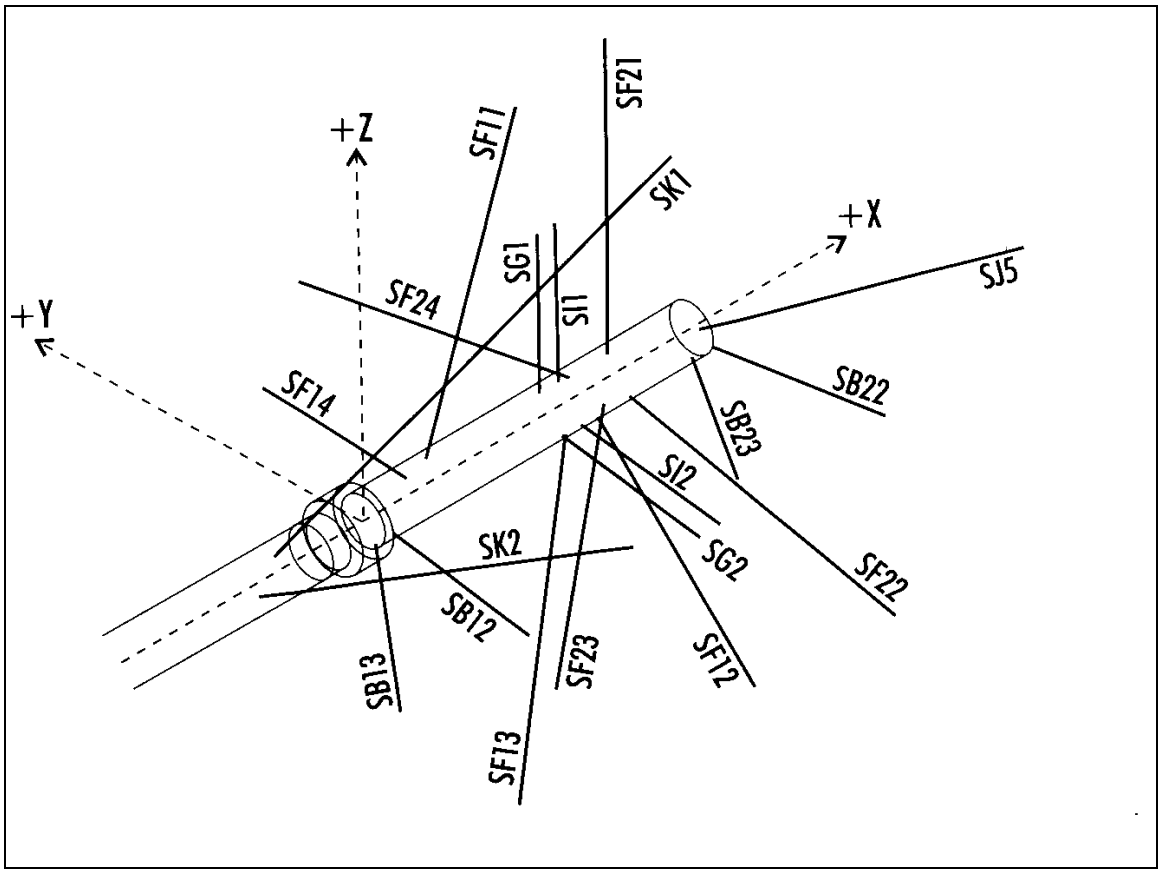

Figure 3-1. *Borehole layout and Cartesian co-ordinate system /1-1/.*

Four types of history results were requested /1-3/. They refer to:

- Evolution (in time) of temperature (T) in selected points at increasing radial distance.
- Evolution of water pressure (p_w) in selected points at increasing radial distance.
- Evolution of normal stresses (σ_r, σ_θ, σ_x) in selected points at increasing radial distance.
- Evolution of radial displacements (u_r) in selected points at increasing radial distance.

In addition to those results the distribution of water pressure, (p_w), along different radii for three selected times were also requested.

3.4.2 Evolution of temperature at selected points

The evolution of temperature with time, in the period (Day 0 – Day 1000) was requested in the following boreholes and points:

Borehole SF21 (borehole entry located at X = 12.65 m)

Point	Sensor coordinates (m)		
	X	Y	Z
1	12.65	-0.08	1.21
2	12.67	-0.09	2.63
3	12.70	-0.13	4.97
4	12.73	-0.19	12.93

Borehole SF22 (borehole entry located at X = 12.64 m)

Point	Sensor coordinates (m)		
	X	Y	Z
1	12.64	-1.40	-0.38
2	12.60	-2.93	-0.73
3	12.49	-9.26	-2.19
4	12.43	-12.67	-3.00

3.4.3 Evolution of water pressure at selected points

The evolution of water pressure with time in the period (Day 0 – Day 1000) was requested in the following boreholes and points:

Borehole SF21 (borehole entry located at X = 12.65 m)

Point	Sensor coordinates (m)		
	X	Y	Z
1	12.67	-0.10	3.03
2	12.71	-0.15	8.18
3	12.72	-0.20	13.58

Borehole SF22 (borehole entry located at X = 12.64 m)

Point	Sensor coordinates (m)		
	X	Y	Z
1	12.56	-5.34	-1.29
2	12.47	-10.21	-2.42
3	12.41	-13.38	-3.17

Borehole SF23 (borehole entry located at X = 12.64 m)

Point	Sensor coordinates (m)		
	X	Y	Z
1	12.59	0.82	-5.21
2	12.54	1.50	-9.07
3	12.49	2.10	-12.50

Borehole SF24 (borehole entry located at X = 12.01 m)

Point	Sensor coordinates (m)		
	X	Y	Z
1	12.06	5.11	-1.05
2	12.16	11.51	-2.17

3.4.4 Evolution of normal stresses (σr, σ_θ, σx) at selected points

The evolution of three normal components of stress in the period (Day 0 – Day 1000) was required at the following points:

Borehole SG1 (borehole entry located at X = 9.13 m)

Point	Stress	Sensor coordinates (m)		
		X	Y	Z
1	σ_x	9.14	-0.06	2.42
2	σ_θ	9.14	-0.06	2.80
3	σ_r	9.14	-0.06	3.08
4	σ_x	9.23	-0.01	7.22
5	σ_θ	9.24	0.00	7.59
6	σ_r	9.25	0.00	7.87

Borehole SG2 (borehole entry located at X = 9.13 m)

Point	Stress	Sensor coordinates (m)		
		X	Y	Z
1	σ_x	9.14	-2.54	-0.55
2	σ_θ	9.14	-2.91	-0.62
3	σ_r	9.15	-3.18	-0.67
4	σ_x	9.20	-6.24	-1.27
5	σ_θ	9.21	-6.63	-1.35
6	σ_r	9.21	-6.98	-1.41

3.4.5 Evolution of radial displacements (ur) at selected points

The evolution of radial displacements in the period (Day 0 – Day 1000) was required at the following points:

Borehole SI1 (borehole entry located at X = 10.14 m)

Point	Anchor coordinates (m)		
	X	Y	Z
1	10.14	-0.05	2.03
2	10.16	-0.03	4.03
3	10.19	0.03	8.03

Borehole SI2 (borehole entry located at X = 10.14 m)

Point	Anchor coordinates (m)		
	X	Y	Z
1	10.14	-2.17	-0.48
2	10.17	-4.14	-0.83
3	10.23	-8.08	-1.53

3.4.6 Distribution of water pressure (pw) along different radii for three selected times

The distribution of water pressure along boreholes SF21, SF22, SF23 and SF24 (see Figure 3-1) was required at the following times:

Time	days
T1	100
T2	600
T3	1000

4 Finite element code

4.1 General

The finite element code ABAQUS was used for the calculations. ABAQUS contains a capability of modelling a large range of processes in many different materials as well as complicated three-dimensional geometry.

The code includes special material models for rock and soil and ability to model geological formations with infinite boundaries and in situ stresses by e.g. the own weight of the medium. It also includes capability to make substructures with completely different finite element meshes and mesh density without connecting all nodes. This technique has been used in the calculations for task C. Detailed information of the available models, application of the code and the theoretical background is given in the ABAQUS Manuals /4-1/.

4.2 Hydro-mechanical analyses in ABAQUS

The hydro-mechanical model consists of porous medium and wetting fluid and is based on equilibrium, constitutive equations, energy balance and mass conservation using the effective stress theory.

Equilibrium

Equilibrium is expressed by writing the principle of virtual work for the volume under consideration in its current configuration at time *t*:

$$\int_V \boldsymbol{\sigma} : \delta\boldsymbol{\varepsilon}\, dV = \int_S \mathbf{t} \cdot \delta\mathbf{v}\, dS + \int_V \hat{\mathbf{f}} \cdot \delta\mathbf{v}\, dV, \qquad (4\text{-}1)$$

where $\delta\mathbf{v}$ is a virtual velocity field, $\delta\boldsymbol{\varepsilon} \overset{def}{=} sym\left(\partial\delta\mathbf{v}/\partial\mathbf{x}\right)$ is the virtual rate of deformation, $\boldsymbol{\sigma}$ is the true (Cauchy) stress, $\mathbf{t}$ are the surface tractions per unit area, and $\hat{\mathbf{f}}$ are body forces per unit volume. For our system, $\hat{\mathbf{f}}$ will often include the weight of the wetting liquid,

$$\mathbf{f}_w = S_r n \rho_w \mathbf{g}, \qquad (4\text{-}2)$$

where S_r is the degree of saturation, n the porosity, ρ_w the density of the wetting liquid and $\mathbf{g}$ is the gravitational acceleration, which we assume to be constant and in a constant direction (so that, for example, the formulation cannot be applied directly to a centrifuge experiment unless the model in the machine is small enough that g can be treated as constant). For simplicity we consider this loading explicitly so that any other gravitational term in $\hat{\mathbf{f}}$ is only associated with the weight of the dry porous medium. Thus, we write the virtual work equation as

$$\int_V \boldsymbol{\sigma} : \delta\boldsymbol{\varepsilon} dV = \int_s \mathbf{t} \cdot \delta\mathbf{v} dS + \int_V \mathbf{f} \cdot \delta\mathbf{v} dV + \int_V S_r n \rho_w \mathbf{g} \cdot \delta\mathbf{v} dV, \qquad (4\text{-}3)$$

where $\mathbf{f}$ are all body forces except the weight of the wetting liquid.

The simplified equation used in ABAQUS for the effective stress is:

$$\overline{\boldsymbol{\sigma}}^{*} = \boldsymbol{\sigma} + \chi\, u_{\mathrm{w}}\mathbf{I}. \qquad (4\text{-}4)$$

where $\boldsymbol{\sigma}$ is the total stress, u_w is the pore water pressure, χ is a function of the degree of saturation (usual assumption $\chi = S_r$), and $\mathbf{I}$ the unitary matrix.

Energy balance

The conservation of energy implied by the first law of thermodynamics states that the time rate of change of kinetic energy and internal energy for a fixed body of material is equal to the sum of the rate of work done by the surface and body forces. This can be expressed as (not considering the thermal part, which is solved as uncoupled heat transfer; cf Equation 4-15):

$$\frac{\mathrm{d}}{\mathrm{dt}}\int_{\mathrm{V}}\left(\tfrac{1}{2}\rho\mathbf{v}\cdot\mathbf{v}+\rho\mathrm{U}\right)\mathrm{dV} = \int_{\mathrm{s}}\mathbf{v}\cdot\mathbf{t}\,\mathrm{dS}+\int_{\mathrm{V}}\mathbf{f}\cdot\mathbf{v}\,\mathrm{dV} \qquad (4\text{-}5)$$

where

ρ is the current density,

$\mathbf{v}$ is the velocity field vector,

U is the internal energy per unit mass,

$\mathbf{t}$ is the surface traction vector,

$\mathbf{f}$ is the body force vector, and

Constitutive equations

The constitutive equation for the solid is expressed as:

$$d\boldsymbol{\tau}^{\mathrm{c}} = \mathbf{H} : d\boldsymbol{\varepsilon} + \mathbf{g}, \qquad (4\text{-}6)$$

where $d\boldsymbol{\tau}^{\mathrm{c}}$ is the stress increment, $\mathbf{H}$ the material stiffness, $d\boldsymbol{\varepsilon}$ the strain increment and $\mathbf{g}$ is any strain independent contribution (e.g. thermal expansion). $\mathbf{H}$ and $\mathbf{g}$ are defined in terms of the current state, direction for straining, etc., and of the kinematic assumptions used to form the generalised strains.

The constitutive equation for the liquid (static) in the porous medium is expressed as:

$$\frac{\rho_{\mathrm{w}}}{\rho_{\mathrm{w}}^{0}} \approx 1 + \frac{\mathrm{u_w}}{\mathrm{K_w}} - \varepsilon_{\mathrm{w}}^{\mathrm{th}}, \qquad (4\text{-}7)$$

where ρ_w is the density of the liquid, ρ_{w}^{0} is its density in the reference configuration, $K_w(T)$ is the liquid's bulk modulus, and

$$\varepsilon_w^{th} = 3\alpha_w(T - T_w^0) - 3\alpha_{w|T^I}(T^I - T_w^0) \qquad (4\text{-}8)$$

is the volumetric expansion of the liquid caused by temperature change. Here $\alpha_{\mathrm{w}}(T)$ is the liquid's thermal expansion coefficient, T is the current temperature, T^{I} is the initial temperature at this point in the medium, and T_{w}^{0} is the reference temperature for the thermal expansion. Both $\mathrm{u}_{\mathrm{w}}/\mathrm{K}_{\mathrm{w}}$ and $\varepsilon_{\mathrm{w}}^{\mathrm{th}}$ are assumed to be small.

Mass conservation

The mass continuity equation for the fluid combined with the divergence theorem implies the pointwise equation:

$$\frac{1}{J}\frac{d}{dt}\left(J\rho_{\mathrm{w}}S_r n\right)+\frac{\partial}{\partial \mathbf{x}}\cdot\left(\rho_{\mathrm{w}}S_r n\mathbf{v}_{\mathrm{w}}\right)=0. \qquad (4\text{-}9)$$

where J is the determinant of the Jacobian matrix of the skeleton motion and **x** is position. The constitutive behaviour for pore fluid is governed by Darcy's law, which is generally applicable to low fluid velocities. Darcy's law states that, under uniform conditions, the volumetric flow rate of the wetting liquid through a unit area of the medium, $S_r n\mathbf{v}_w$, is proportional to the negative of the gradient of the piezometric head:

$$S_r n\mathbf{v}_{\mathrm{w}} = -\hat{\mathbf{k}}\frac{\partial\phi}{\partial \mathbf{x}}, \qquad (4\text{-}10)$$

where $\hat{\mathbf{k}}$ is the permeability of the medium and ϕ is the piezometric head, defined as:

$$\phi \overset{def}{=} \mathrm{z}+\frac{\mathrm{u}_{\mathrm{w}}}{\mathrm{g}\rho_{\mathrm{w}}} \qquad (4\text{-}11)$$

where z is the elevation above some datum and g is the magnitude of the gravitational acceleration, which acts in the direction opposite to z. $\hat{\mathbf{k}}$ can be anisotropic and is a function of the saturation and void ratio of the material. $\hat{\mathbf{k}}$ has units of velocity (length/time). [Some authors refer to $\hat{\mathbf{k}}$ as the hydraulic conductivity and define the permeability as

$$\hat{\mathbf{K}} = \frac{\nu}{g}\hat{\mathbf{k}} \qquad (4\text{-}12)$$

where ν is the kinematic viscosity of the fluid.]

We assume that g is constant in magnitude and direction, so

$$\frac{\partial\phi}{\partial \mathbf{x}} = \frac{1}{\mathrm{g}\rho_{\mathrm{w}}}\left(\frac{\partial \mathrm{u}_{\mathrm{w}}}{\partial \mathbf{x}}-\rho_w\mathbf{g}\right) \qquad (4\text{-}13)$$

Vapour flow

Vapour flow is modelled as a diffusion process driven by a temperature gradient (coded as UEL user supplied routine with stiffness and flow).

$$\mathbf{q}_v = -D_{Tv}\frac{\partial T}{\partial \mathbf{x}} \tag{4-14}$$

where $\mathbf{q}_v$ is the vapour flux and D_{Tv} the thermal vapour diffusivity.

4.3 Uncoupled heat transfer analysis

Energy balance

The basic energy balance is (neglecting mechanical contribution; cf Equation 4-5)

$$\int_v \rho \dot{U} dV = \int_s q dS + \int_v r dV \tag{4-15}$$

where V is a volume of solid material, with surface area S; ρ is the density of the material; $\dot{U}$ is the material time rate of the internal energy; q is the heat flux per unit area of the body, flowing into the body; and r is the heat supplied externally into the body per unit volume.

It is assumed that the thermal and mechanical problems are uncoupled in the sense that $U = U(T)$ only, where T is the temperature of the material, and q and r do not depend on the strains or displacements of the body. For simplicity a Lagrangian description is assumed, so ”volume” and ”surface” mean the volume and surface in the reference configuration.

Constitutive definition

The relationship is usually written in terms of a specific heat, neglecting coupling between mechanical and thermal problems:

$$c(T) = \frac{dU}{dT}, \tag{4-16}$$

Heat conduction is assumed to be governed by the Fourier law.

$$\mathbf{f}_q = -\mathbf{k}\frac{\partial T}{\partial \mathbf{x}} \tag{4-17}$$

where $\mathbf{f}_q$ is the heat flux and $\mathbf{k}$ is the heat conductivity matrix, $\mathbf{k} = \mathbf{k}(T)$. The conductivity can be fully anisotropic, orthotropic, or isotropic.

4.4 Coupling of thermal and hydro-mechanical solutions

In ABAQUS the coupled problem is solved through a ”staggered solution technique” as sketched in Figure 4-1 and below.

1. First a thermal analysis is performed where heat conductivity and specific heat are defined as functions of saturation and water content. In the first analysis these parameters are assumed to be constant and in the subsequent analyses they are read from an external file.

2. The hydromechanical model is used to calculate stresses, pore pressures, void ratios, degree of saturation etc. as function of time. Saturation and void ratio histories are written onto an external file.

3. The material parameters update module reads the file with saturation and void ratio data and creates a new file containing histories for saturation and water content2

4. . The saturation and water content histories are used by the thermal model in the following analysis.

5. Steps 1-3 are repeated if parameter values are found to be different compared to those of the previous solution.

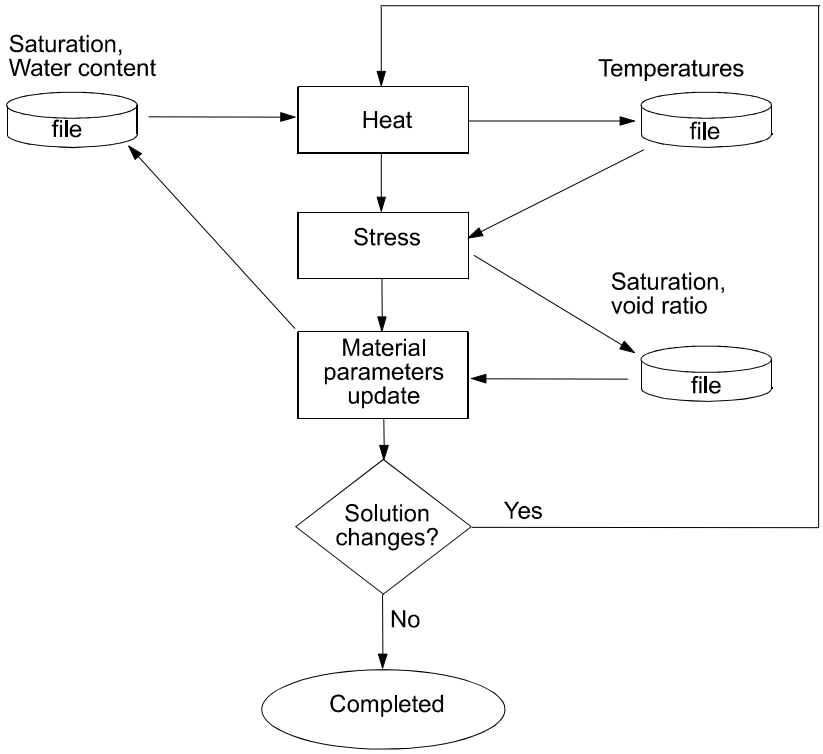

Figure 4-1. *In ABAQUS, heat transfer calculations and hydro-mechanical calculations are decoupled. By using the iteration procedure schematically shown above, the effects of a fully coupled THM model are achieved.*

5 Finite element models of the rock, buffer and other installations

5.1 General

Three different finite element models have been used for the calculations. The first model used for task A only included the rock. The second model used for task B only included the installations in the FEBEX drift. The third model included both the rock and the installations. Since the model of the rock was very similar for tasks A and C only the finite element model used for task C will be shown.

A conceptual model of the rock structure and the hydrology around the FEBEX drift has been the base for the finite element model and its properties and boundary conditions. The background and a description of the model are included as Appendix 3 in this report.

5.2 Conceptual hydro-geological model

Figure 5-1 shows the rock structure according to the conceptual model. The area around the FEBEX tunnel is intersected by 5 fractured zones. Two of them are located outside the FEBEX tunnel. Those are the “South shear zone” and the “North shear zone”. The other three intersect the FEBEX tunnel. Those are the “Shear and breccia zone” and two “Lamprophyre dykes”.

Figure 5-1 also shows the location of the KWO, GTS, and FEBEX tunnels and four boreholes used to characterise the area (FEBEX and BOUS holes).

Proper limits of the model are the “South and North shear zones”, the KWO tunnel and a southwest boundary about 100 m away from the FEBEX tunnel. Since all zones are sub vertical a proper simplification is to model all zones and boundaries vertical.

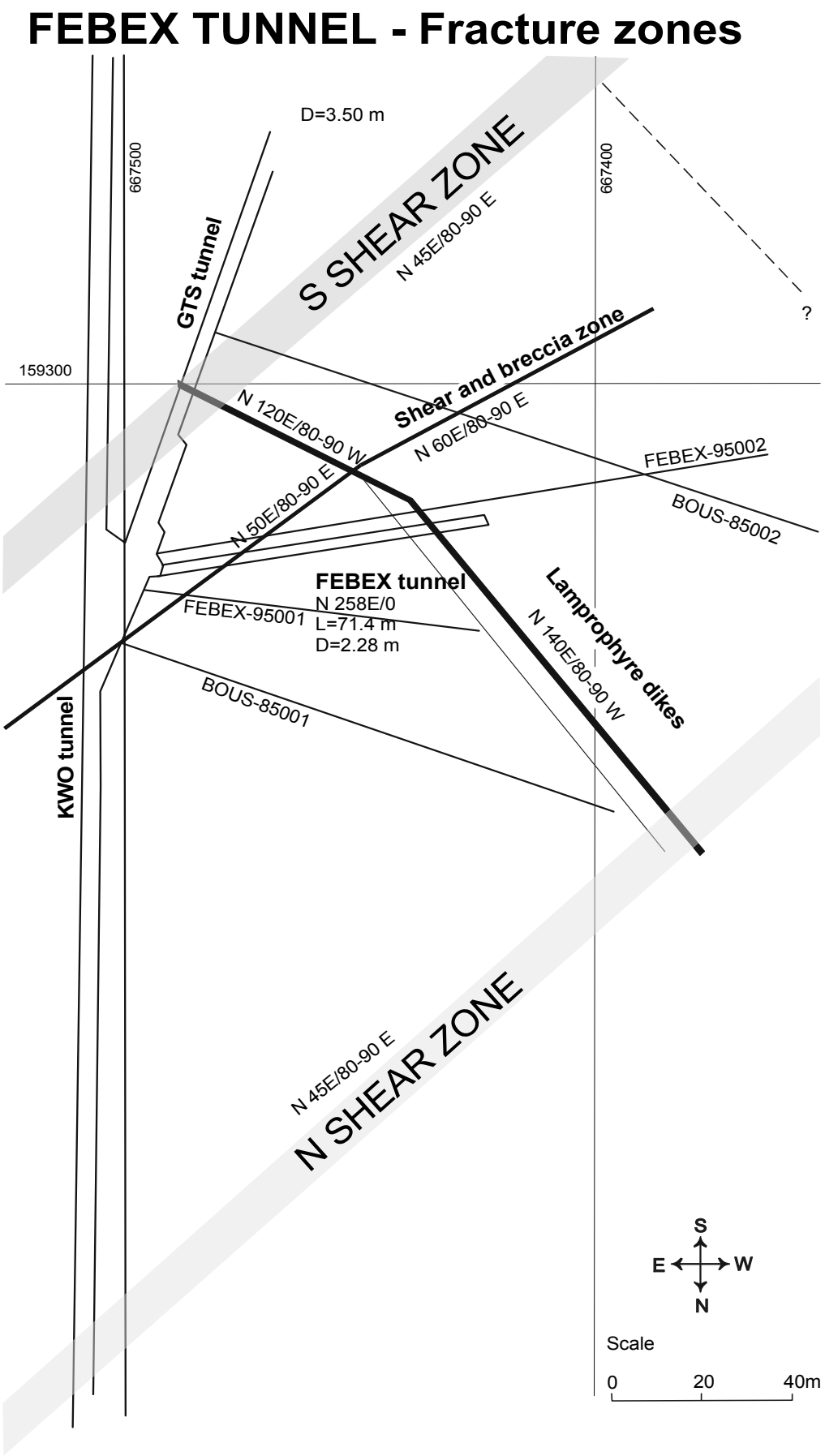

Figure 5-1. *Conceptual model of the rock structure (Appendix 3).*

5.3 Finite element model of mainly the rock for tasks A and C

5.3.1 Element mesh

The finite element model of the rock was built with the conceptual model as basis. The element mesh is very large in dimensions and rather complicated, since it includes the installations in the ZEDEX drift and a refined element mesh of the near field rock. The mesh consists of three structures:

- The outer rock (the main structure) with the dimensions 600x150x300 m^3
- The near-field rock (first substructure) with the dimensions 30x30x70 m^3
- The FEBEX tunnel with all installations (second substructure) with the diameter D=2.2 and length L=70 m.

Figure 5-2 shows the main structure (entire 3D model). The central horizontal slit on the boundary surface is the KWO and GTS tunnels. Figure 5-3 shows a horizontal section at the test level. Figure 5-4 shows the lower half of the first substructure with the fractured zone and the drift while Figure 5-5 also shows the details of the second substructure with the tunnel and installations. A 3D illustration of the fracture zones and the ZEDEX tunnel is shown in Figure 5-6.

The model consists of about 49 790 elements. The elements are 3-dimensional with 8-nodes. The mesh thus includes the buffer but with a lower element density than in the mesh for task B (see chapter 5.4).

5.3.2 Boundary conditions

The following hydraulic boundary conditions were considered suitable (see Appendix 3) and used for the model:

- Upper horizontal boundary: Constant water pressure of –1350 kPa.
- Lower horizontal boundary: No flow
- Boundary along the “South shear zone”: No flow
- Boundary along the “North shear zone”: No flow
- Boundary along the KWO and GTS tunnels: No flow
- Southwest boundary: No flow
- Inner boundaries of the open tunnels: Constant water pressure of 0 kPa.

No flow boundary implies mirroring of the model in the boundary. Since the shear zones are dominant the mirror effect of those boundaries is probably insignificant. It is also probable that the tunnels are dominating the flow at the test level, which means that the boundary along the KWO and GTS tunnels has a minor effect. However, the southwest boundary is very important for the pressure situation. This boundary was at the first calibration calculations applied too close to the test site and therefore moved away.

The mechanical boundary conditions are fixed displacements for the top and bottom surface and for the vertical surfaces the in-plane displacements are fixed. All other boundaries inside the structure are either free (inside the drift during excavation) or coupled to the neighbouring materials.

The thermal boundaries are constant temperature of 12°C at all outer and inner boundaries.

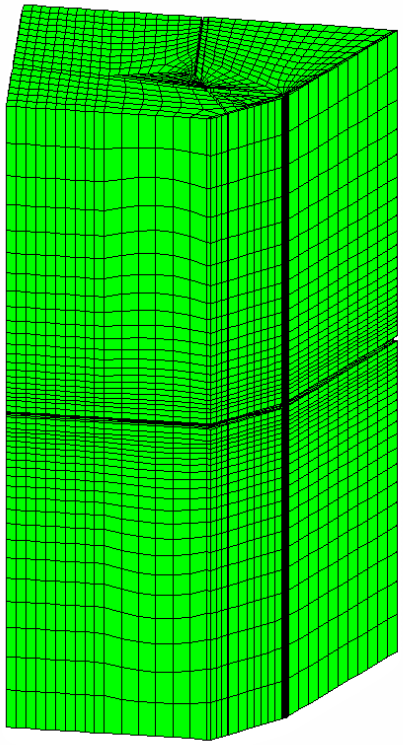

Figure 5-2. *Element mesh. The KWO and GTS tunnels are the black horizontal band in the centre of the model.*

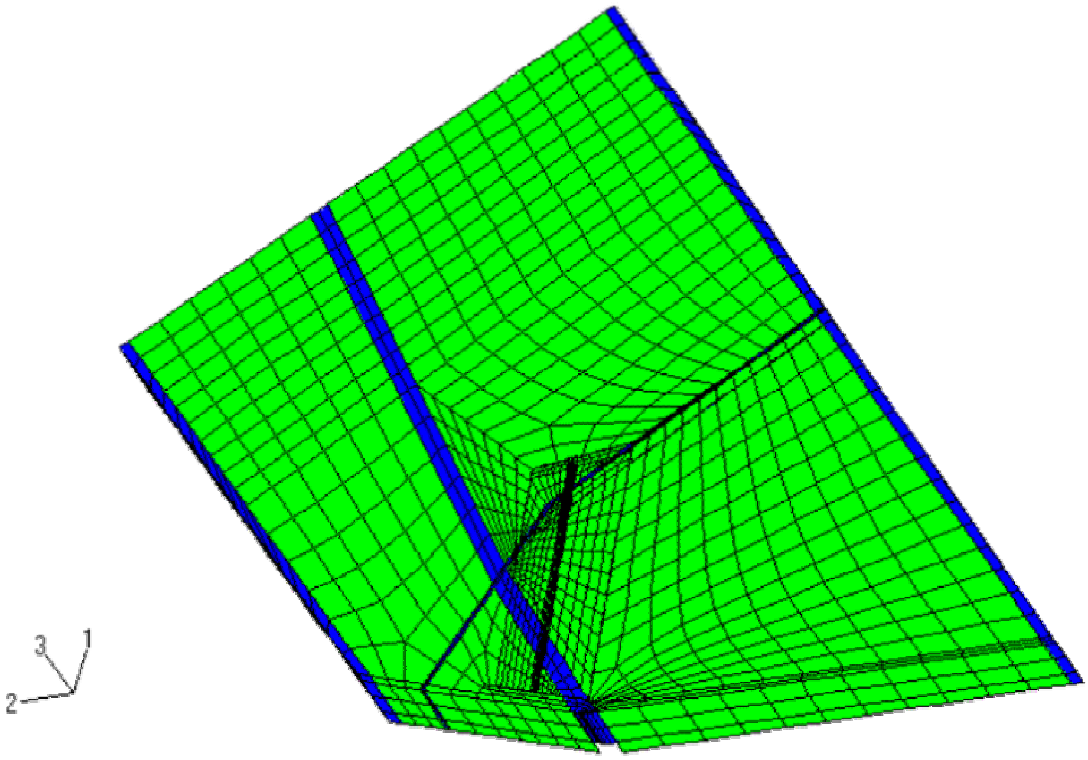

Figure 5-3. *Horizontal section of the entire element mesh at the level of the ZEDEX drift. The fracture zones (in blue) and the FEBEX drift (black) are marked.*

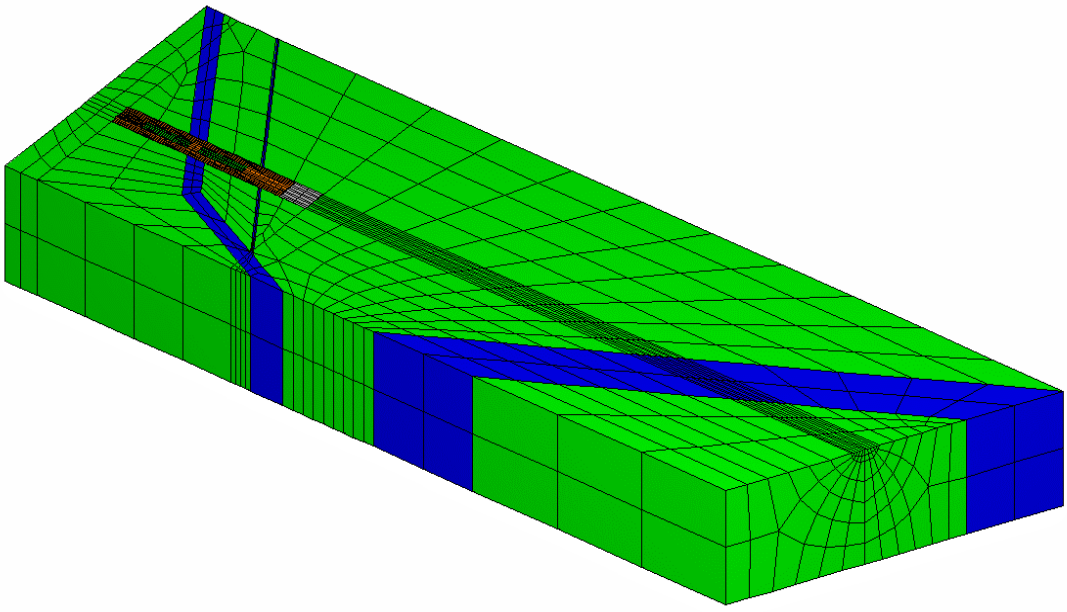

Figure 5-4. *Horizontal section of the first substructure at the level of the ZEDEX drift. The fractures zones (in blue) and the FEBEX drift are marked.*

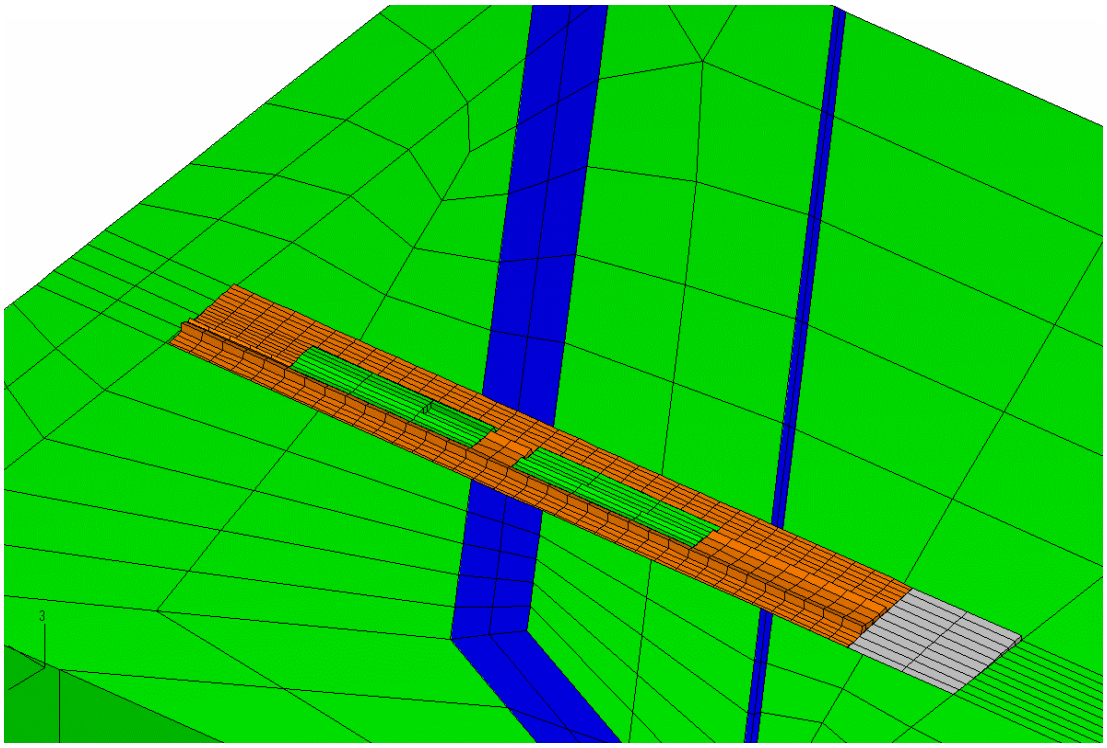

Figure 5-5. *Element mesh of the buffer, plug and canisters and the surrounding rock. The difference in mesh density between the rock and the second substructure with the buffer etc. is obvious.*

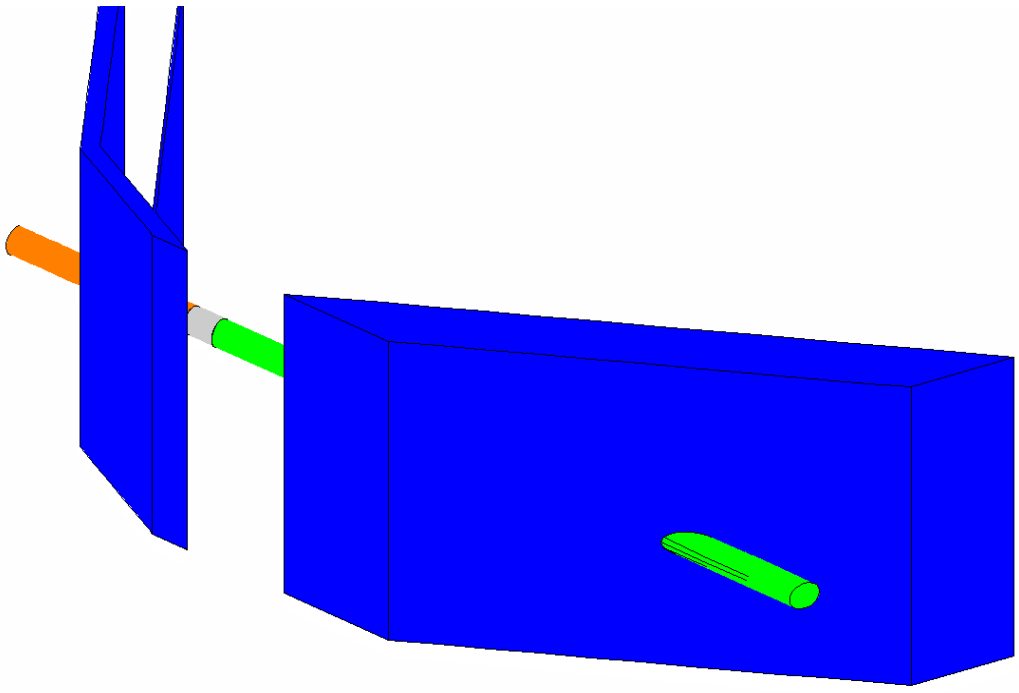

Figure 5-6. *3D illustration of the fracture zones and the ZEDEX tunnel inside the first substructure.*

5.4 Finite element model of mainly the bentonite buffer for task B

5.4.1 General

Since the main issue of task B was to disconnect the influence of the rock from the buffer and study only the processes in the buffer, another mesh with rotational symmetry and a high density of elements could be used. By using a hydraulic boundary condition with the water pressure 0 kPa a very permeable rock with no water pressure was simulated. By comparing the results with measurements and with the results from the large 3D model (see chapter 5.3) the influence of the rock and the element mesh could be studied.

5.4.2 Element mesh

The element mesh is shown in Figures 5-7, 5-8 and 5-9. The mesh is axial symmetric around the centre line of the steel tube. In the hydro-mechanical calculations only the buffer material was simulated while in the thermal analysis the heater and the rock were included in the simulation as well.

5.4.3 Boundary conditions

Mechanical

The boundaries between the buffer and the rock and between the buffer and the plug were mechanically fixed. The boundaries between the buffer and the heaters were free.

Hydraulic

A constant hydrostatic pressure of 0 kPa was applied at the boundaries between the buffer and the rock. The reason for not including the rock in the hydro-mechanical calculation is that Task B only deals with the response of the bentonite. The interaction with the rock was included in Task C. The other boundaries were hydraulically isolated.

Thermal

The outer boundary of the rock and the outer surface of the plug were applied with a heat transfer film coefficient, which is 10 W/m^2, °K for the rock and 5 W/m^2, °K for the plug, and constant temperatures equal the initial temperature.

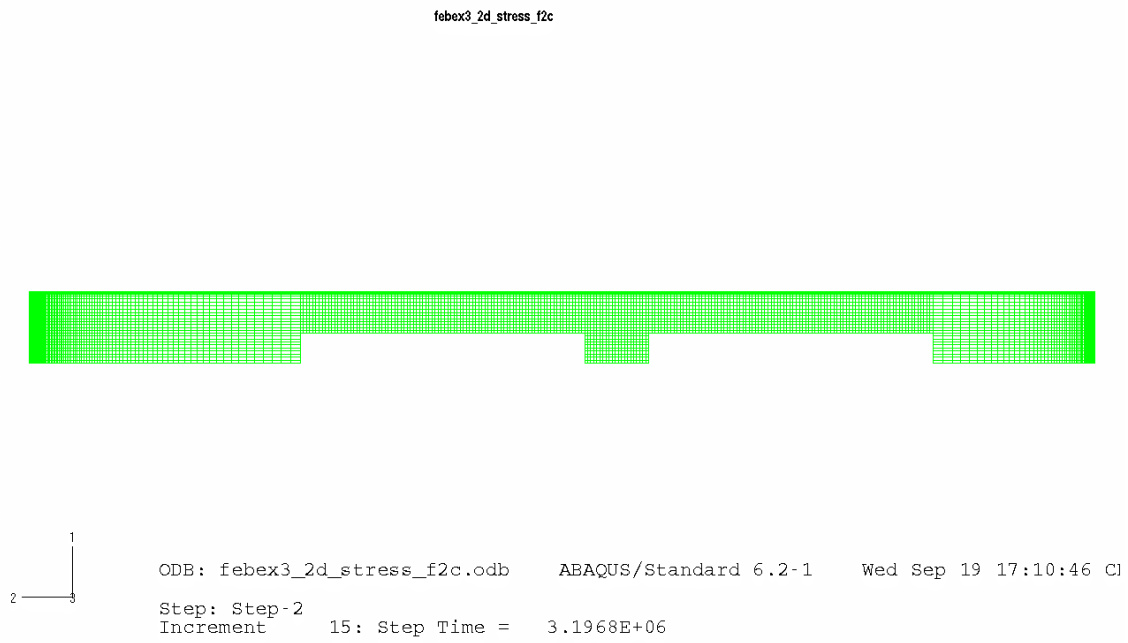

Figure 5-7. *Element mesh of the hydro-mechanical model of the buffer material. The mesh is axially symmetric around the bottom boundary.*

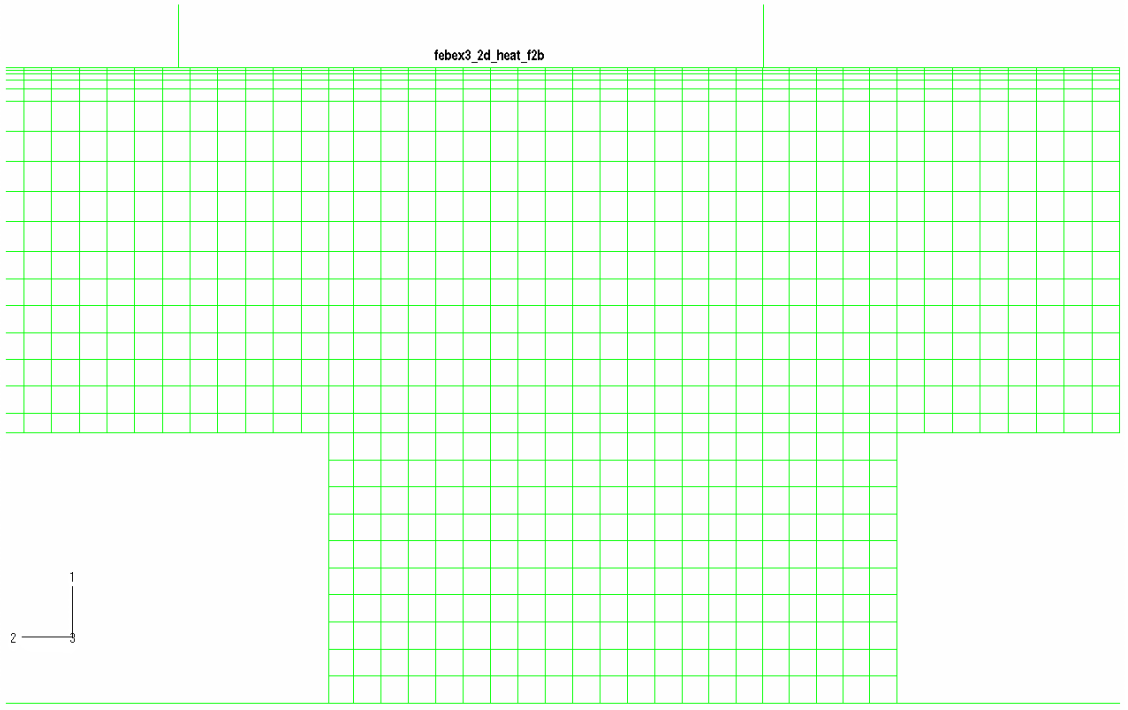

Figure 5-8. *Detail of the mesh of the buffer material between the rock and the heaters.*

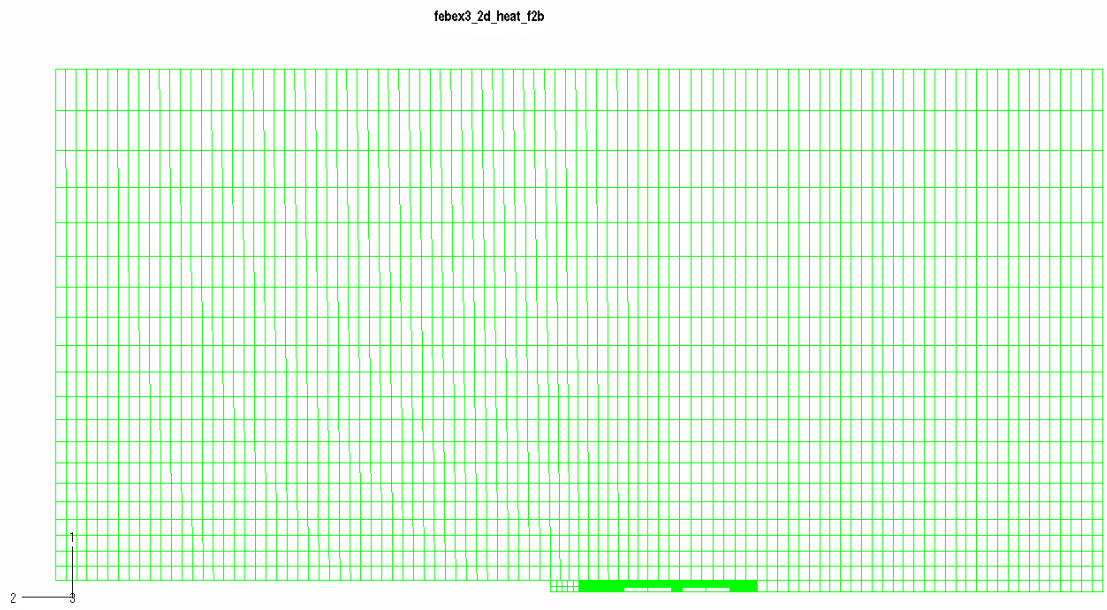

Figure 5-9. *The entire element mesh of the rock for the temperature calculations. The buffer material is the dark detail at the bottom of the model*

6 Material model of the bentonite buffer

6.1 General

This chapter contains a description of the material models for the buffer material and the parameters included in the models

The following processes are modelled:

Thermal:

- Thermal flux from conduction

Hydraulic:

- Water liquid flux
- Water vapour flux
- Hydraulic coupling between the pore water and the pore gas

Mechanical:

- Mechanical behaviour of the structure
- Thermal expansion
- Mechanical behaviour of the separate phases
- Mechanical coupling between the structure and the pore water

The model includes complete coupling between all processes. The processes may be a function of the following variables:

- Temperature
- Degree of water saturation
- Void ratio

6.2 Material models

6.2.1 Thermal flux from conduction

The only thermal flux that is modelled is thermal conduction with the following parameters:

λ = thermal conductivity

c = specific heat

6.2.2 Water liquid flux

The water flux in the liquid phase is modelled to be governed by Darcy's law with the water pressure difference as driving force in the same way as for water saturated clay.

The magnitude of the hydraulic conductivity K_p of partly saturated clay is a function of the void ratio, the degree of saturation and the temperature. K_p is assumed to be a function of the hydraulic conductivity K of saturated clay and the degree of saturation S_r according to Equation 6-1.

$$K_p = (S_r)^{\delta} K \qquad (6\text{-}1)$$

where

K_p = hydraulic conductivity of partly saturated soil (m/s)

K = hydraulic conductivity of completely saturated soil (m/s)

δ = parameter (usually between 3 and 10)

Water transport driven by gravity and density gradients is included in the model as well.

6.2.3 Water vapour flux

The water vapour flux is modelled as a diffusion processes driven by the temperature gradient and the water vapour pressure gradient (at isothermal conditions) according to Equation 6-2:

$$q_v = -D_{Tv}\nabla T - D_{pv}\nabla p_v \qquad (6\text{-}2)$$

where

q_v = vapour flow

D_{Tv} = thermal vapour flow diffusivity

T = temperature

D_{pv} = isothermal vapour flow diffusivity

p_v = vapour pressure

The isothermal vapour flow is neglected and thus D_{pv} =0.

The thermal water vapour diffusivity D_{Tv} can be evaluated from moisture redistribution tests by calibration calculations. The following relations were found to yield acceptable results /6-1/:

$$D_{Tv} = D_{Tvb} \qquad 0.3 \le S_r \le 0.7 \qquad (6\text{-}3)$$

$$D_{Tv} = D_{Tvb} \cdot \cos^{a}\left(\frac{S_r - 0.7}{0.3} \cdot \frac{\pi}{2}\right) \qquad S_r \ge 0.7 \qquad (6\text{-}4)$$

$$D_{Tv} = D_{Tvb} \cdot \sin^b\left(\frac{S_r}{0.3} \cdot \frac{\pi}{2}\right) \quad S_r \leq 0.3 \qquad (6\text{-}5)$$

a and *b* are factors that regulates the decreased vapour flux at high and low degree of saturation.

The diffusivity is thus constant with a basic value D_{Tvb} between 30% and 70% degree of saturation. It decreases strongly to D_{Tv}=0 at 0% and 100% saturation. The influence of temperature and void ratio on the diffusivity is not known and not considered in the model.

6.2.4 Hydraulic coupling between the pore water and the pore gas

The pore pressure u_w of the unsaturated buffer material, which is always negative, is modelled as being a function of the degree of saturation S_r independent of the void ratio.

$$u_w = f(S_r) \qquad (6\text{-}6)$$

ABAQUS also allows for hysteresis effects, which means that two curves may be given (drying and wetting curves)

The pore air pressure is not modelled.

6.2.5 Mechanical behaviour of the structure

The mechanical behaviour has been modelled with a non-linear Porous Elastic Model and Drucker-Prager Plasticity model. The effective stress theory is applied and adapted to unsaturated conditions according to Equation 4-4 by Bishop. The shortcomings of the effective stress theory are compensated for by a correction called moisture swelling (see chapters 6.2.8 and 6.2.9).

The *Porous Elastic Model* implies a logarithmic relation between the void ratio *e* and the average effective stress *p* according to Equation 6-7.

$$\Delta e = \kappa \Delta \ln p \qquad (6\text{-}7)$$

where κ = porous bulk modulus

Poisson's ratio ν is required for the deviatoric part.

Drucker Prager Plasticity model contains the following parameters:

β = friction angle in the *p-q* plane

d = cohesion in the *p-q* plane

ψ = dilation angle

q = $f(\varepsilon^d_{pl})$ = yield function defined for each material

The yield function is the relation between Mises' stress q and the plastic deviatoric strain ε^d_p at a specified stress path. The dilation angle determines the volume change during shear.

6.2.6 Thermal expansion

The volume change caused by the thermal expansion of water and particles can be modelled with the parameters

α_s = coefficient of thermal expansion of solids (assumed to be 0)

α_w = coefficient of thermal expansion of water

Only the expansion of the separate phases is taken into account. The possible change in volume of the structure by thermal expansion (not caused by expansion of the separate phases) is not modelled. However, a thermal expansion in water volume will change the degree of saturation, which in turn will change the volume of the structure.

6.2.7 Mechanical behaviour of the separate phases

The water and the particles are mechanically modelled as separate phases with linear elastic behaviour. The pore air is not mechanically modelled.

6.2.8 Mechanical coupling between the structure and the pore water

Effective stress theory

The effective stress concept according to Bishop is used for modelling the mechanical behaviour of the water-unsaturated buffer material, defining the relation between the effective stress p and total stress p_{tot} according to Equation 6-8:

$$p = (p_{tot} - u_a) + \chi(u_a - u_w) \qquad (6\text{-}8)$$

Equation 6-8 is simplified in the following way:

u_a = 0 (no account is taken to the pressure of enclosed air)

$\chi = S_r$

Moisture swelling

The shortcomings of the effective stress theory can be partly compensated in ABAQUS by a correction called "moisture swelling". This procedure changes the volumetric strain ε_v by adding a strain that can be made a function of the degree of saturation S_r:

$$\Delta\varepsilon_v = f(S_r) = \ln(p_0/p)\cdot\kappa/(1+e_0) \qquad (6\text{-}9)$$

$$p = p_{tot} - u_w \cdot S_r \qquad (6\text{-}10)$$

where

ε_v = volumetric strain

p_0 = initial effective stress taken from the initial conditions

p = actual effective stress

κ = porous bulk modulus (from Equation 6-7)

e_0 = initial void ratio

p_{tot} = actual total stress

u_w = pore water pressure

S_r = degree of water saturation

The moisture swelling relation (*M.S.*) that is needed as input is the logarithmic volumetric strain according to Equation 6-11 where $\Delta\varepsilon_v$ is taken from Equation 6-9.

$$M.S. = \ln(1+\Delta\varepsilon_v) \qquad (6\text{-}11)$$

6.3 Required parameters

The required input parameters for the described THM model (ABAQUS) are the following:

Thermal

- Tables of thermal conductivity $\boldsymbol{\lambda}$ and specific heat $\boldsymbol{c}$ as function of void ratio $\boldsymbol{e}$, degree of saturation $\boldsymbol{S_r}$. and temperature

Hydraulic

- Table of the hydraulic conductivity of water saturated material $\boldsymbol{K}$ as function of void ratio $\boldsymbol{e}$ and temperature $\boldsymbol{T}$.
- Influence of degree of saturation $\boldsymbol{S_r}$ on the hydraulic conductivity $\boldsymbol{K_p}$ expressed as the factor $\boldsymbol{\delta}$ in Equation 5-1.
- The basic water vapour flow diffusivity $\boldsymbol{D_{vTb}}$ and the parameters $\boldsymbol{a}$ and $\boldsymbol{b}$ in Equations 5-3 to 5-5.
- Table of the matric suction $\boldsymbol{u_w}$ as a function of the degree of saturation $\boldsymbol{S_r}$.

Mechanical

- Porous bulk modulus $\boldsymbol{\kappa}$ according to Equation 5-7 and Poisson's ratio $\boldsymbol{\nu}$.
- Drucker Prager plasticity parameters $\boldsymbol{\beta}$, $\boldsymbol{d}$, $\boldsymbol{\psi}$, and the **yield function**.

- Bulk modulus and coefficient of thermal expansion of water ($\boldsymbol{B_w}$, $\boldsymbol{\alpha_w}$)and bulk modulus solids ($\boldsymbol{B_s}$).
- Bishops parameter $\boldsymbol{\chi}$ in Equation 5-8 (usual assumption $\boldsymbol{\chi = S_r}$).
- The volume change correction $\boldsymbol{\varepsilon_v}$ as a function of the degree of saturation $\boldsymbol{S_r}$ (the ”moisture swelling” procedure).

Initial conditions

The following initial conditions of the elements in the structure need to be specified:

- void ratio $\boldsymbol{e}$
- degree of saturation $\boldsymbol{S_r}$
- pore pressure $\boldsymbol{u}$
- average effective stress $\boldsymbol{p}$

6.4 Calibration tests

Most of the required parameters can be determined with direct measurements in the laboratory. However, the following parameters cannot be directly measured:

δ, D_{vTb}, a, b, χ and the ”moisture swelling” procedure.

These parameters need to be calibrated with some indirect tests. It can be done with the following sequence of calibration tests:

Drying and wetting tests

Unconfined samples at the initial void ratio and degree of saturation are dried or wetted by changing the relative humidity in the surrounding air. After equilibrium the density and water ratio of each sample are measured and the relation between the void ratio and the degree of saturation is determined.

The drying and wetting tests are then simulated with the code and the measured and calculated results compared. Since the effective stress theory is not valid the curves will not coincide. The difference is used to determine χ and the ”moisture swelling” data. Usually $\chi = S_r$ is assumed and the difference in volume change directly calculated and used for the ”moisture swelling” procedure.

Swelling pressure tests

The swelling pressure measured at the initial void ratio after completed saturation is used to check that the applied ”moisture swelling” procedure yields the correct swelling pressure by simulating a swelling pressure test. If the calculated swelling pressure disagrees with the measured one, the ”moisture swelling” procedure must be changed. A conflict may appear which has to be solved either by making a compromise and accept some difference or by applying another relation for χ.

Water uptake tests

When the mechanical parameters have been determined the influence of the degree of saturation on the hydraulic conductivity can be checked. The factor δ in Equation 5-1 can be determined with a number of water uptake tests. These tests are made by confining samples with a low degree of saturation in stiff cylinders and apply a filter stone with zero water pressure at one end. The negative water pressure of the unsaturated sample will suck water into the sample. After a certain time, which must be different for all samples, the test is brought to an end. The sample is then sliced into a number of pieces and the water ratio (and if possible also the density) of each piece is determined.

With these tests the degree of saturation (and void ratio) can be plotted as a function of the distance from the water inlet. By simulating the same test with the code the factor δ in Equation 6-1 can be checked.

Temperature gradient tests

Finally, the thermal vapour flow diffusivity can be determined with a number of temperature gradient tests. These tests can be performed in a stiff oedometer with water tight boundaries by applying a constant temperature gradient along the sample. The tests are finished after different times and the sample sliced in the same way as in the previous tests.

With these tests the degree of saturation (and void ratio) can be plotted as a function of the distance to the hot end. By simulating the test with the code D_{vTb}, a, and b in Equations 6-3 to 6-5 can be calibrated.

Calibration sequence

The calibration of the different parameters must be made in the mentioned sequence, since the parameters δ, D_{vTb}, a, and b are not required for simulating the first two tests and D_{vTb}, a, and b are not required for simulating the water uptake test, while all parameters are required for the temperature gradient test.

6.5 Parameter values for the material model

6.5.1 General

The thermal parameters for the material models in ABAQUS have been derived from measurements on FEBEX bentonite. The laboratory tests are described in /1-2/. Additional information for the calibrations were found in /6-2/ (temperature gradient test) and /6-3/ (water uptake tests).

6.5.2 Reference material

The existence of slots between the bentonite blocks makes the average density of the buffer lower than the average density of the blocks.

The basic mean properties of the blocks are the following:

- dry density: ρ_d = 1.69 g/cm^3 and
- water ratio: w = 0.144

which yield (using the density of solids ρ_s = 2.7 g/cm^3 and the density of water ρ_w= 1.00 g/cm^3)

- void ratio: e = 0.60 and
- degree of saturation: S_r = 0.65.

5.53% of the total volume were gaps. About 2.6% of the total volume came from the 30 mm gap in the roof. The rest of the volume is evenly distributed in the buffer. If all gaps are included the average dry density will be ρ_d = 1.60 g/cm^3. If the gap at the roof is excluded the average dry density will be ρ_d = 1.64 g/cm^3. The average value was taken yielding the following initial conditions used for the calculations:

- dry density: ρ_d = 1.62 g/cm^3 and
- water ratio: w = 0.144

which yield

- void ratio: e = 0.67 and
- degree of saturation: S_r = 0.58.

The water ratio at water saturation is for this void ratio w = 0.248.

The latter values of the void ratio and degree of saturation have been used both for deriving parameter values for the material model and as initial conditions in the calculations.

6.5.3 Thermal properties

The thermal conductivity of FEBEX bentonite has been measured and the following expression suggested.

$$\lambda = 1.28 - 0.71/(1+\exp((S_r - 0.65)/0.1)) \quad (6\text{-}12)$$

The values shown in Table 6-1 are taken from this equation and have been used in the calculation with linear interpolation between the values.

Table 6-1. Thermal conductivity of the buffer material as a function of the degree of saturation.

S_r	λ W/m,K
0	0.57
0.1	0.57
0.2	0.58
0.3	0.59
0.4	0.62
0.5	0.70
0.6	0.84
0.7	1.01
0.8	1.15
0.9	1.23
1.0	1.26

The *specific heat* has been calculated as the weight average of the specific heat of water and particles according to Equation 6-13.

$$c=800/(1+w)+4200w/(1+w) \qquad (6\text{-}13)$$

Equation 6-13 yields the input parameters shown in Table 6-2 (linear interpolation)

Table 6-2. Heat capacity *c* of the buffer material as a function of water ratio *w.*

w	C Ws/m,kg
0	800
0.1	1109
0.2	1367
0.3	1585
1.0	2500

6.5.4 Hydraulic properties

Hydraulic conductivity

The hydraulic conductivity of FEBEX bentonite has been measured for a large range of densities /1-2/. Table 6-3 shows the values used in the calculations. The measured values have been divided by 2 as a consequence of the calibration calculations with the water uptake tests (see chapter 6.6). The dependency on temperature has been assumed to be entirely caused by the change in viscosity of water.

The influence of the degree of saturation is governed by the parameter δ in Equation 6-1. For the reference material the standard value

$$\delta = 3$$

has been found to be valid for this bentonite.

Table 6-3. Hydraulic conductivity *K* as a function of void ratio *e* and temperature *T.*

T °C	e	K m/s
20	0.47	$0.048 \cdot 10^{-13}$
20	0.57	$0.11 \cdot 10^{-13}$
20	0.69	$0.25 \cdot 10^{-13}$
20	0.82	$0.55 \cdot 10^{-13}$
50	0.47	$0.07 \cdot 10^{-13}$
50	0.57	$0.17 \cdot 10^{-13}$
50	0.69	$0.37 \cdot 10^{-13}$
50	0.82	$0.83 \cdot 10^{-13}$
70	0.47	$0.10 \cdot 10^{-13}$
70	0.57	$0.22 \cdot 10^{-13}$
70	0.69	$0.49 \cdot 10^{-13}$
70	0.82	$1.1 \cdot 10^{-13}$
90	0.47	$0.12 \cdot 10^{-13}$
90	0.57	$0.28 \cdot 10^{-13}$
90	0.69	$0.6 \cdot 10^{-13}$
90	0.82	$1.4 \cdot 10^{-13}$

Thermal vapour flow diffusivity

The thermal vapour flow diffusivity D_{Tvb} and the parameters a and b according to Equations 6-2 to 6-5 have been determined with calibration calculations (see chapter 6.6)

$\boldsymbol{D}_{Tvb} = 0.4 \cdot 10^{-11}$ m^2/s,K

$a = 6$

$b = 10$

Water retention curve

The water retention properties have been determined both on unconfined and confined samples /1-2/. One relation was measured on confined samples with the dry density between 1.60 and 1.65 g/cm^3 and fitted to the modified van Genuchten expression in Equation 6-3.

$$S_r = S_{r_0} + \left(S_{r_{mas}} - S_{r_0}\right)\left[1 + \left(s/P_0\right)^{1/(1-\lambda)}\right]^{-\lambda}\left[1 - s/P_s\right]^{\lambda_s} \qquad (6\text{-}14)$$

where S_{r0} and S_{rmax} are the residual and maximum degree of saturation and P_0 (MPa), P_s (MPa), λ and λ_s are material parameters with the following values:

$S_{r0} = 0.01$

$S_{rmax} = 1.00$

$P_0 = 3.5 \cdot 10^4$ (kPa)

$P_s = 4.0 \cdot 10^6$ (kPa)

$\lambda = 0.30$

$\lambda_s = 1.5$

Table 6-4 shows chosen data from the relation used in the calculations.

Table 6-4. Relation between pore pressure u_w and degree of saturation S_r (choice of data).

S_r	U_w kPa
0.072	$-2.0 \cdot 10^6$
0.162	$-1.0 \cdot 10^6$
0.195	$-8.0 \cdot 10^5$
0.267	$-5.0 \cdot 10^5$
0.434	$-2.0 \cdot 10^5$
0.582	$-1.0 \cdot 10^5$
0.734	$-5.0 \cdot 10^4$
0.859	$-2.5 \cdot 10^4$
0.92	$-1.5 \cdot 10^4$
0.952	$-1.0 \cdot 10^4$
0.981	$-5.0 \cdot 10^3$
0.99	$-3.0 \cdot 10^3$
0.994	$-2.0 \cdot 10^3$
0.998	$-1.0 \cdot 10^3$
1.0	1.0

Since the water transport is modelled in ABAQUS as governed by the pore water pressure (u_w) but the measurements and requested results are in relative humidity (R_f) a conversion from calculated negative pore water pressure to relative humidity has to be done. The conversion according to Equation 6-15, which is derived from thermodynamic considerations /see e.g. 6-4/, has been used.

$$R_f = \exp(u_w/135\ 022) \qquad (6\text{-}15)$$

6.5.5 Mechanical properties

The following data has been used for the ***Porous Elastic*** model:

$\kappa = 0.165$

$\nu = 0.4$

The value $\kappa = 0.165$ was recalculated from the compression index $C_c = 0.38$ derived from oedometer tests /1-2/.

The following data was derived for the ***Drucker Prager Plasticity*** model (based on results from triaxial tests on similar bentonite clays /6-5/)

$\beta = 17°$

$d = 100$ kPa

$\psi = 2°$

Table 6-5. Yield function.

Q (kPa)	ε_{pl}
113	0
138	0.005
163	0.02
188	0.04
213	0.1

However the Drucker Prager Placticity routine was not activated in the calculation, so no plasticity occurred.

The following standard values have been used for the ***properties of water and solid phases***:

$B_w = 2.1 \cdot 10^6$ kPa (bulk modulus of water)

$B_s = 2.1 \cdot 10^8$ kPa (bulk modulus of solids)

$\alpha_w = 3.0 \cdot 10^{-4}$ (coefficient of thermal volumetric expansion of water)

$\alpha_s = 0$ (coefficient of thermal expansion of solids)

$\rho_w = 1000$ kg/m^3 (density of water)

$\rho_s = 2700$ kg/m^3 (density of solids)

The ***effective stress parameter*** χ in Equation 6-8 is assumed to correspond to the degree of saturation:

$\chi = S_r$

The data for the ***moisture swelling procedure*** is derived from the following assumption:

The relation between total stress and suction of a confined sample (constant volume) is assumed to be linear when suction is decreased to 0. During a decrease in suction from the initial value 99.46 MPa to 0 MPa the total pressure increases from 0 to 7 MPa, which yields the relation given by Equation 6-16.

$p_{tot} = 7000 + 0.07038 \cdot u_w$ (6-16)

where

p_{tot} = total stress (kPa)

u_w = pore water pressure (kPa)

The moisture swelling procedure (*M.S.*) is calculated according to Equations 6-9 to 6-11

$\Delta\varepsilon_v = f(S_r) = \ln(p_0/(p_{tot} - u_w \cdot S_r)) \cdot \kappa/(1+e_0)$ (6-9) and (6-10)

$M.S. = \ln(1+\Delta\varepsilon_v)$ (6-11)

with

p_0 = initial effective stress = $- u_{w0} \cdot S_{r0}$ = 57 687 kPa

κ = porous bulk modulus (from Equation 6-7) = 0.165

e_0 = initial void ratio = 0.67

p_{tot} = total stress = $7000 + 0.07 \cdot u_w$

u_w = pore water pressure = $f(S_r)$ according to the retention curve

S_r = degree of water saturation

The swelling has been checked by simulating the volume change in the suction controlled oedometer tests /1-2/ and compare with measured results (see chapter 6.6).

6.6 Calibration calculations

6.6.1 General

All four types of calibration calculations that were mentioned in chapter 6.4 have been performed. The only difference from the procedure proposed in chapter 6.4 is that the swelling pressure test was used for determining the data for the ***moisture swelling procedure*** as described in chapter 6.5 and the swelling test was used for checking the data, which means that the procedures were done in reverse order.

6.6.2 Swelling pressure test

By locking the nodes of a clay element with e=0.67 and S_r=0.58 and successively increasing the negative pore water pressure from the initial conditions (u=-99460 kPa) the change in total stress with suction and degree of saturation can be calculated. Figure 6-1 shows the results of such a calculation. The swelling pressure at full saturation is 6.9 MPa and the increase is linear with increasing suction from the initial condition, which were the conditions settled for the ***moisture swelling procedure***.

6.6.3 Swelling test

By unlocking the nodes of the clay element with e=0.67 and S_r=0.58 and successively increasing or decreasing the negative pore water pressure from the initial conditions (u=-99 460 kPa) the change in volume or void ratio with suction and degree of saturation can be calculated. In order to compare the results with measurements a constant total stress of 100 kPa was applied on the sample. Figure 6-2 shows the results of the calculation. The sample swells from e=0.67 to e=1.2, which correspond to 32% volumetric swelling. The measured swelling /1-2/ was from e=0.58 to e=1.1 or 33% volumetric swelling.

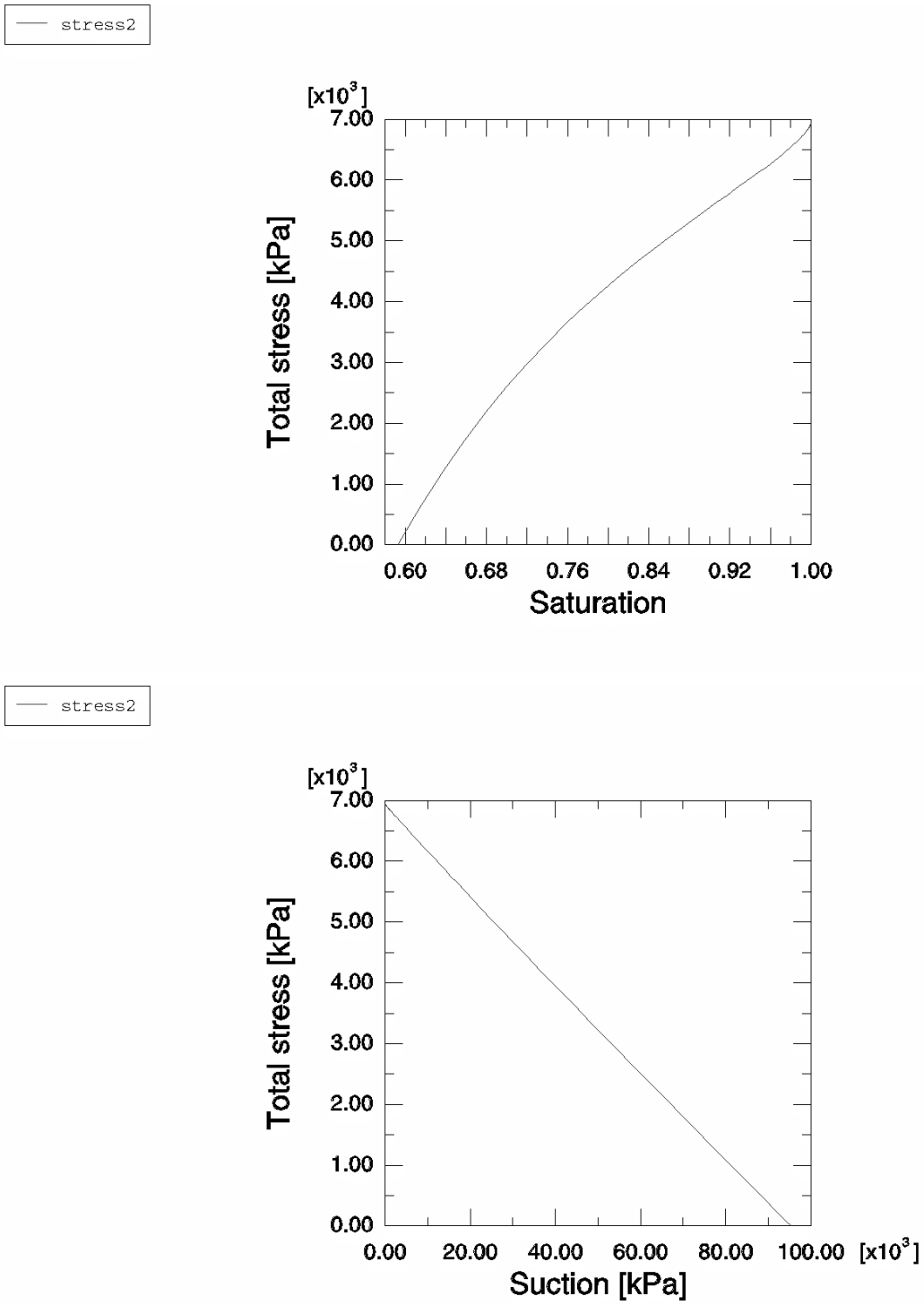

Figure 6-1. *Calculated evolution of total stress of a confined sample at increasing degree of saturation and decreasing suction.*

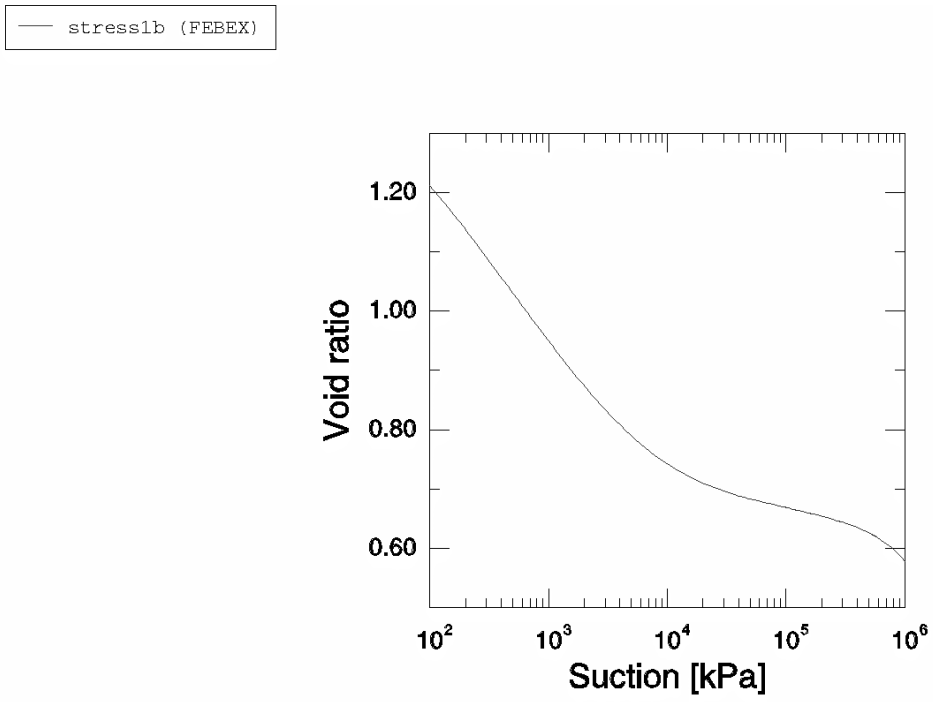

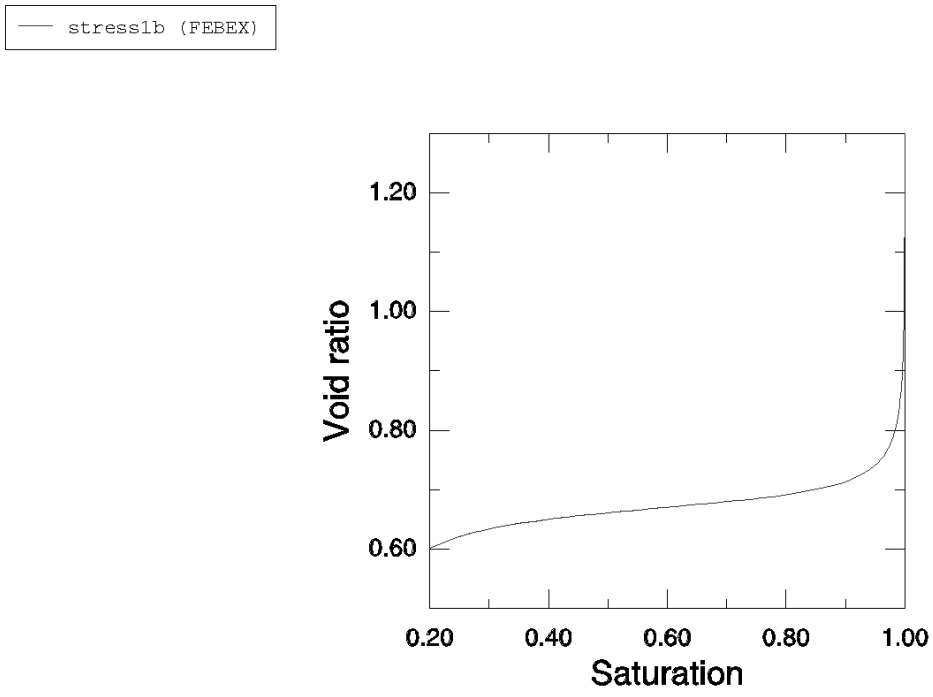

Figure 6-2. *Calculated evolution of void ratio of an unconfined sample as a function of suction and degree of saturation.*

6.6.4 Water uptake tests

Water uptake tests (infiltration tests) have been performed in a steel cell with an internal diameter of 5.0 cm and height of 2.5 cm /6-3/. The sample is hydrated from a filter applied on the top surface of the sample with a water pressure of 1 MPa. Measurement of water inflow into the sample has been made during the tests. The results are shown in Figure 6-3. Complete water saturation was reached after 350 hours, which is clearly shown for test SAT5. SAT5 was left for a long time (59 days) and had similar initial conditions (w=14.4% and ρ_d=1.65 g/cm^3) as the reference material used for the FEBEX calculation.

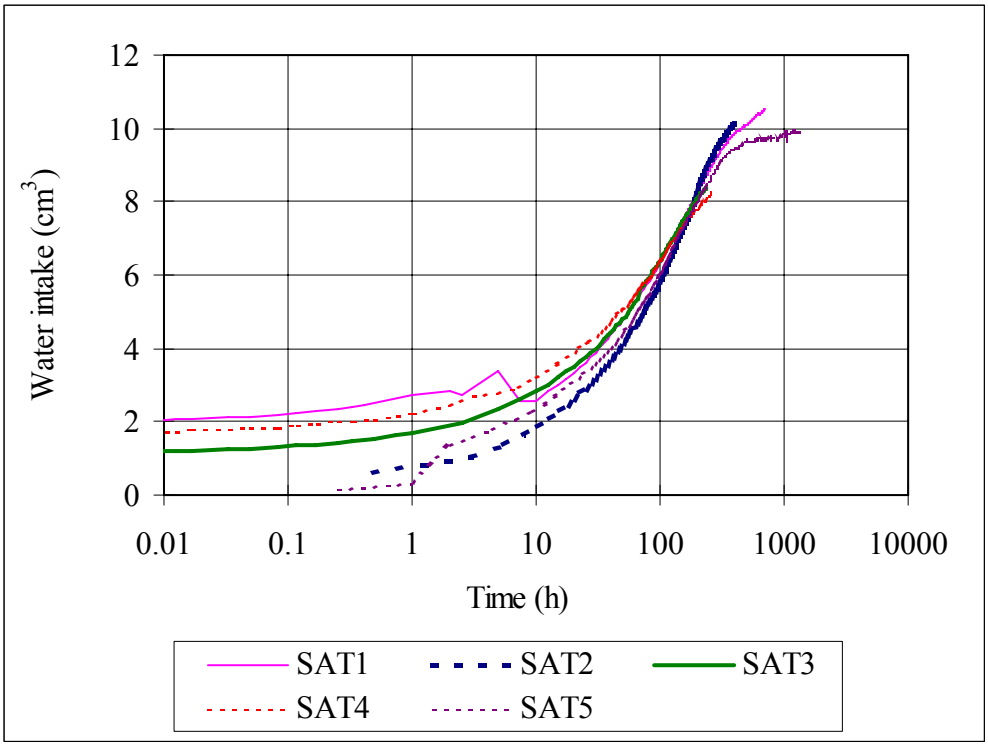

Figure 6-3. *Water intake in the infiltration tests in the steel cell: SAT1 (29 days, ρ_d: 1.65 g/cm^3), SAT2 (15 days, ρ_d: 1.65 g/cm^3), SAT3 (10 days, ρ_d: 1.70 g/cm^3), SAT4 (10 days, ρ_d: 1.70 g/cm^3), SAT5 (59 days, ρ_d: 1.65 g/cm^3) /6-3/.*

This test has been simulated with a 1D mesh with 25 1 mm thick elements with the parameter values shown in chapters 6.4 and 6.5, with exception of the hydraulic conductivity (Table 6-3) that at first was 2 times higher than the final chosen values. However, the calculation with the given hydraulic conductivity yielded a too fast wetting with completed saturation after about 175 hours. The calculation was then repeated with halved values. The results of that calculation are shown in Figure 6-4. The water flux results agree very well (except for the initial stage) and complete saturation reached after 350 hours.

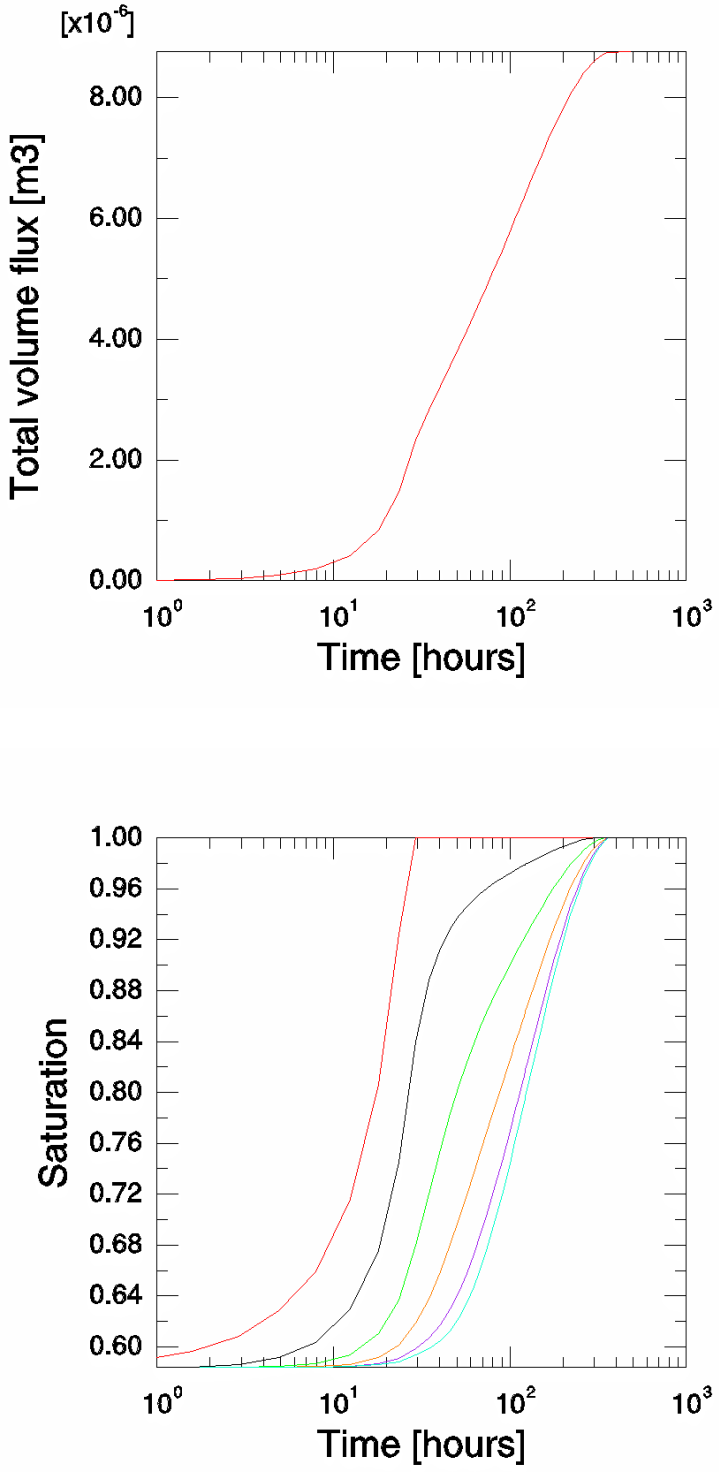

Figure 6-4. *Results of simulation of the water uptake test. The upper diagram shows the water intake and the lower diagram the evolution of the degree of saturation 1, 5, 10, 15, 20 and 25 mm from the filter stone.*

6.6.5 Temperature gradient test

A temperature gradient test has been performed by UPC /6-2/, with a double sample with the length 80 mm and diameter 38 mm placed on each side of a central heater. The specimens were heated to 75 °C by the heater and cooled to have a constant temperature of 30°C at the other ends. The temperature was measured at difference distances from the hot ends. The specimens were confined in radial direction by rubber membranes in order to avoid loss of water during heating.

After 169 hours the test was interrupted and the diameter carefully measured at different parts. The specimens were sliced and the water ratio of each slice determined. Figure 6-5 shows the water ratio and the change in diameter as a function of the distance from the heater for both samples.

The test was simulated with an axial symmetric element mesh consisting of 80 elements. The temperature was applied according to the measurements. The test was then simulated with the material model described in chapter 6.5 and the initial conditions S_r=0.63 and e_0=0.67. Different values of the thermal vapour flow diffusivity D_{Tvb} was used for the calculations and the following value found to yield the best concordance of distribution of water ratio after 169 hours:

$\boldsymbol{D}_{Tvb} = 0.4 \cdot 10^{-11}$ m^2/s,K

The calculations were run to 1000 hours. Figure 6-6 shows the temperature applied and the calculated shape of the specimen after 169 hours. Figure 6-7 shows the distribution of water ratio and void ratio after 169 and 1000 hours, while Figure 6-8 shows a history plot of the change in water ratio for all elements along the centre line. It is obvious that the redistribution of water is not finished after 169 hours ($6.1 \cdot 10^5$ seconds) according to the calculation.

The test can also be used to check the mechanical model. The measured shrinkage at the hot end (10 mm) is a decreased diameter of 0.33 mm while the swelling at the cold end (70 mm) is an increased diameter of 0.6 mm. These values correspond to a volume change of -1.75% and 3.2%. The calculated change in void ratio at the hot end is from e=0.67 to e=0.66 and at the cold end from e=0.67 to e=0.685. These values correspond to a volume change of -0.6% and 0.9%. The model thus seems to under-predict the volume change.

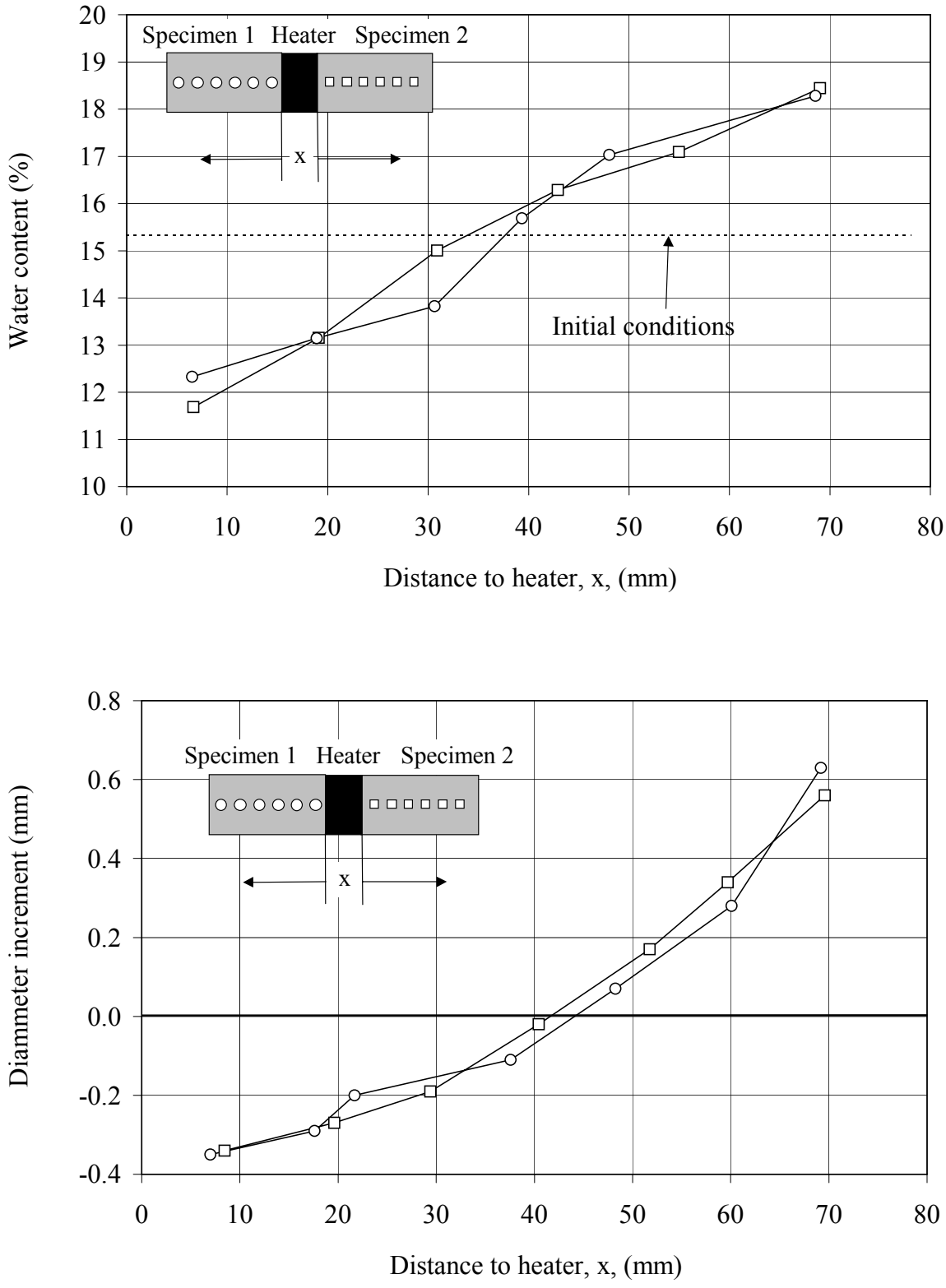

Figure 6-5. *Measured results of the temperature gradient tests /6-2/.*

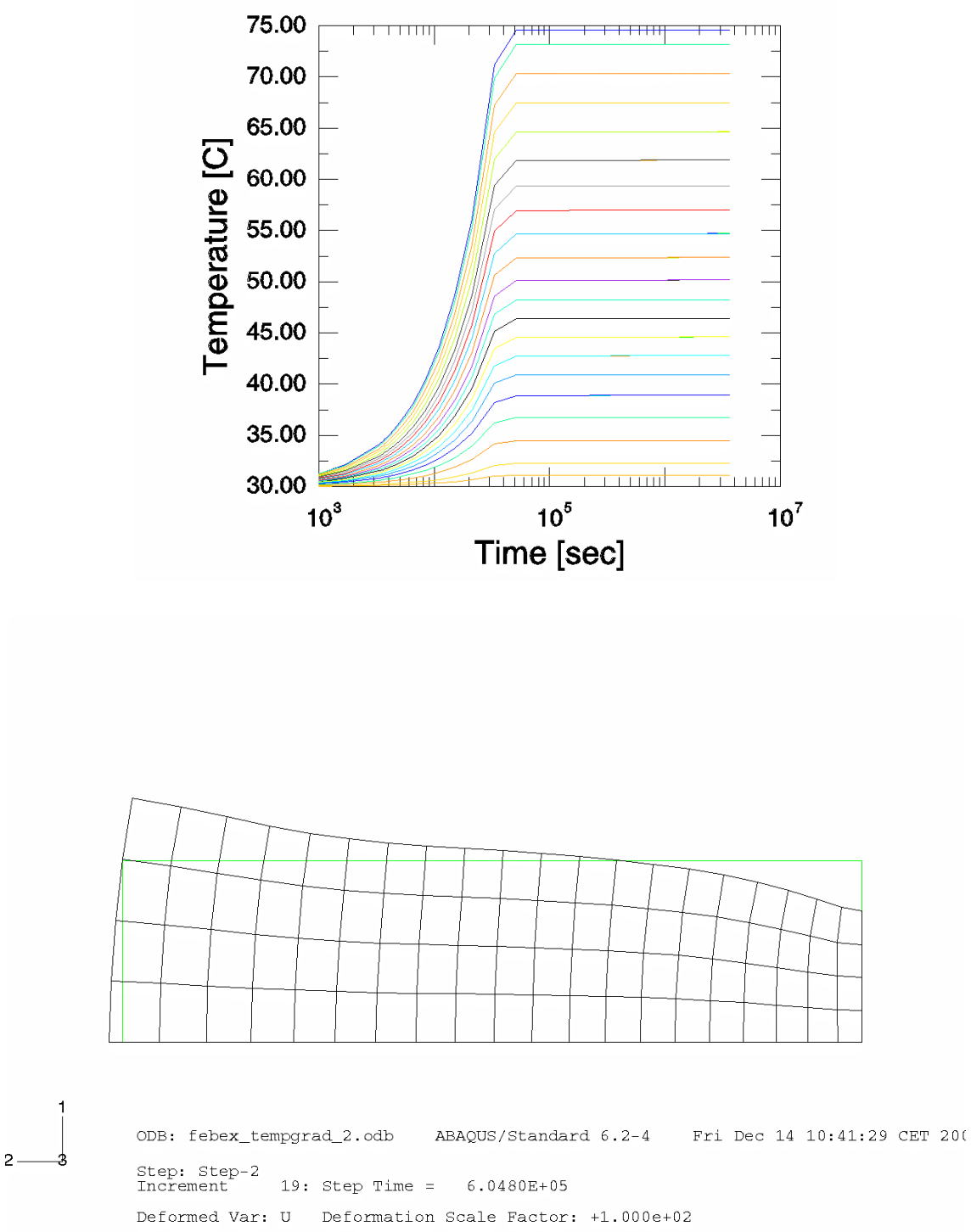

Figure 6-6. *Applied temperature as a function of time for the elements in axial direction (upper figure) and predicted deformation of the sample with a displacement magnification factor of 100.*

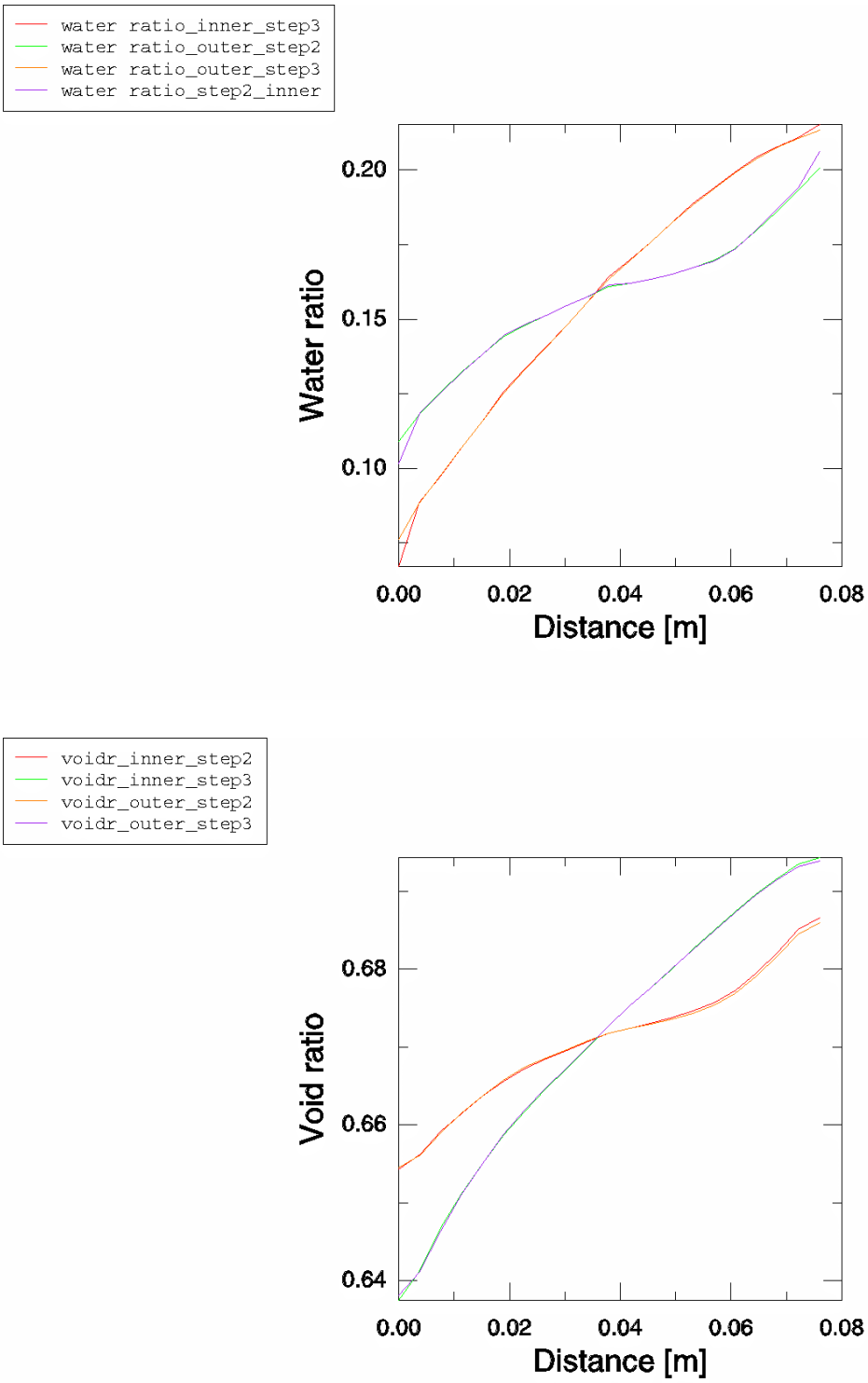

Figure 6-7. *Calculated water ratio and void ratio as a function of the distance from the heater after 169 hours (step 2) and 1000 hours (step 3) for both the inner boundary (centre of sample) and the outer boundary.*

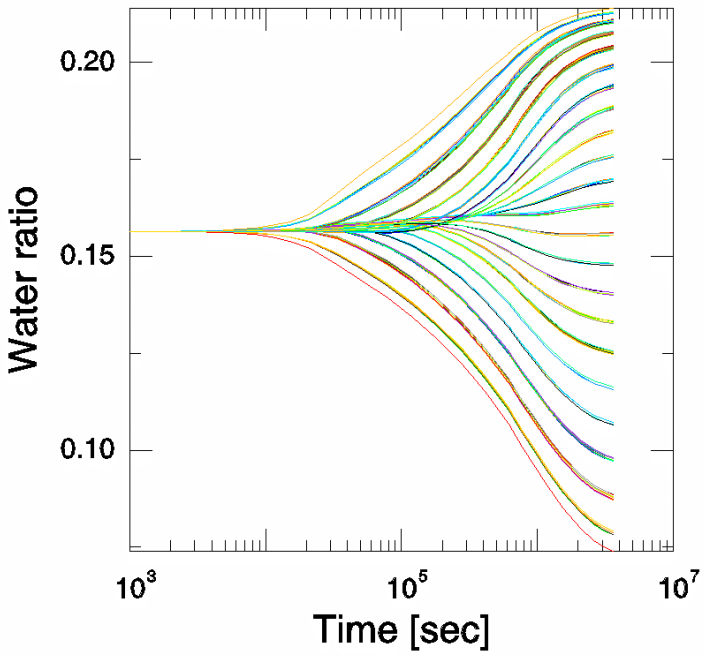

Figure 6-8. *Calculated evolution of water ratio in the specimen for all elements.*

7 Material models of the rock, the fractures and the other materials

7.1 General

The rock is hydraulically modelled as a porous medium with flow governed by Darcy's law and mechanically as linear elastic with thermal expansion. Thermally the rock is modelled with thermal flux governed by Fouriers law. Most properties of the rock were given by the specifications and other reports (see e.g. /7-1/). The rock matrix and fracture hydraulic properties were after the calibration calculations only changed for one fracture zone (see chapter 8.3).

The canister and plug were thermally and mechanically modelled in the same way as the rock. They were not hydraulically modelled (impermeable).

7.2 Rock properties

Hydraulic

The rock matrix is modelled as a porous media with anisotropic hydraulic conductivity with the following values /2-1; Appendix 3/:

$K_1 = 4.6 \cdot 10^{-12}$ m/s

$K_2 = 9.2 \cdot 10^{-12}$ m/s

$K_3 = 6.9 \cdot 10^{-11}$ m/s

Direction 2 is horizontal parallel to the KWO tunnel while direction 3 is vertical (see Figures 5-2 and 5-3)

The model also requires the void ratio e of the rock and the E-modules of water E_w and solids E_s for the transient calculation:

$e = 0.008$ (actually an initial condition)

$E_w = 2.1 \cdot 10^6$ kPa

$E_s = \infty$

Mechanical

The measured E-modulus of the intact rock is around 50 GPa on small samples /1-1/, which don't include the effect of fractures. As an average for the entire rock an E-modulus E_r corresponding to half that value was chosen for this study (matrix as well as fractures).

$E_r = 2.5 \cdot 10^7$ kPa

Poisson's ratio

$\nu = 0.25$

and the following coefficient of thermal expansion were used

$\alpha = 8.3 \cdot 10^{-6}$

Thermal

The following values were used for thermal conductivity λ, density ρ and specific heat c:

$\lambda = 3.6$ W/m,˚K

$\rho = 2400$ kg/m^3

$c = 920$ Ws/kg,˚K

7.3 Fracture properties

Hydraulic

The hydraulic properties of the five fracture zones have been evaluated /7-1; Appendix 3/. Table 7-1 shows the values used in the final predictions of part A. The only change from the given values is the transmissivity of the "Shear and breccia zone", which was reduced with a factor 10 due to the mismatch of the inflow from that zone, found at the calibration calculations.

Table 7-1. Values of width and hydraulic conductivity of the five fracture zones used in the predictions.

Fracture	Width (m)	Hydraulic conductivity (m/s)	Transmissivity (m^2/s)
Shear and breccia zone (F1)	5	$1.38 \cdot 10^{-9}$	$6.9 \cdot 10^{-9}$
Lamprophyre dyke (F2)	1.5	$2.3 \cdot 10^{-10}$	$3.45 \cdot 10^{-10}$
Lamprophyre dyke (F3)	0.25	$2.3 \cdot 10^{-10}$	$5.75 \cdot 10^{-9}$
South shear zone (F4)	5	$2.2 \cdot 10^{-9}$	$1.1 \cdot 10^{-8}$
North shear zone (F5)	5	$2.2 \cdot 10^{-9}$	$1.1 \cdot 10^{-8}$

The other parameters were identical to those of the rock matrix.

Mechanical and thermal

The mechanical and thermal properties are identical to those of the rock matrix except the thermal conductivity /1-1/:

λ = 2.7 W/m,˚K

7.4 Concrete plug

The following properties were applied for the concrete plug:

Hydraulic properties: no flow

Mechanical properties:

$E = 2.0 \cdot 10^6$ kPa

$\nu = 0.3$

Thermal properties:

$\rho = 2400$ kg/m^3

c = 900 Ws/kg,˚K

λ = 1.7 W/m,˚K

7.5 Canisters

The following properties have been applied for the canisters:

Hydraulic properties: no flow

Mechanical properties:

$E = 2.0 \cdot 10^6$ kPa

$\nu = 0.3$

$\alpha = 1.15 \cdot 10\text{-}5$*Thermal properties:*

$\rho = 7850$ kg/m^3

c = 460 Ws/kg,˚K

λ = 450 W/m,˚K

8 Calculation sequence and initial conditions

8.1 General

The modelling was done in several steps. The calculations for task C with the large 3D model of the rock was done with the same time sequence as the real test, starting with the excavation of the tunnel and ending 1000 days after start heating. The calculations for tasks A and C are described in this chapter and the results are shown in chapters 10 and 11. However, the calculations for task B with merely only the buffer included will be described at first.

The boundary conditions were described in chapters 5.3.2 and 5.4.3.

8.2 Buffer calculation for task B

8.2.1 Calculation sequence and numerical solution

The calculations of the THM-processes in the buffer with the axial symmetric model shown in Figures 5-7 to 5-9 have been done with a staggered solution, as described in chapter 4.4 applying the initial value of the degree of saturation for the first temperature calculation. The temperature evolution was thus calculated at first and then the hydro-mechanical response followed by a repeated temperature calculation with calculated degrees of saturation from the hydro-mechanical calculation and so on until the solutions did not change. The power of the heaters was applied according to the following sequence:

Day 0-20: 1200 W per heater

Day 21-53: 2000 W per heater

Day 54-1000: Constant temperature 100 ºC in the entire heater applied during the first 1000 s of day 54 and then kept constant.

For the heat transfer calculation about 9500 4-node elements (axial symmetric dcax4 elements with linear interpolation) have been used.

The system is solved by a direct solver using implicit backward Euler time integration.

For the stress analysis the same amount and type of elements have been used (axial symmetric cax4p 4 node elements that are fully integrated with displacements and pore pressure as nodal variables).

Vapour flux is simulated by using user defined 4-node elements overlaying the mesh.

The system is solved by a direct solver and for the consolidation phase implicit backward Euler time integration is used.

8.2.2 Initial conditions for the calculations

The following initial bentonite conditions were applied (see chapter 6.5):

e = 0.67 (void ratio)

S_r = 0.58 (degree of saturation)

u = -99460 kPa (pore pressure)

p = 57687 kPa (average effective stress)

The following initial temperature was applied in all materials:

T = 12 °C (temperature)

8.3 Rock calculation for task A and coupled rock/buffer calculation for task C

8.3.1 Calculation sequence

The calculations for task C were done in the following sequence:

1. Thermal calculation covering the first 1000 days of the test from start heating. These results were then used in step 5.
2. Application of initial HM-conditions in the rock before excavation
3. Transient HM calculation of the excavation of the FEBEX drift and the subsequent period of 335 days (before the installation of the buffer).
4. 335 days after excavation: Installation of the buffer and application of initial conditions for the buffer.
5. Continuation of the transient HM calculation including the applied temperatures received from the thermal calculation. Calculation run for 1000 days

Before starting the calculations for task C steps 2 and 3 were made for task A and the results used to calibrate the hydraulic model and to predict some hydraulic measurements (see chapter 10).

The planned staggered repetition of the thermal and HM-calculations were omitted since it was concluded that the influence of the buffer wetting on the temperature in the rock (and the subsequent change in HM-response) would be insignificant. If the purpose had been to study the buffer in more detail in this task these steps would have been required.

8.3.2 Initial conditions

The calculations were made in several steps and the excavation of the ZEDEX tunnel was simulated before the actual calculation of the heating and wetting of the buffer.

The hydraulic boundary conditions were applied at the start of the simulated excavation. The excavation was then started with the steady state hydraulic situation of the rock as initial conditions, while the initial conditions of the buffer and the coupling of the bentonite mesh to the rock mesh (simulating the installation) were applied later according to the calculation sequence.

For the mechanical part the following stresses, taken as an average of reported values /1-1/, were applied as principal stresses:

σ_v = 10 MPa (vertical stress)

σ_H = 40 MPa (maximum horizontal stress)

σ_h = 20 MPa (minimum horizontal stress)

The direction of σ_H is perpendicular to the North and South shear zones and the direction of σ_h is thus parallel to those zones.

The thermal initial conditions were a temperature of 12 °C everywhere in the model.

9 Thermo-hydro-mechanical behaviour of the buffer. Results from the calculations of task B

9.1 General

Two main types of calculations were done. One type concerned task B, which was focussed on the processes in the buffer and the other type concerned tasks A and C, which were focussed on the processes in the rock. The rock was in task B only included in the thermal calculation while the buffer was in task C completely included but with a coarser element mesh with the main purpose to look at the influence of the buffer on the rock. This chapter only deals with the results from task B.

The predictions of task B are presented mainly as diagrams of the requested results and comparison with measurements. The location of different sections was shown in Figure 2-3. Some additional results are also shown.

The figures from this chapter are collected as Appendix 1 due to the large number of figures compared to the volume of the text.

9.2 Temperature and heater power

The predicted and measured evolution of the heating power of both heaters as a function of time is shown in Figure 9-1. The diagram shows the power required to keep the heaters at a constant temperature of 100 ºC. The figure shows

1. that some important processes are well captured: an initially high power, which is required due to the heat capacity, and a reduction with time followed at the end of the time period by an increased power required due to that the wetting of the buffer increased the thermal conductivity.
2. that the predicted power for the inner heater is higher than for the outer heater in agreement with the measurements
3. that the predicted powers at all times are between the measured powers
4. that the large measured difference in required power between the two heaters are not predicted

The reason for the mismatch according to item 4 is not clear. One possible explanation is there is a difference in thermal conductivity of the rock around the two canisters, which is not included in the model (in addition to the difference between the lamprophyre and the granite rock).

The predicted and measured distribution of temperature in radial direction in section D1 after 90 and 1000 days are shown in Figure 9-2.

The predicted and measured distribution of temperature in radial direction in section G after 90 and 1000 days is shown in Figure 9-3.

The predicted and measured distribution of temperature in axial direction along line LG1 at the radius 1.14 m after 90 and 1000 days is shown in Figure 9-4.

The predicted and measured distribution of temperature in axial direction along line RC1 at the radius 0.81 m after 90 and 1000 days is shown in Figure 9-5.

The predicted and measured evolution of temperature with time at point D1G (radius 1.14 in section D1) and point GG (radius 1.14 in section G) is shown in Figure 9-6.

A contour plot of the predicted temperature in the entire cross section of the buffer after 1000 days is shown in Figure 9-7.

The predicted and measured temperatures agree rather well with exception of mainly the temperature on the canister surface that is modelled to be 100 ºC. Lower temperature than 100 ºC is measured in some points on the canisters mainly at the corners of the lids.

9.3 Hydraulic results

The predicted and measured distribution of relative humidity in radial direction in section E1 after 90, 180, 300 and 1000 days is shown in Figure 9-8.

The predicted and measured distribution of relative humidity in radial direction in section H after 90, 180, 300 and 1000 days is shown in Figure 9-9.

The predicted and measured distribution of relative humidity in radial direction in section E2 after 90, 180, 300 and 1000 days is shown in Figure 9-10.

The predicted and measured distribution of relative humidity in axial direction at the radius 1.08 m along line LG1 after 90, 180, 300 and 1000 days is shown in Figure 9-11.

The predicted and measured distribution of relative humidity in axial direction at the radius 0.81 m along line RC1 after 90, 180, 300 and 1000 days is shown in Figure 9-12.

The predicted and measured evolution of relative humidity with time is shown in Figures 9-13 and 9-14. Figure 9-13 shows RH at three points with different radius at section H, which is located between the two heaters. Figure 9-14 shows RH at three points with different radius at section E1, which is located in the outer ¼ of heater 1.

It is obvious from the comparisons that the predicted RH at the end of the time period agrees rather well with the measurements but the measured drying in the beginning is faster than the predicted. The reason could either be that the model in general underpredicts vapour flux rates or that the slots between the blocks, which are n ot included in the model, accelerate the vapour flux.

A contour plot of predicted relative humidity in the entire cross section of the buffer after 1000 days is shown in Figure 9-15.

A contour plot of predicted degree of water saturation in the entire cross section of the buffer after 1000 days is shown in Figure 9-16.

A contour plot of predicted pore water pressure in the entire cross section of the buffer after 1000 days is shown in Figure 9-17.

9.4 Mechanical results

The predicted and measured evolution of total radial stress with time at point E2G1 (radius 1.22 in section E2), at point E2H1 (radius 0.48 in section E2), and at point E2G2 (radius 1.19 in section E2) and total axial stress with time at point B2G (radius 0.80 in section B2) is shown in Figure 9-18.

The comparison shows that the agreement between predicted and measured stresses is not good but not too bad either, considering that the evaluation should be made with caution, since it is difficult to measure stresses in stiff materials as bentonite before complete water saturation.

The evolution of total radial stress with time is also shown for all elements in section E2 in Figure 9-19.

A contour plot of the void ratio in the entire cross section of the buffer after 1000 days is shown in Figure 9-20.

10 Hydraulic behaviour before installation of the buffer. Results of the rock calculation for task A

10.1 General

The validation and calibration calculations of the hydraulic behaviour of the rock were initially made with a rock model that was similar to the one shown in Figures 5-2 to 5-6 but without the substructure with the refined mesh of the near field rock. The calculations were made in two steps. At first calibration calculations were done in order to check and calibrate the hydraulic conditions. Then predictions of the inflow into the FEBEX tunnel and the pressure drop due to the tunnel excavation were done.

10.2 Calibration calculations

The modelled pore water pressure distribution before excavation and 100 days after start excavation corresponding to 63 days after finished excavation are shown in Figure 10-1. The water pressure at the inner part of the intended drift is about 800 kPa all the way from the drift to the north and south shear zones before start excavation while the zone influenced by the excavation with decreased water pressure reaches 40-80 m away from the drift.

The inflow to different parts of the site has been measured and is compared to the calculated inflow in Table 10-1, where also the measured water pressure in the near field rock is compared to the calculations.

Table 10-1. Comparison between measured and calculated inflow into the tunnels after calibration (after excavation but before installation of the buffer).

Location of measured inflow	Measured inflow (ml/min.)	Calculated inflow (ml/min.)
Inflow from N shear zone into KWO tunnel	62.5	53.4
Inflow from S shear zone into GTS tunnel	23	50.2
Inflow from “Shear breccia zone” into FEBEX after excavation	33.3	38.9
Total inflow from into GTS and KWO between the shear zones after excavation	27.8	72.9

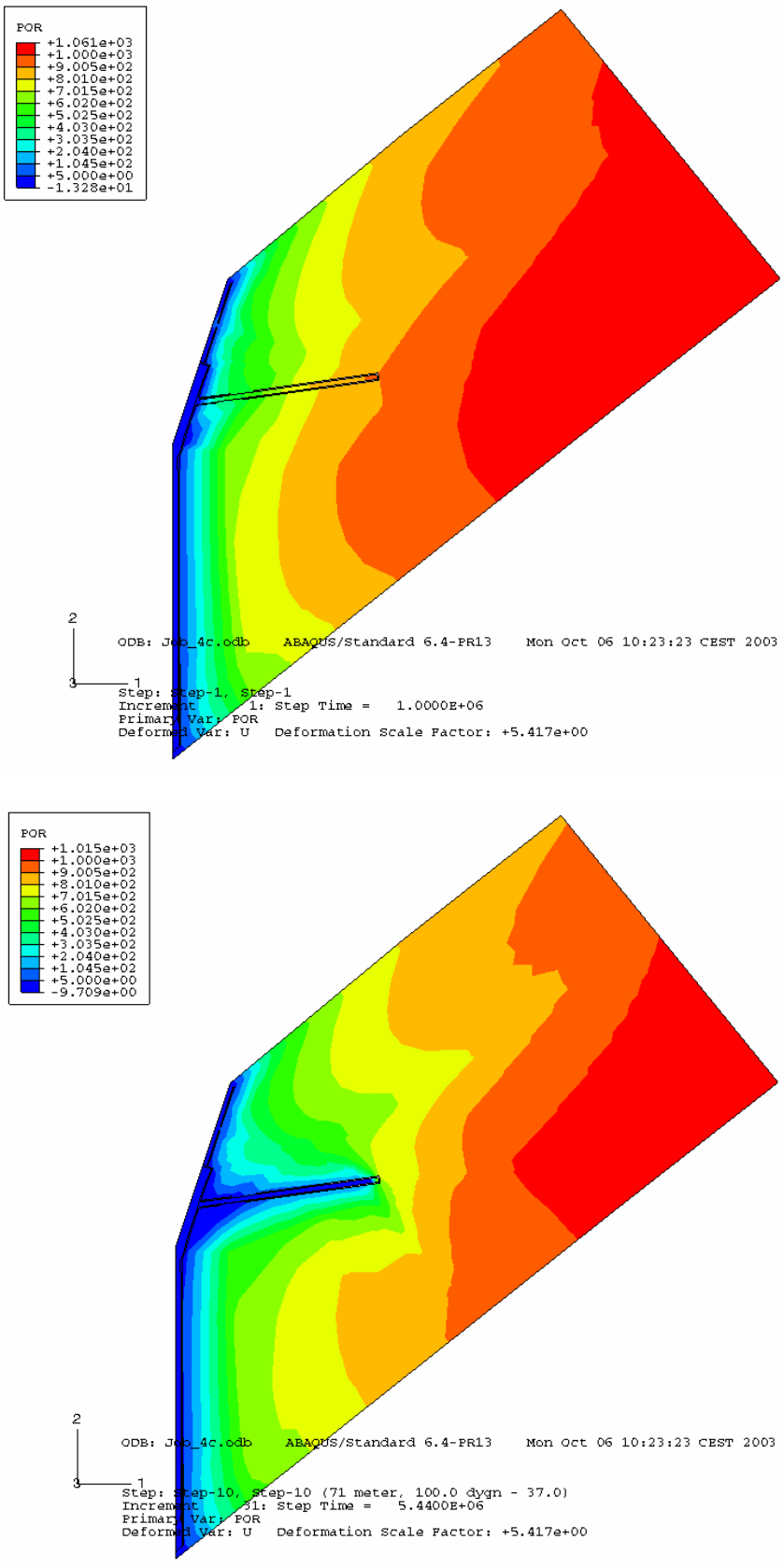

Figure 10-1. *Modelled water pressure distribution (kPa) in a horizontal section of the model before (upper) and after excavation of the FEBEX drift.*

The results validated the model in large and the only calibration or changes done after the first prediction (where all values were taken from the literature) were that the transmissivity of the "Shear breccia zone" was reduced with a factor 10, the water table was lowered 120 m from the top of the model and the south-west boundary was moved 100 m further away from the test site.

In Table 10-2 the measured water pressure in the borehole that runs parallel to the FEBEX drift at a distance of only 3.8 m from the centre of the FEBEX drift is compared to the calculated pressure. The agreement is good between 50 and 100 m from the entrance but rather poor close to the entrance and far away. It is though important that the pressures agree in the location of the FEBEX installation.

Table 10-2. Comparison between measured and calculated water pressure after calibration in borehole FEBEX 95.002 (before excavation).

Measuring section	Measuring interval (meters from entrance)	Measured pressure (kPa)	Calculated average pressure (kPa)
5	23-49	167	620
4	50-61	611	790
3	62-74	759	840
2	75-105	902	880
1	106-132	1568	940

10.3 Predictions

After completed calibration the water pressure drop in sections 3 and 4 during excavation and the total inflow into the test section of the FEBEX drift (54-71 m) were predicted. The water pressure was measured during the mining operation in those sections. The results of the measurements and the predictions are shown in Table 10-3.

Table 10-3. Comparison between measured and calculated water pressure in borehole FEBEX 95.002 during the mine by operation and water inflow into the test section of the FEBEX drift after excavation.

Measuring section	Measuring interval (meters from entrance)	Measured pressure / inflow		Predicted pressure / inflow	
		Before excavation	After excavation	Before excavation	After excavation
4	50-61	680 kPa	480 kPa	790 kPa	300 kPa
3	62-74	790 kPa	670 kPa	840 kPa	300 kPa
FEBEX	54-71	4.5-8.5 ml/min		7.0 ml/min	

The results show that the predicted inflow is well within the range of the measured but also that the predicted water pressure decrease is larger than the measured. This difference is probably caused by a skin zone that seems to appear after excavation. Such a zone is not included in the model.

11 Thermo-hydro-mechanical behaviour after installation of the buffer. Results of the coupled rock/buffer calculation for task C

11.1 General

Two types of results from the calculations with the large 3D-mesh described in chapter 5.3 are shown: At first (in chapter 11.2) some general results not related to the requested results are shown. These results are shown mostly as contour plots of some interesting variables at some interesting times and locations. Then (in chapter 11.3) the requested results are shown. In order to compare how well the predictions agree with the measured results both curves are plotted in the same diagrams.

The figures from this chapter are collected as Appendix 2 due to the large number of figures compared to the volume of the text.

11.2 Some results of general interest

Some results of the temperature calculations are shown in Figures 11-1. The temperature 15 degrees have reached the border of the near field rock (first rock substructure)

Some contour plots of the calculated water pressure results are shown in Figures 11-2 to 11-6. The initial water pressure distribution in the near field rock is shown in Figure 11-2, where one can see that the water pressure is 0 around the empty tunnel and increases to between 350 and 450 kPa at the fringe of the near field rock 6-10 m away from the tunnel.

The water pressure distribution in the near field rock at different times after installation of the buffer is shown in Figures 11-3 and 11-4. It is interesting to note that after 100 days there is a negative water pressure at the rock/buffer contact on the rock surface, which derives from the suction of the buffer, while after 300 days the negative water pressure has changed to positive in large parts of the rock surface at the buffer/rock contact due to the inflow of water that cannot be absorbed by the buffer. After 600 days no negative water pressure is left and after 1000 days the minimum water pressure at the rock buffer contact is +250 kPa.

Figure 11-5 shows the water pressure distribution in the entire rock mass after 1000 days.

The wetting of the buffer is included in the calculation, since all models are completely coupled and the hydraulic interaction between the buffer and the rock is important for the evolution of the water pressure in the rock. Figure 11-6 shows a contour plot of the calculated degree of water saturation at the end of the period (after 1000 days). The figure shows both the result of the coupled calculation with the large rock model in task 1C and the previous result from the detailed calculation of only the buffer from task 1B. Although the pictures do not have a very high resolution it is obvious that the results are rather alike with the contour line of 80% degree of saturation located half way between the rock and the canister. The processes in the buffer has not been the major aim of this task 1C but the comparison anyway shows that they can be captured in spite of the very large scale model of the rock.

11.3 Predicted behaviour of the rock and comparison with measurements

11.3.1 General

Results were requested for some points in the rock where measurements are made (see chapter 3.4). The predicted results are shown in this chapter together with measured results provided by UPC

11.3.2 Evolution of temperature

The calculated evolution of temperature with time in boreholes SF21 and SF22 in points 1-4 within the period (Day 0 – Day 1000) is shown in Figure 11-7 together with measured temperatures (see chapter 3.4.2). The agreement between measured and calculated values is very good.

11.3.3 Evolution of water pressure

The evolution of water pressure with time in boreholes SF21, SF22, SF23 and SF24 in different points within the period (Day 0 – Day 1000) is shown in Figures 11-8 and 11-9. The calculated values are generally 300-500 kPa lower than the measured ones. The reason is mainly caused by a similar difference in start values.

11.3.4 Evolution of normal stresses (σr, σ_θ, σx)

The evolution of the changes of the three normal components of stress within the period (Day 0 – Day 1000) in boreholes SG1 and SG2 is shown in Figure 11-10 together with measured stresses (see chapter 3.4.4). The range of stress change agrees well but there is little correlation for separate measuring points except for point SG1-4 where the measured and calculated results agree very well. These types of stress measurements are however difficult to perform and the measured results may be questioned.

11.3.5 Evolution of radial displacements (ur)

The evolution of radial displacements within the period (Day 0 – Day 1000) in boreholes SI1 and SI2 is shown in Figure 11-11 together with measured displacements (see chapter 3.4.5). The calculated displacements are generally a factor 2 larger than the measured ones in borehole SI1 except for SI1-1, where the agreement is very good. The measured results in SI2 are very low and may be questioned.

11.3.6 Distribution of water pressure (pw) along different radii

The distribution of water pressure along boreholes SF21, SF22, SF23 and SF24 is shown in Figures 11-12 and 11-13 together with measured results. The difference is rather general and mainly caused by a difference in the start pressure, while the measured change in pressure is better captured by the predictions.

12 Comments and conclusions

The wetting of the bentonite based buffer material and the hydraulic response of the surrounding rock in a repository for spent nuclear fuel is depending on not only the properties of the rock and the buffer material but also on the interaction between the rock and the buffer. The large field tests in ÄHRL in Sweden (Prototype Repository) and Grimsel in Switzerland (FEBEX) are very well suited for analysing these interactions since a large number of measurements both in the rock and in the buffer are done and considerable modelling is performed before and during the test operation.

The excavation of the test tunnel and the first 1000 days of the FEBEX experiment have been modelled. The modelling has been performed in three stages where different predictive results have been requested and organized as task A, B and C. Task A concerns hydro-mechanical modelling of the rock with prediction of the effect of excavation of the FEBEX tunnel. Task B concerns thermo-hydro-mechanical prediction of the buffer material during the first 1000 days after installation. Task C concerns thermo-hydro-mechanical prediction of mainly the rock response to the installation and heating during the first 1000 days.

The modelling of the **rock behaviour** for tasks A and C included all steps in the FEBEX experiment, i.e. the excavation, buffer and canister placement, heating of the canisters and the subsequent wetting and swelling of the buffer material, temperature increase and mechanical and hydraulic response in the rock. The calculations of the interaction between the near field rock and the buffer material in the FEBEX tunnel were done by sub-structuring of a very large model of the rock. Although the model has a dimension of 600 m the buffer and near field rock processes could be captured, thanks to the ability of the code ABAQUS to connect structures with different element mesh and element density. A large amount of instruments made it possible to compare the calculations with measurements. The comparison showed that

- the modelled water pressure in the rock in the FEBEX area before excavation of the FEBEX tunnel and the water inflow into the tunnels agree well with measurements after changing the properties of one fractured zone and reducing the level of the ground water table
- the predicted change in water pressure in the near field rock due to the *excavation* of the FEBEX tunnel is larger than the measured change while the predicted and measured inflow into the FEBEX tunnel agreed well
- the predicted change in water pressure in the near field rock due to the *installation* of the buffer is in good agreement with the measurements but the pressure level is lower due to that the initial water pressures before installation of the buffer are only about half the measured ones
- the predicted early decrease in water pressure in the rock caused by the suction of the bentonite is not observed by the measurements
- the temperature predictions agree well with the measurements
- the range in predicted displacements and change of total stress in the near field rock is in good agreement with the range of measured displacements and stress but the correlation between predictions and measurements in the specific points are poor.

The temperature predictions were thus as expected good. It is generally known that temperature is rather easy to predict.

Some of the hydraulic predictions after installation of the buffer were not so good although the change in water pressure in the near field rock was well predicted. The main reason for the discrepancy is that the initial water pressure derived after excavation of the FEBEX tunnel was too low. The conclusion is that there is a skin effect with different properties in the rock boundary around the drift that is not included in the model. That such a skin effect exists has been found in other large-scale tests as the Buffer Mass Test in Stripa /12-1/ and the Backfill and Plug Test in Äspö HRL /12-2/.

Another discrepancy is that the predicted reduction in water pressure in the boreholes of between 50 and 300 kPa during the first months was not observed in the measurements. The reason for the latter discrepancy can be e.g.

- a difference in behaviour of the modelled and real contact between the buffer and the rock. The negative pore pressure in the buffer might not be distributed to the rock if the water flow in the rock mainly takes place in fractures instead of in the rock matrix as modelled. This could be related to the skin effect found for the excavation phase.
- a delayed rock/buffer interaction caused by the slot between the rock and the buffer
- measurement problems that may be induced by the large water volume and possible air pockets between the packers in the boreholes

The results of the mechanical predictions are ambiguous. The range in predicted change of total stress in the near field rock is in good agreement with the range of measured stress but the correlation between prediction and measurement in the specific points are poor. There are two possible main reasons for the discrepancies and both are probably part of the explanation:

- The rock model is not accurate enough, since the rock structure is more complicated than the model.
- Measuring stresses and strains in rock is difficult and the results may be unreliable

The modellings of the **buffer behaviour** were mainly done for task B but also included in task C. They showed that the thermo-hydro-mechanical predictions agreed rather well with measurements in both models. The following conclusions can thus be drawn:

- The influence of the rock on the wetting of the buffer is insignificant, which means that the rock provides the buffer with the required water flow but also that the water pressure built up in the rock/buffer interface is not so high that it influences the wetting. The reason is that the hydraulic conductivity is much higher in the rock than in the buffer and that the overall water pressure in the rock is low compared to the suction in the buffer.
- The fair agreement in results between the large integrated model and the specific buffer model showed that the buffer and near field rock processes can be captured in a large model, thanks to the ability of the code ABAQUS to connect structures with different element mesh and element density.

References

1-1 **DECOVALEX III, Task 1: Modelling of FEBEX in-situ test. PART A:** HYDRO-MECHANICAL MODELLING OF THE ROCK (rev. 3).

1-2 **DECOVALEX III, Task 1: Modelling of FEBEX in-situ test. PART B:** THERMO-HYDRO-MECHANICAL ANALYSIS OF THE BENTONITE BEHAVIOUR

1-3 **DECOVALEX III, Task 1: Modelling of FEBEX in-situ test. PART C:** THERMO-HYDRO-MECHANICAL ANAYSIS OF THE ROCK (Rev. 2).

2-1 **ENRESA 1998.** FEBEX. Full scale engineered barriers experiment in crystalline host rock. Pre-operational stage. Summary report. ENRESA publicacion tecnica num. 01/98.

4-1 **ABAQUS Inc.** ABAQUS manuals.

6-1 **Börgesson L. & Johannesson L.-E. 1995.** Thermo-Hydro-Mechanical modelling of water unsaturated buffer materials. Status 1995. SKB Arbetsrapport AR 95-32.

6-2 **Pintado X., Ledesma A, and Lloret A.** Backanalysis of thermohydraulic bentonite properties from laboratory tests. UPC.

6-3 **Villar M.V. 1999.** Ensayos THM para el proyecto FEBEX. CIEMAT report 70-IMA-L-0-66.

6-4 **Fredlund D.G., and Rahardjo H. 1993.** Soil Mechanics for unsaturated soils. John Wiley & Sons Inc., New York.

6-5 **Börgesson L, Johannesson L-E, Sandén T, Hernelind J, 1995.** Modelling of the physical behaviour of water saturated clay barriers. Laboratory tests, material models and finite element application. SKB Technical Report TR 95-20, SKB, Stockholm.

7-1 **Guimerà J, Carrera J, Martínez L, Vázquez E, Fierz T, Buhler C, Vives L, Meier P, Medina A, Saaltink M, Ruiz B and Pardillo J, 1998:** FEBEX Hydrogeological characterization and modelling. UPC, 70-UPC-M-0-1001, Jan. 1998

12-1 **Börgesson L., Pusch R., Fredriksson A., Hökmark H., Karnland O. and Sandén T. 1992.** Final Report of the Rock Sealing Project – Identification of Zones Disturbed by Blasting and Stress Release. SKB Stripa Project TR 92-21.

12-2 **Börgesson L. and Hernelind J. 1999.** Preparatory modelling for the backfill and plug test. Scoping calculations of H-M processes. SKB ÄHRL IPR-99-11.

APPENDIX 1. Figures 9-1 to 9-20

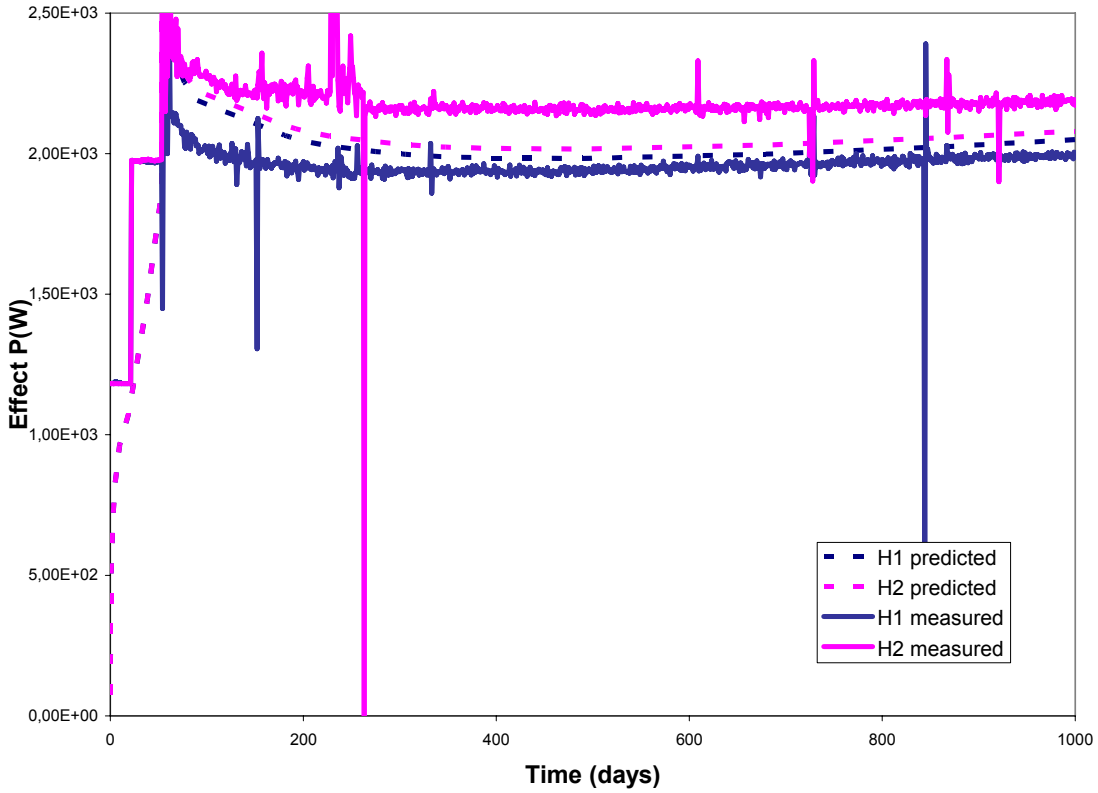

Figure 9-1. *Evolution of predicted and measured heating power as a function of time. Heater 1 corresponds to the outer heater (close to the plug).*

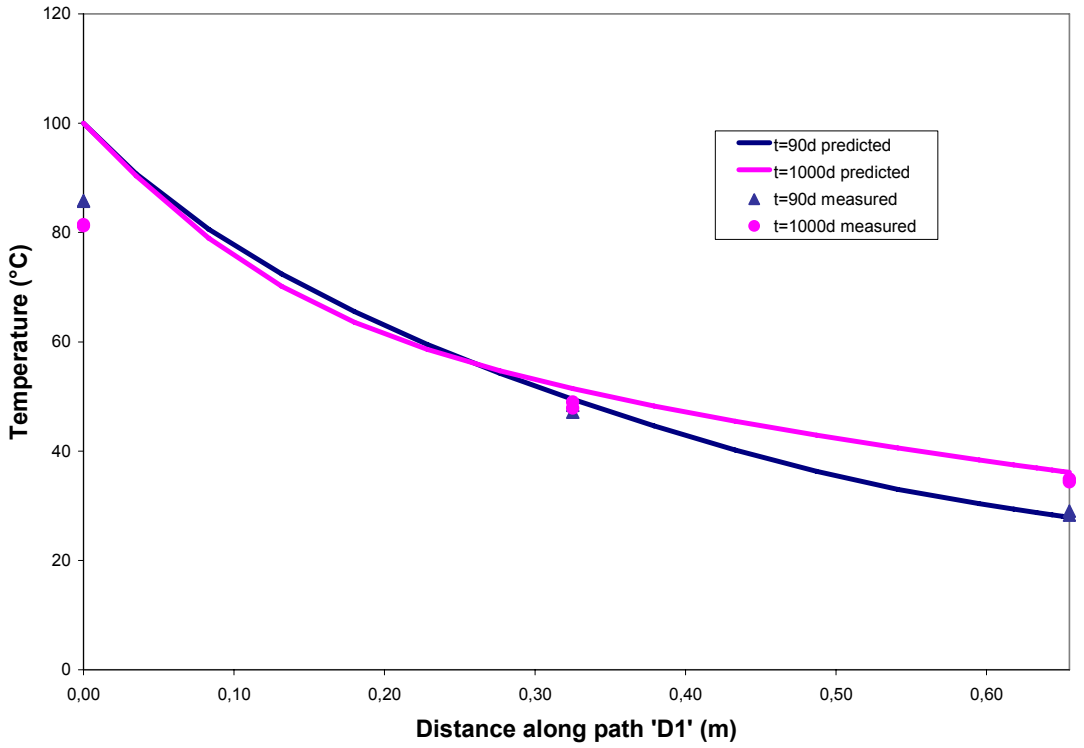

Figure 9-2. *Distribution of predicted and measured temperature (ºC) in radial direction in section D1 after 90 and 1000 days.*

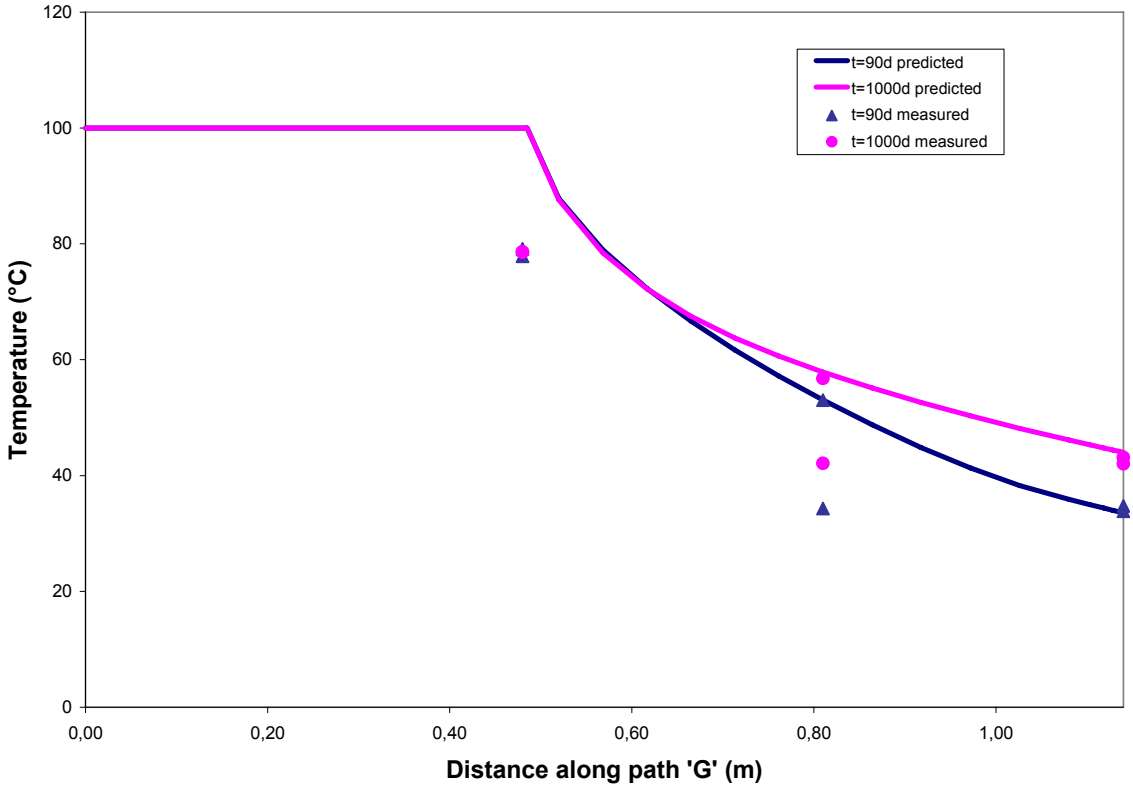

Figure 9-3. *Distribution of predicted and measured temperature (ºC) in radial direction in section G after 90 and 1000 days.*

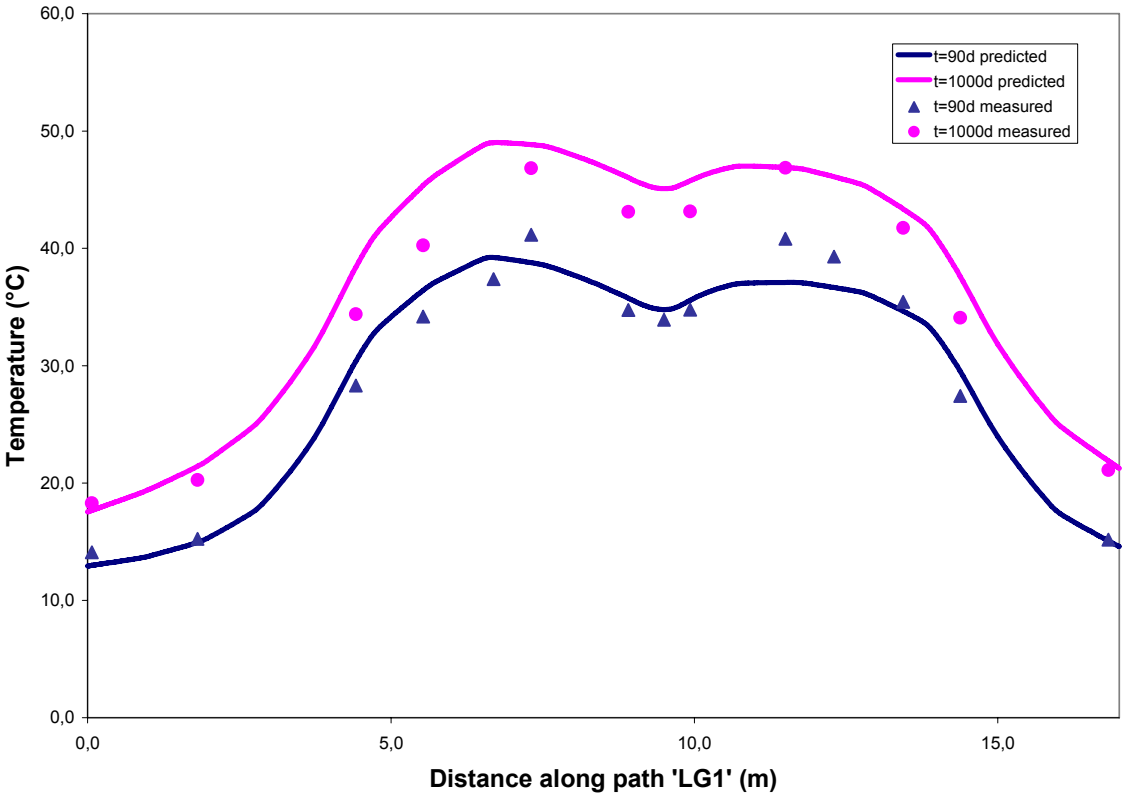

Figure 9-4. *Distribution of predicted and measured temperature (ºC) in axial direction (ºC) along line LG1 at the radius 1.14 m after 90 and 1000 days.*

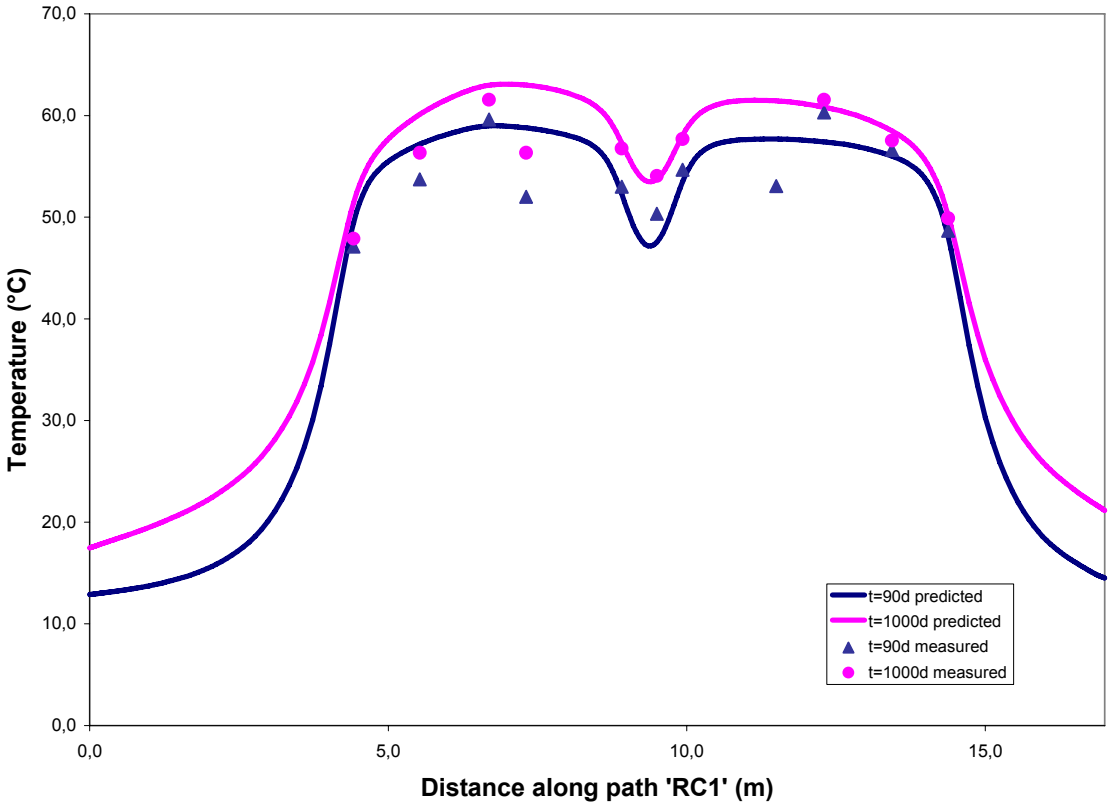

Figure 9-5. *Distribution of predicted and measured temperature (°C) in axial direction along line RC1 at the radius 0.81 m after 90 and 1000 days.*

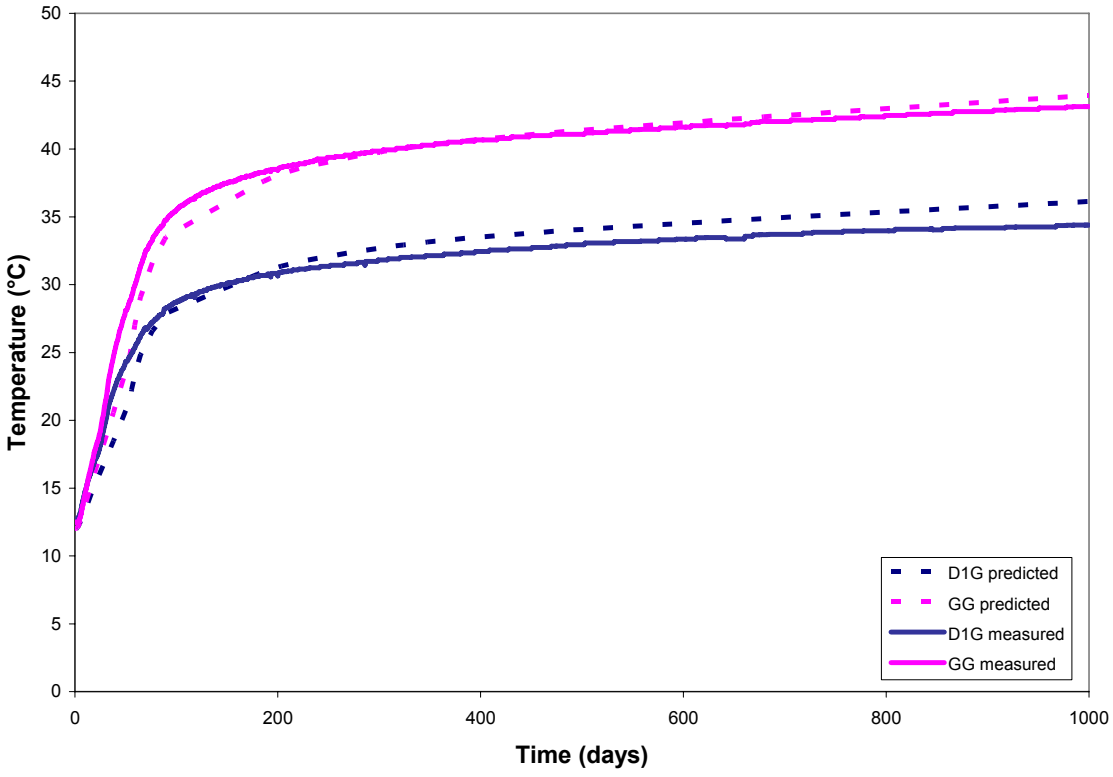

Figure 9-6. *Evolution of predicted and measured temperature (°C) with time (days) at point D1G (radius 1.14 in section D1) and point GG (radius 1.14 in section G).*

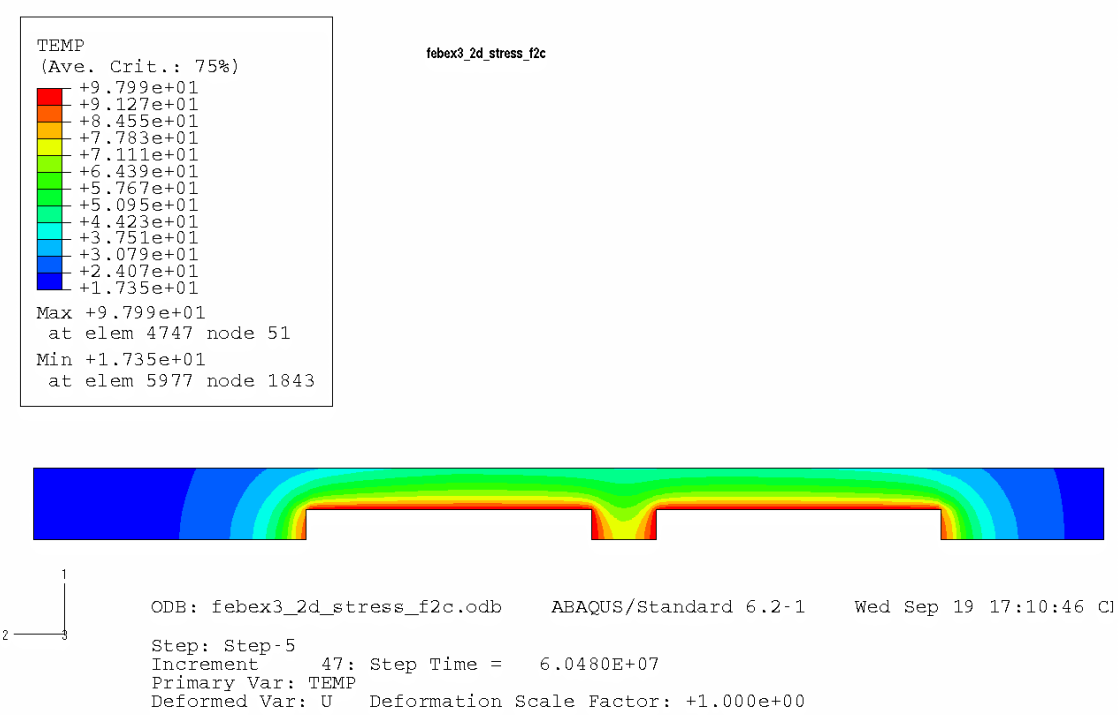

Figure 9-7. *Contour plot of temperature (ºC) in the entire cross section of the buffer after 1000 days.*

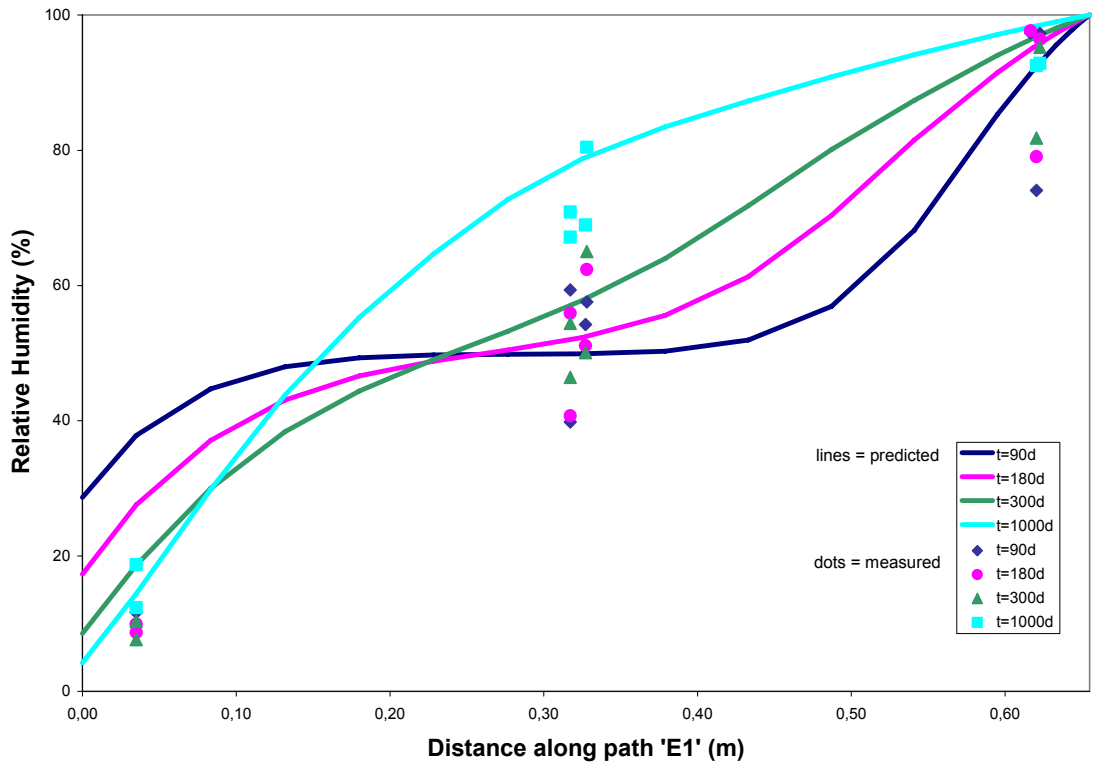

Figure 9-8. *Distribution of predicted and measured relative humidity in radial direction in section E1 after 90, 180, 300 and 1000 days as a function of the distance from the heater surface.*

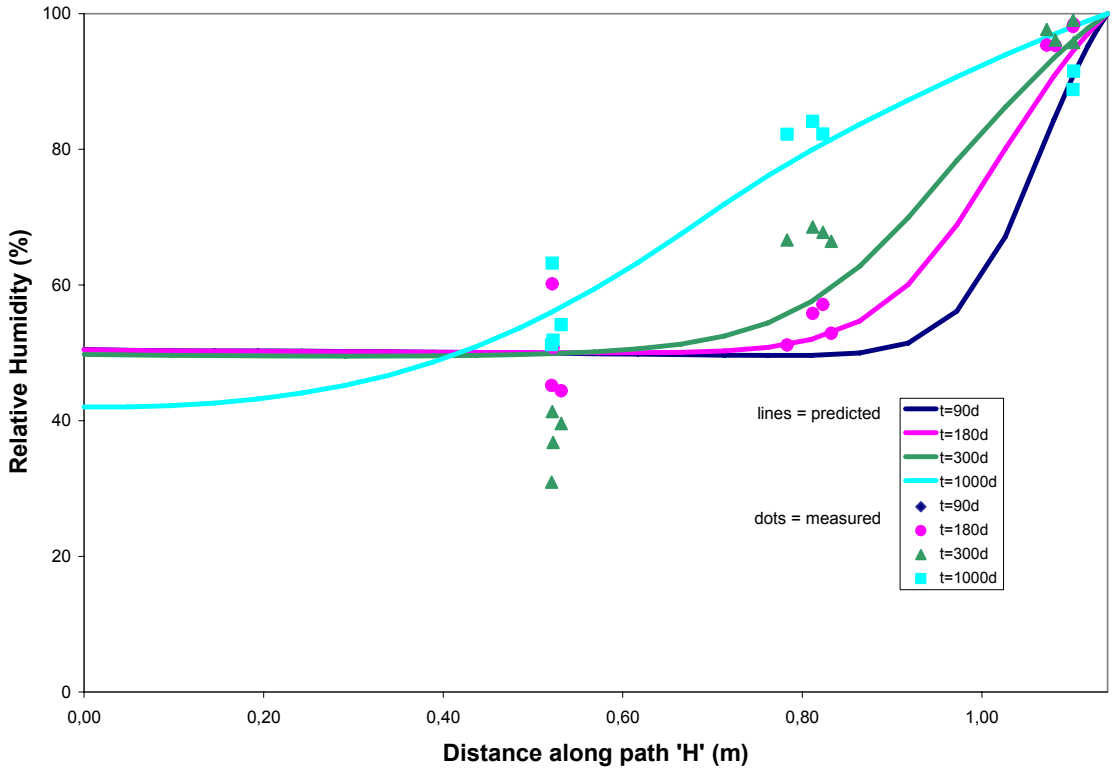

Figure 9-9. *Distribution of predicted and measured relative humidity in radial direction in section H after 90, 180, 300 and 1000 days as a function of the distance from the centre line.*

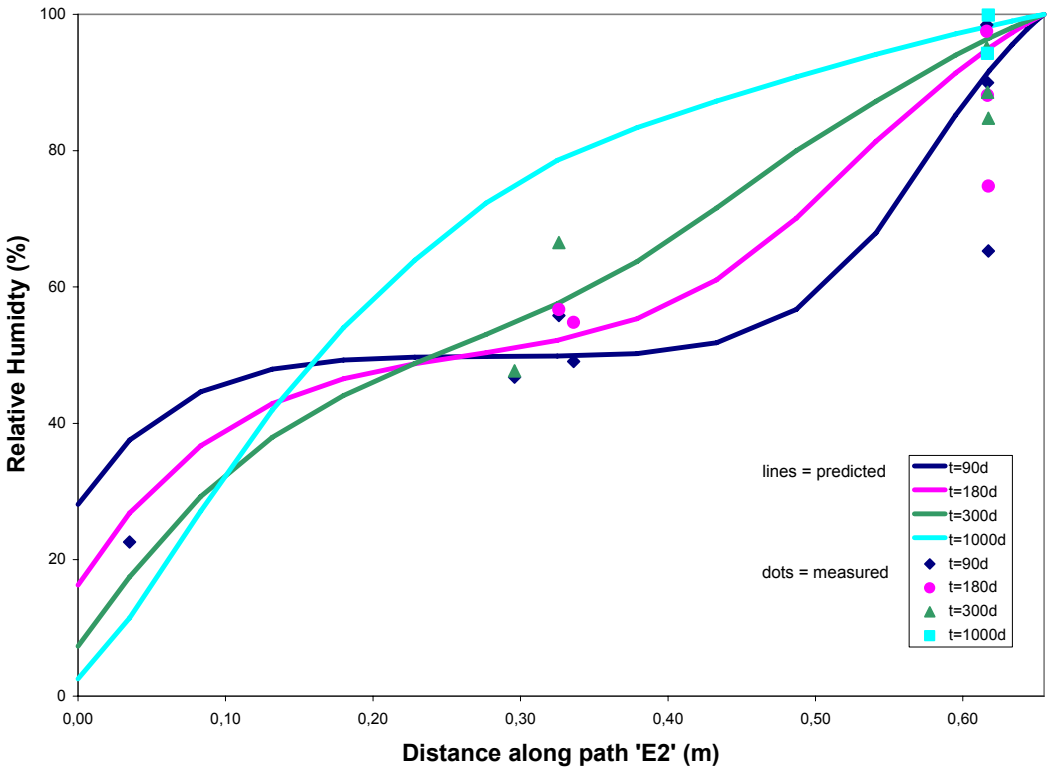

Figure 9-10. *Distribution of predicted and measured relative humidity in radial direction in section E2 after 90, 180, 300 and 1000 days as a function of the distance from the heater surface.*

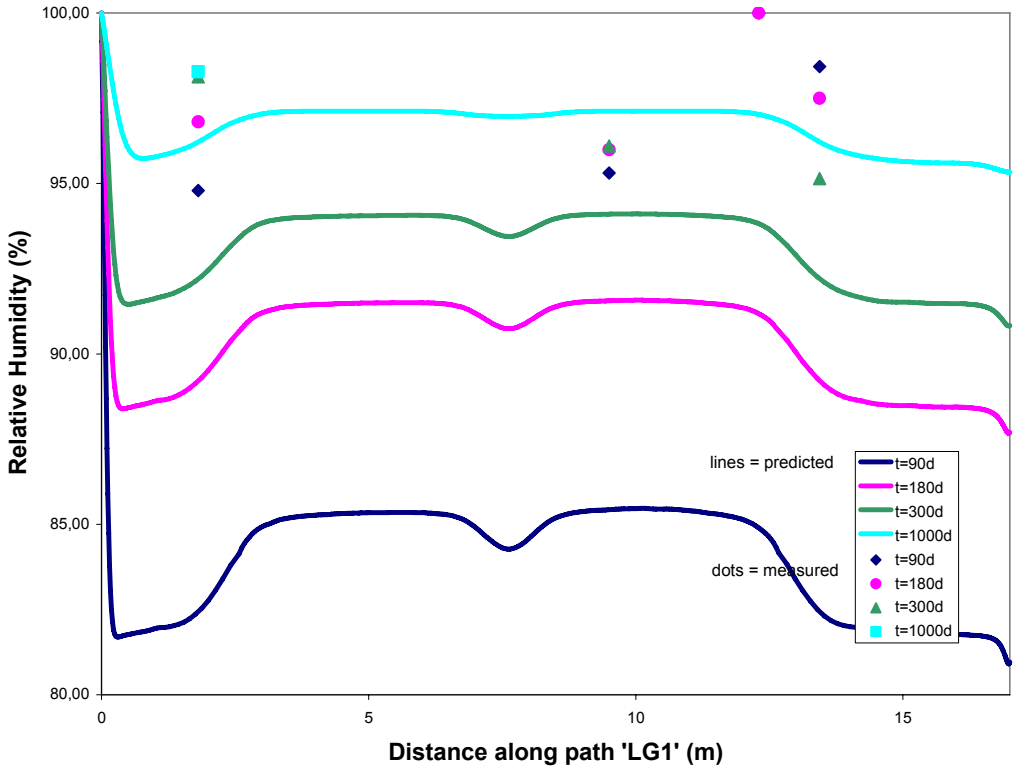

Figure 9-11. *Predicted and measured relative humidity in axial direction at the radius 1.08 m along line LG1 after 90, 180, 300 and 1000 days as a function of the distance from the plug.*

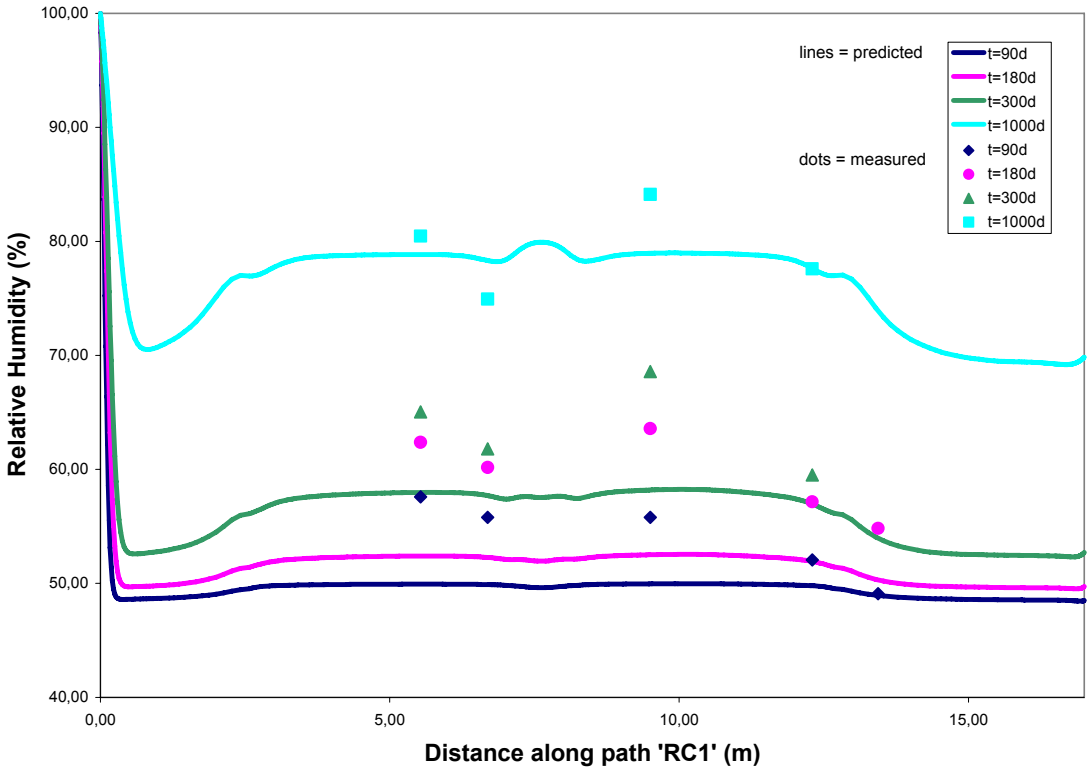

Figure 9-12. *Predicted and measured relative humidity in axial direction at the radius 0.81 m along line RC1 after 90, 180, 300 and 1000 days as a function of the distance from the plug.*

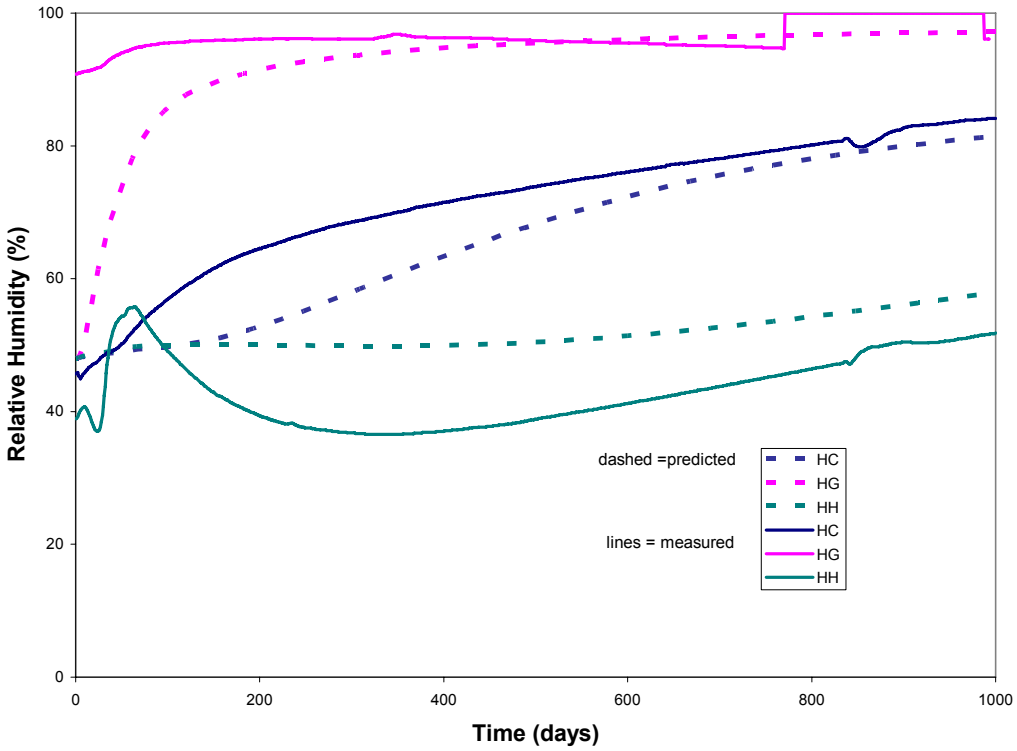

Figure 9-13. *Evolution of predicted and measured relative humidity with time at the following three points in section H: HH (radius 0.52 m), HC (radius 0.81 m) and HG (radius 1.07 m).*

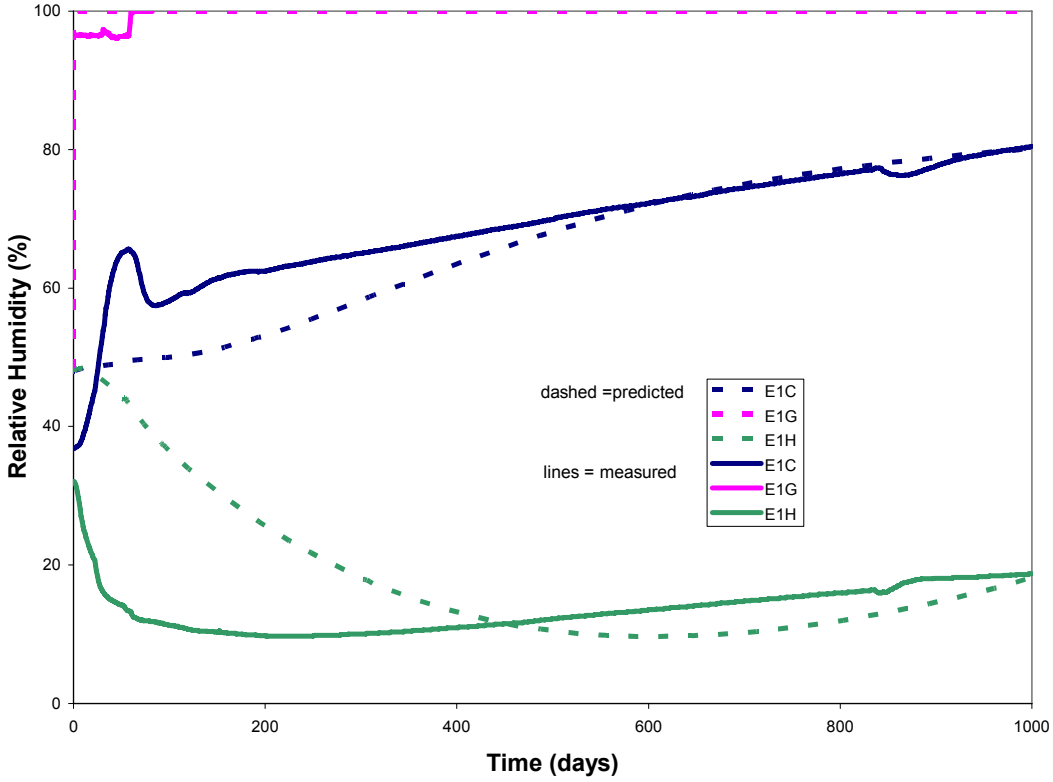

Figure 9-14. *Evolution of predicted and measured relative humidity with time at the following three points in section E1: E1H (radius 0.52 m), E1C (radius 0.81 m) and E1G (radius 1.10 m).*

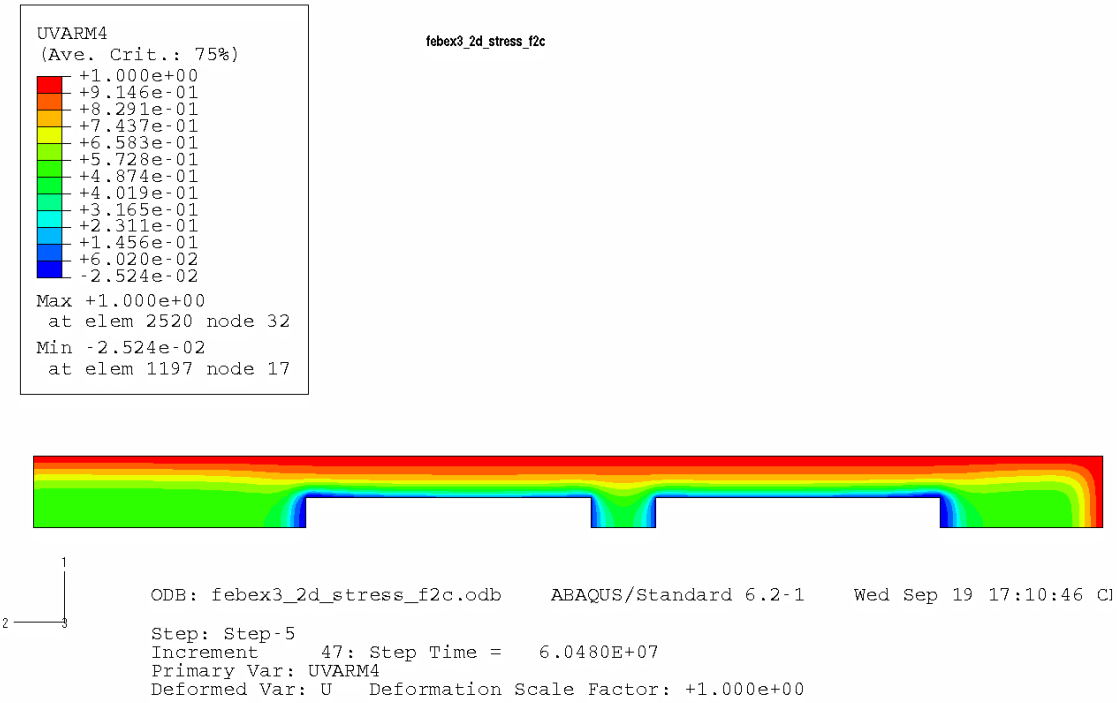

Figure 9-15. *Contour plot of the relative humidity after 1000 days.*

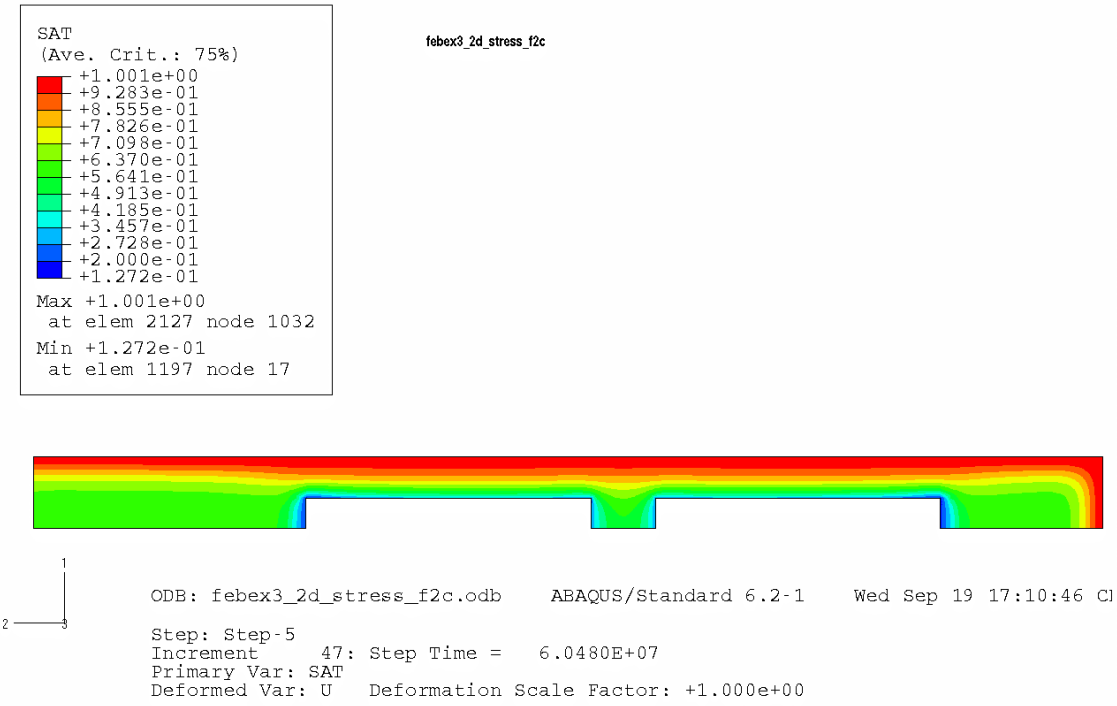

Figure 9-16. *Contour plot of the degree of water saturation after 1000 days.*

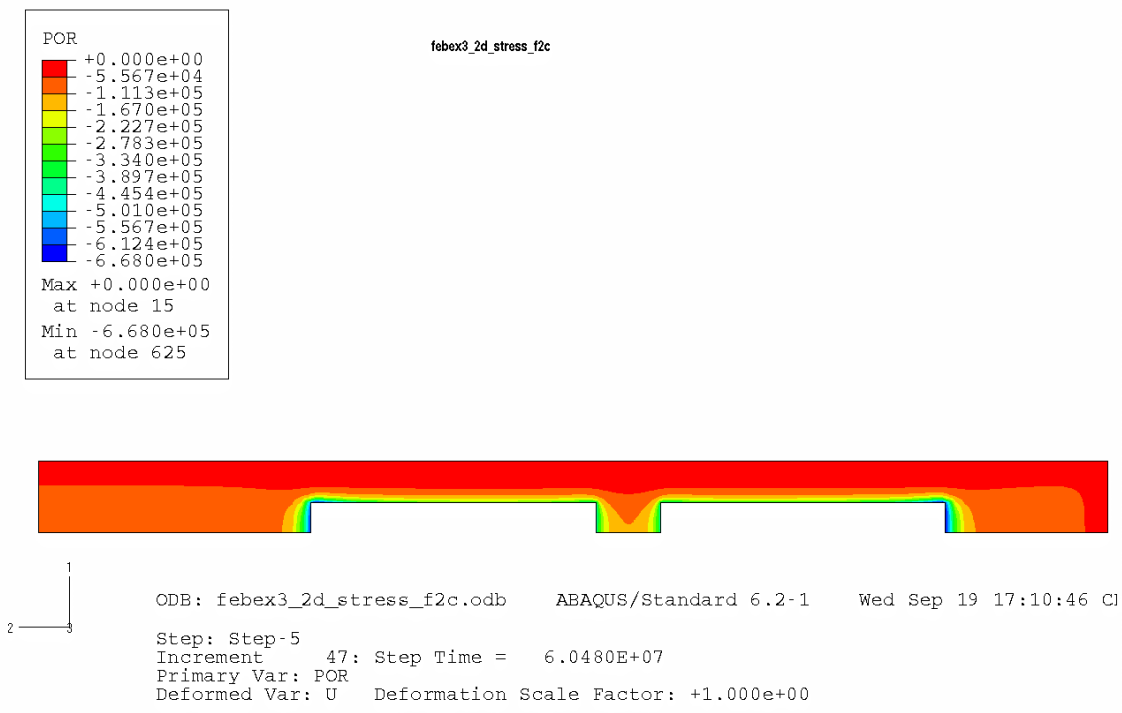

Figure 9-17. *Contour plot of pore water pressure (kPa) after 1000 days.*

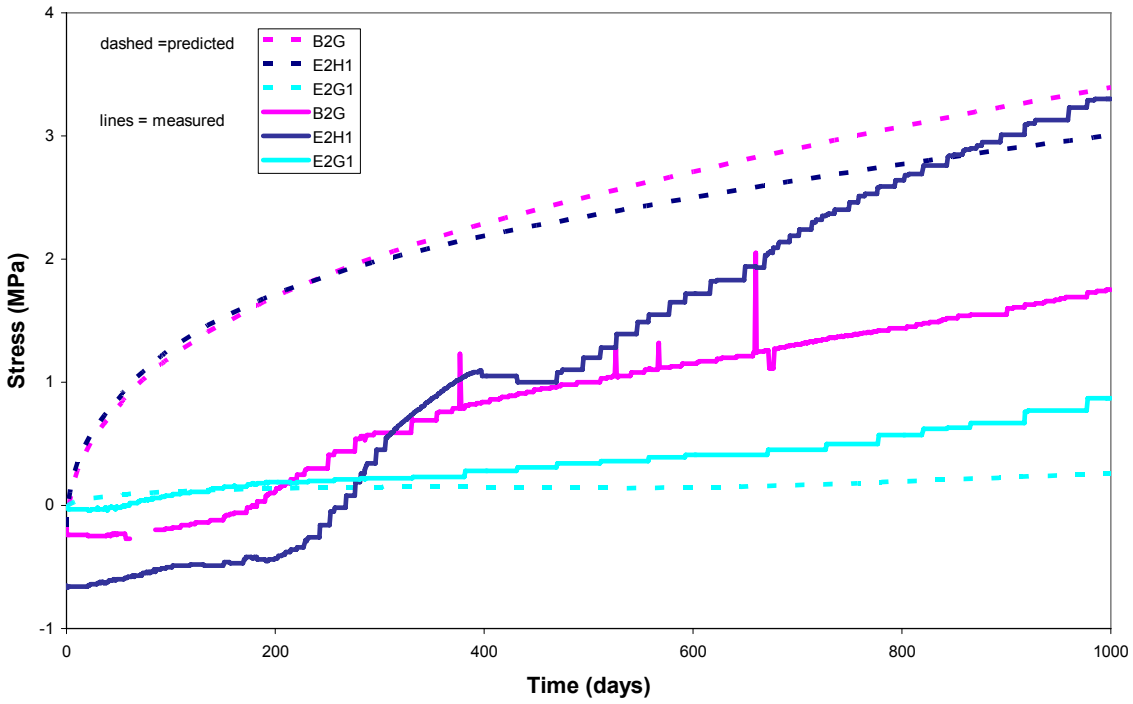

Figure 9-18. *Predicted and measured evolution of total radial stress with time at point E2G1 (radius 1.22 in section E2), at point E2H1 (radius 0.48 in section E2) and total axial stress with time at point B2G (radius 0.80 in section B2).*

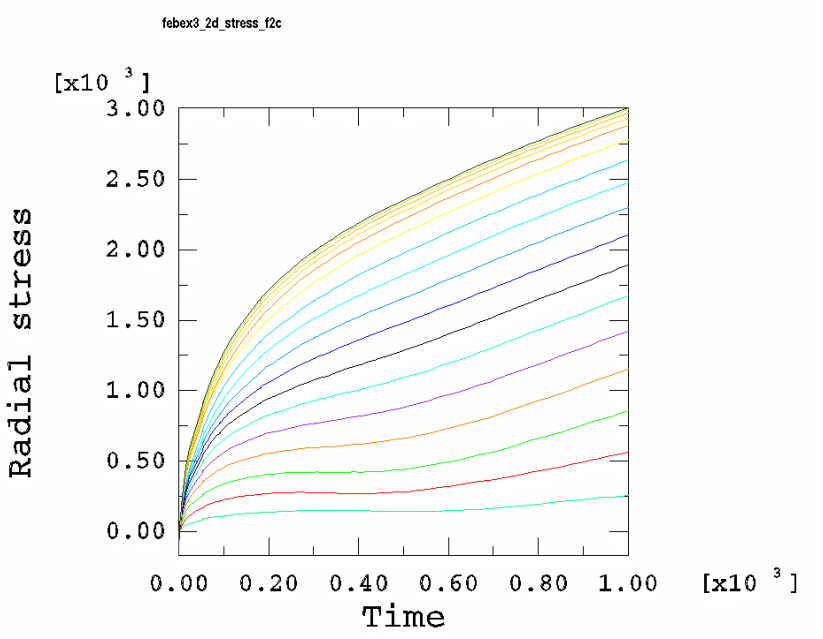

Figure 9-19. *Evolution of total radial stress (kPa) with time (days) for all elements in section E2.*

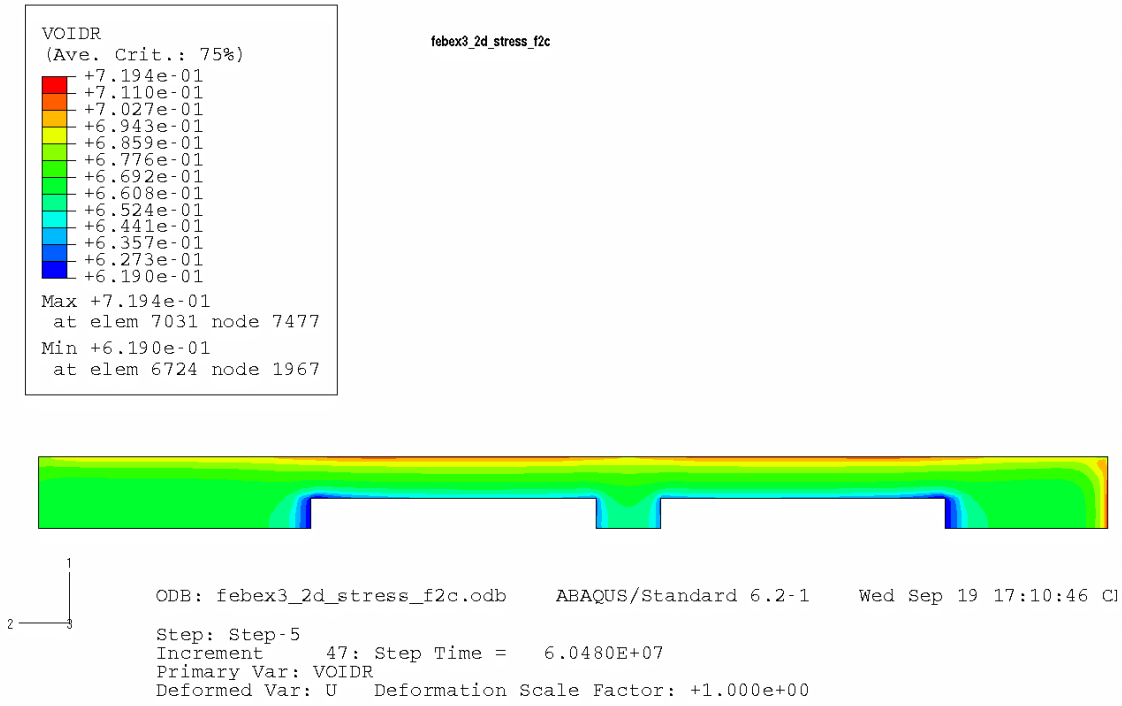

Figure 9-20. *Contour plot of void ratio in the entire cross section of the buffer after 1000 days.*

APPENDIX 2. Figures 11-1 to 11-13

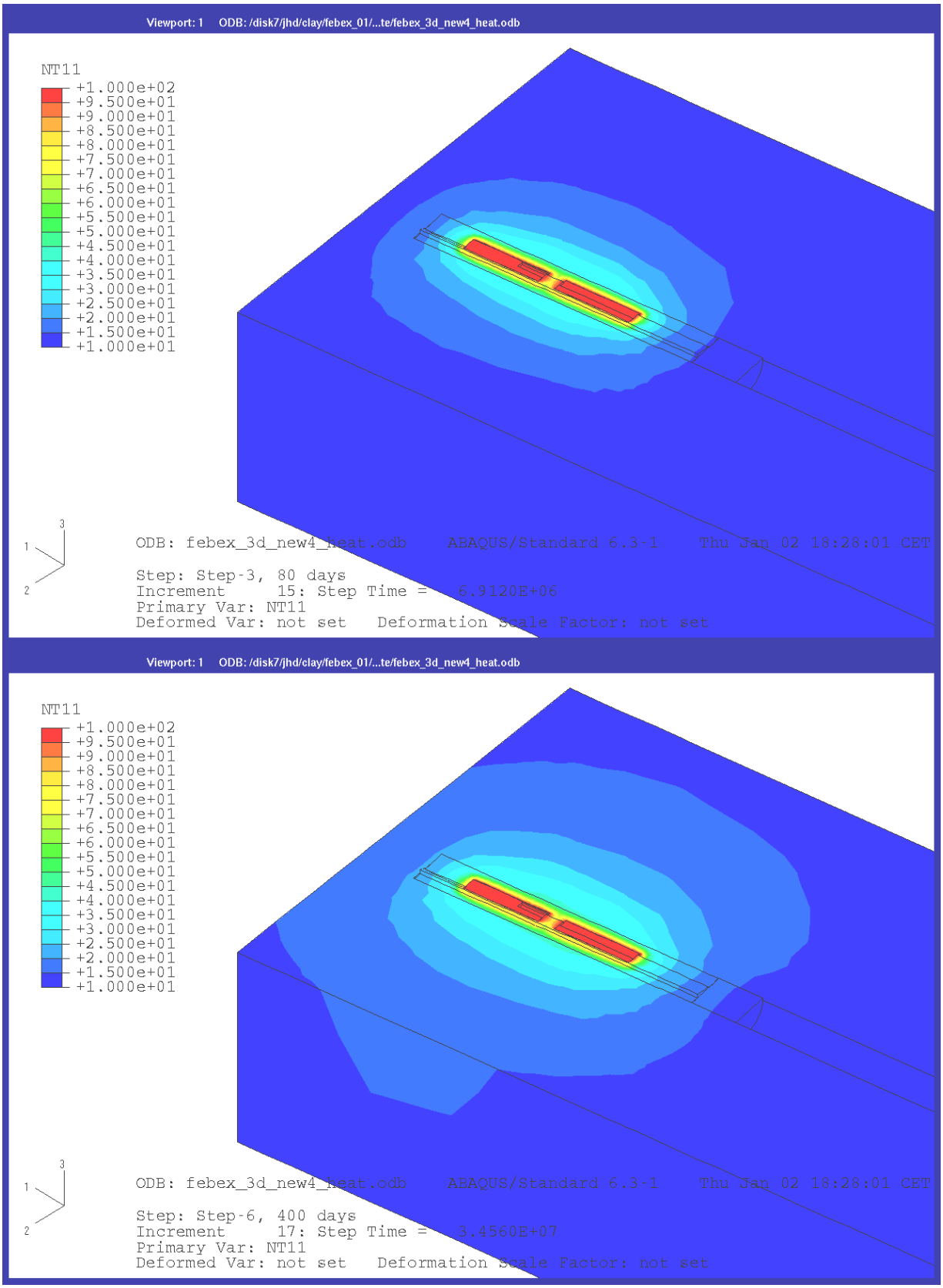

Figure 11-1. *Temperature distribution (˚C) in the near field rock and FEBEX tunnel (substructures 1 and 2) after 180 days (upper) and 1000 days.*

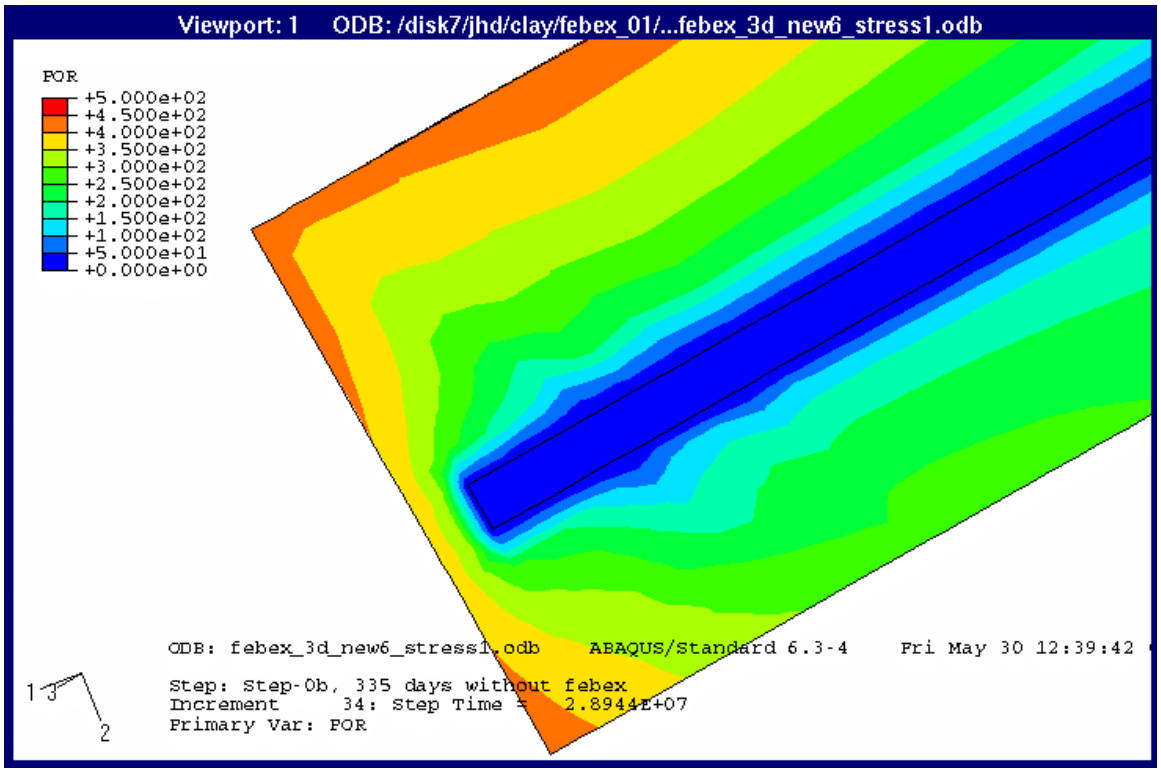

Figure 11-2. *Pore water pressure distribution (kPa) in the near field rock and FEBEX tunnel just before installation of the buffer.*

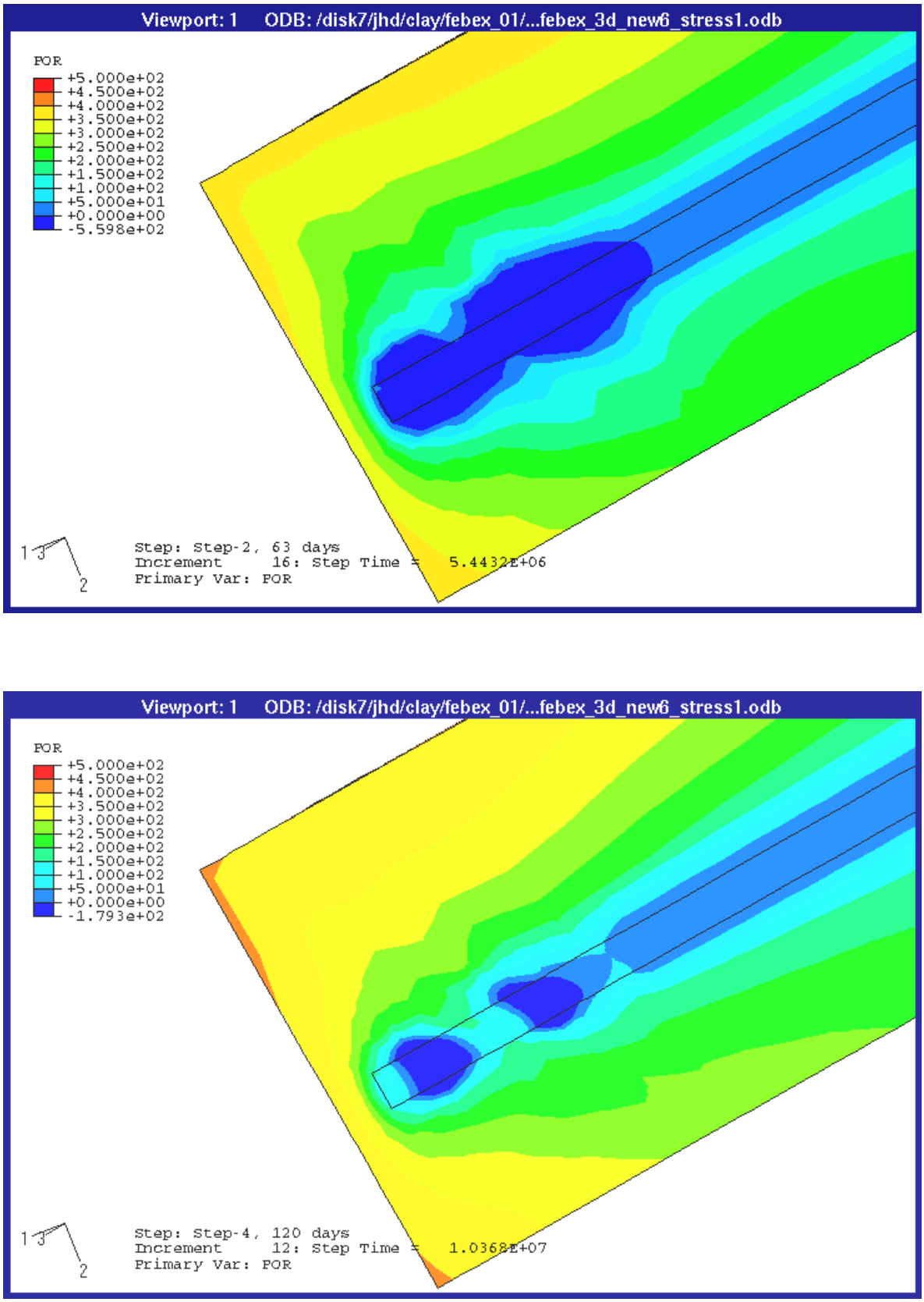

Figure 11-3. *Pore water pressure distribution (kPa) in the near field rock and in the rock surface of the FEBEX tunnel 100 days (upper) and 300 days after installation of the buffer.*

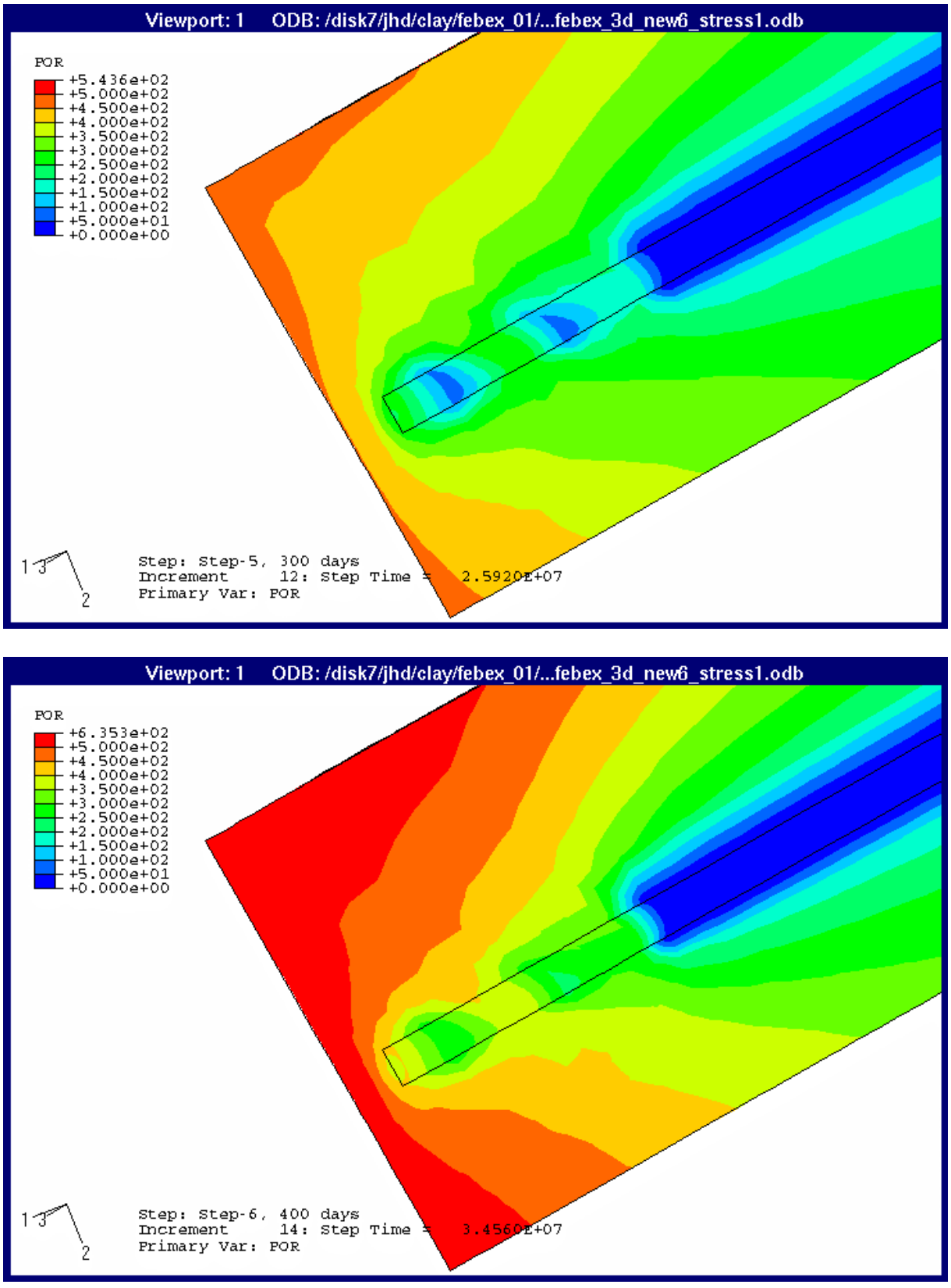

Figure 11-4. *Pore water pressure distribution (kPa) in the near field rock and in the rock surface of the FEBEX tunnel 600 (upper) and 1000 days after installation of the buffer.*

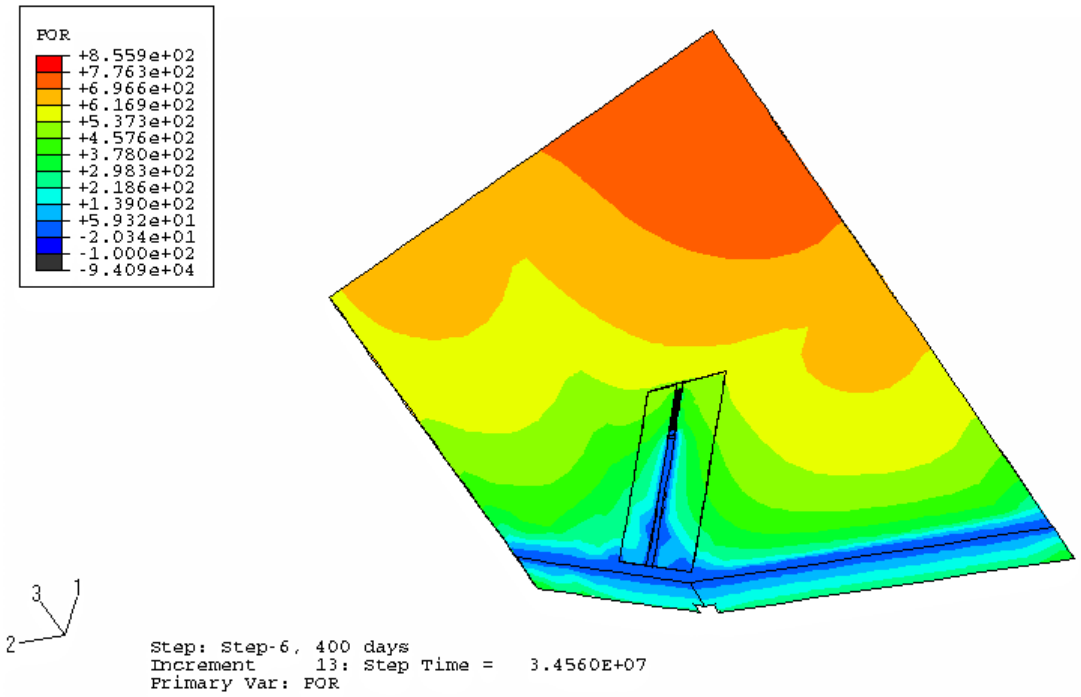

Figure 11-5. *Pore water pressure (kPa) in the rock in a horizontal section of the entire rock after 1000 days.*

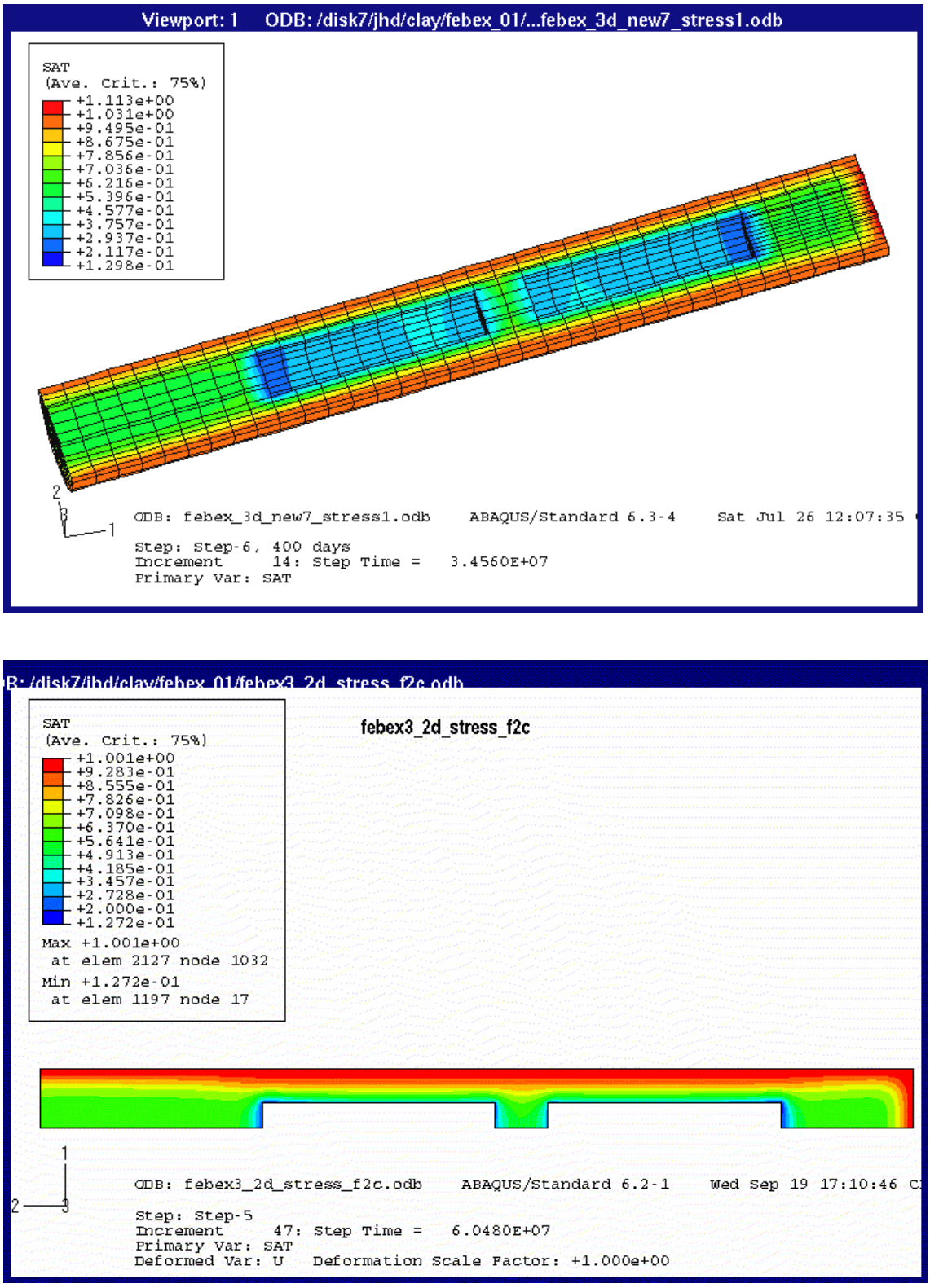

Figure 11-6. *Degree of water saturation of the buffer material after 1000 days according to the calculations of Task 1C (upper picture), with the large-scale 3D model of the entire rock and according to the calculations of task 1B (lower), with the 2D axial symmetric model of only the buffer.*

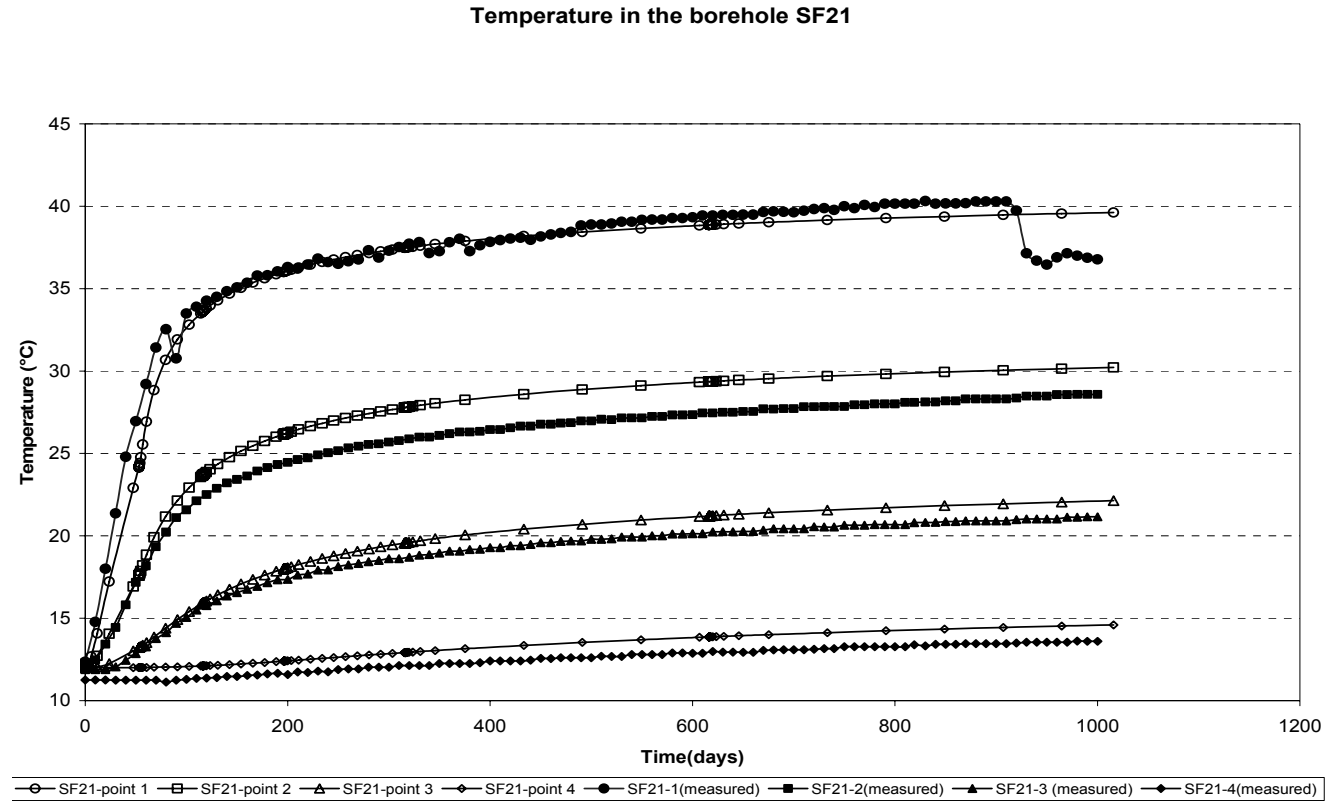

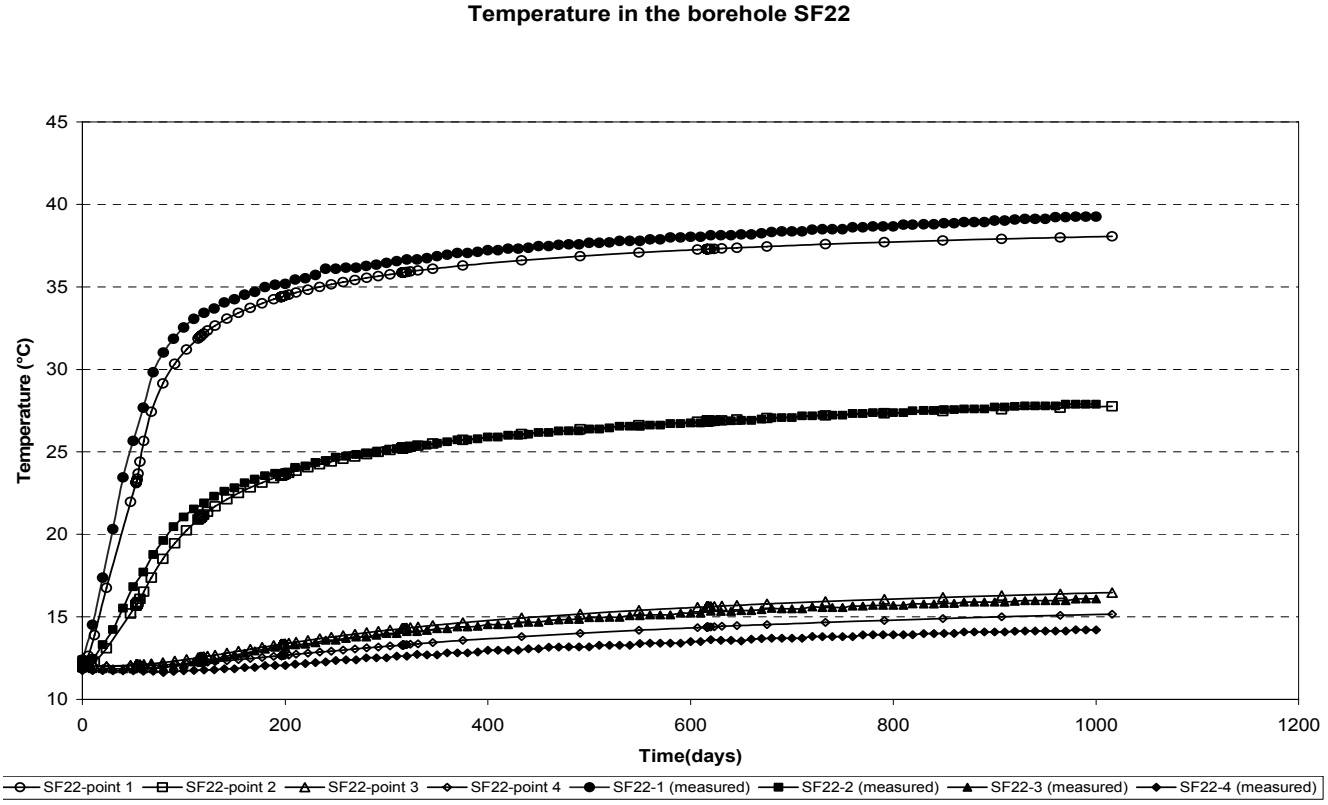

Figure 11-7. *Calculated and measured temperatures in boreholes SF21 and SF22. Open symbols are calculated results and filled are measured.*

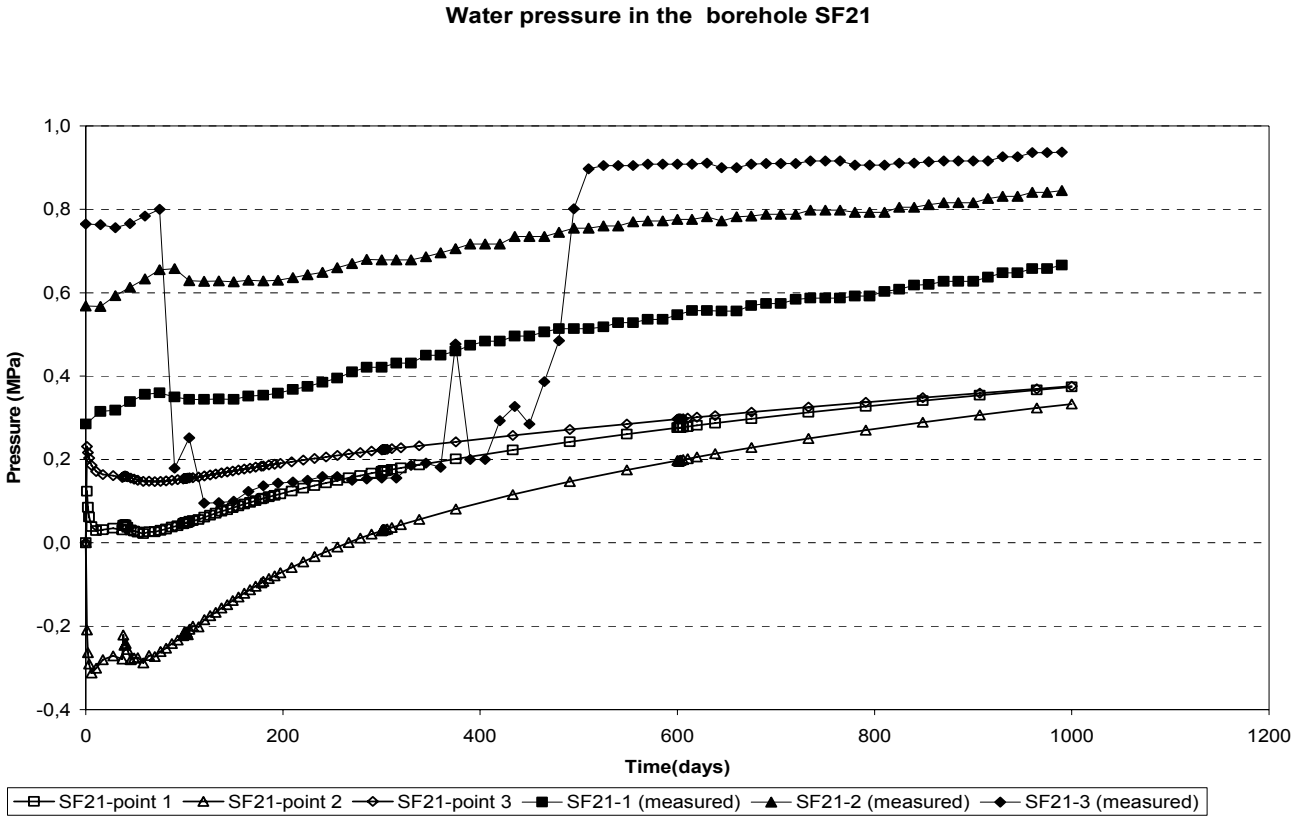

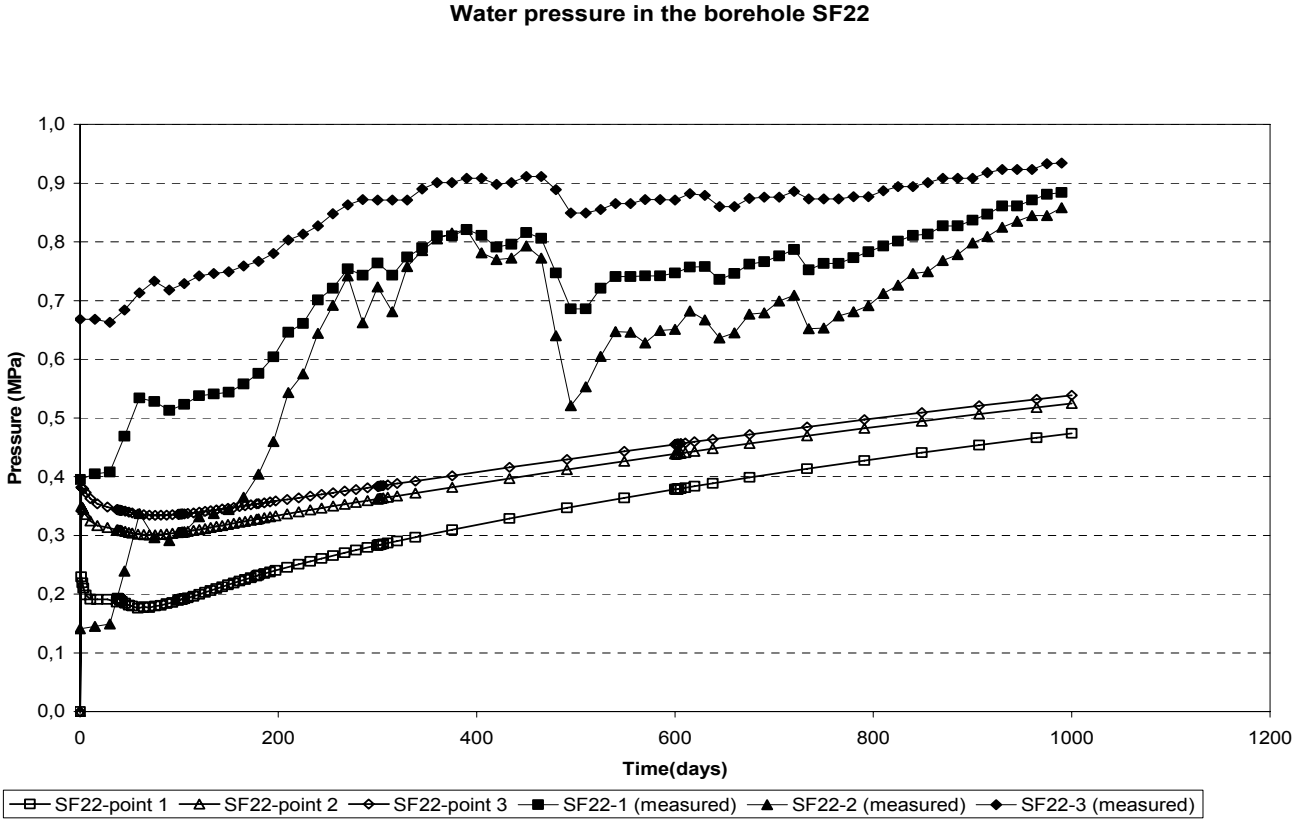

Figure 11-8. *Calculated and measured water pressure in boreholes SF21 and SF22. Open symbols are calculated results and filled are measured.*

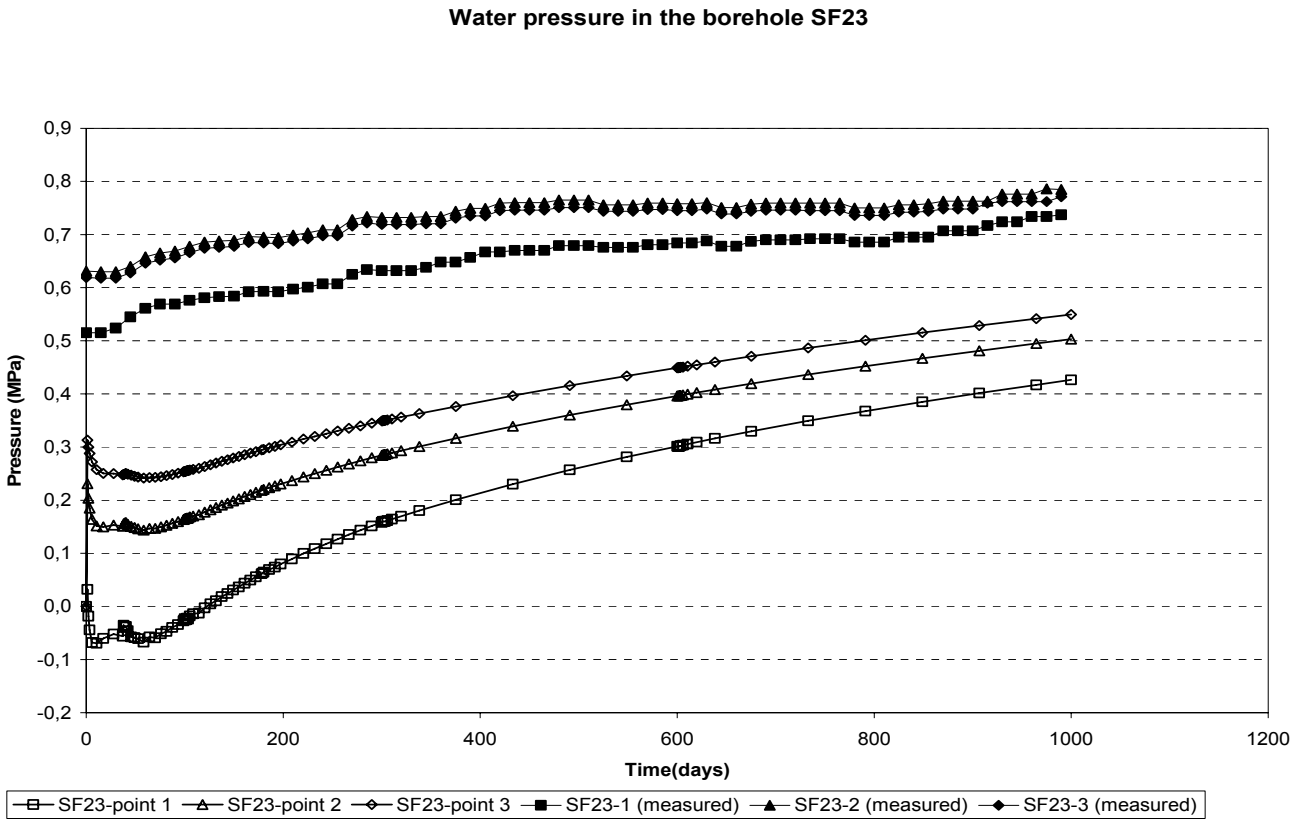

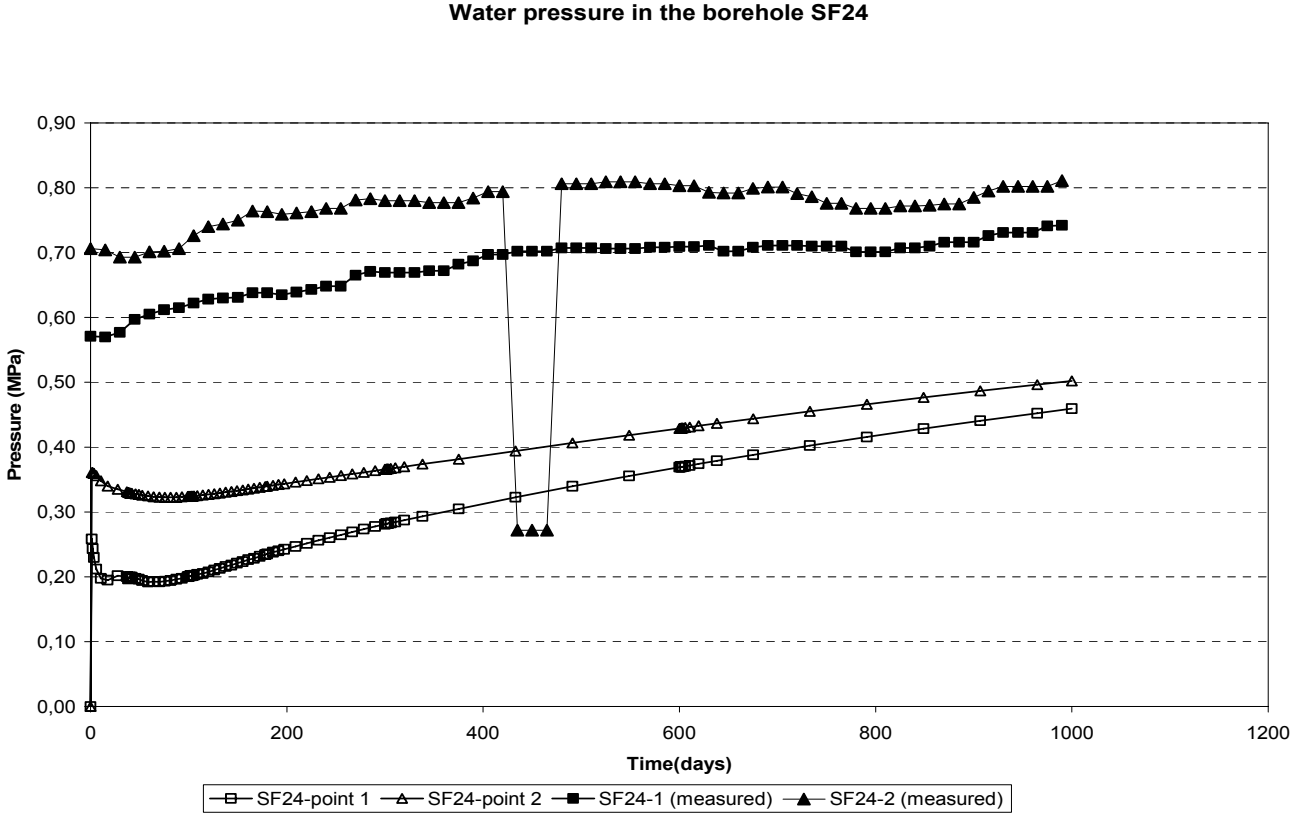

Figure 11-9. *Calculated and measured water pressure in boreholes SF23 and SF24. Open symbols are calculated results and filled are measured.*

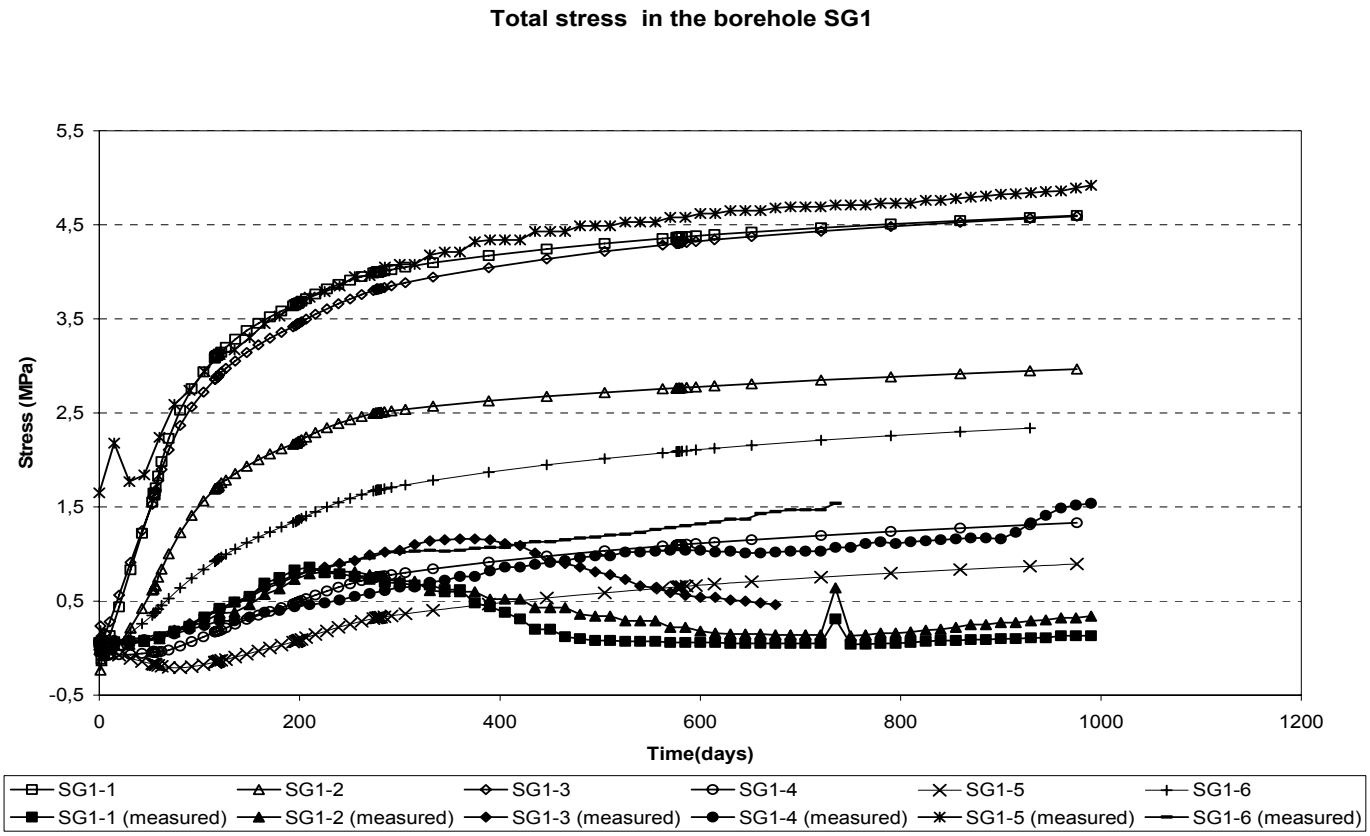

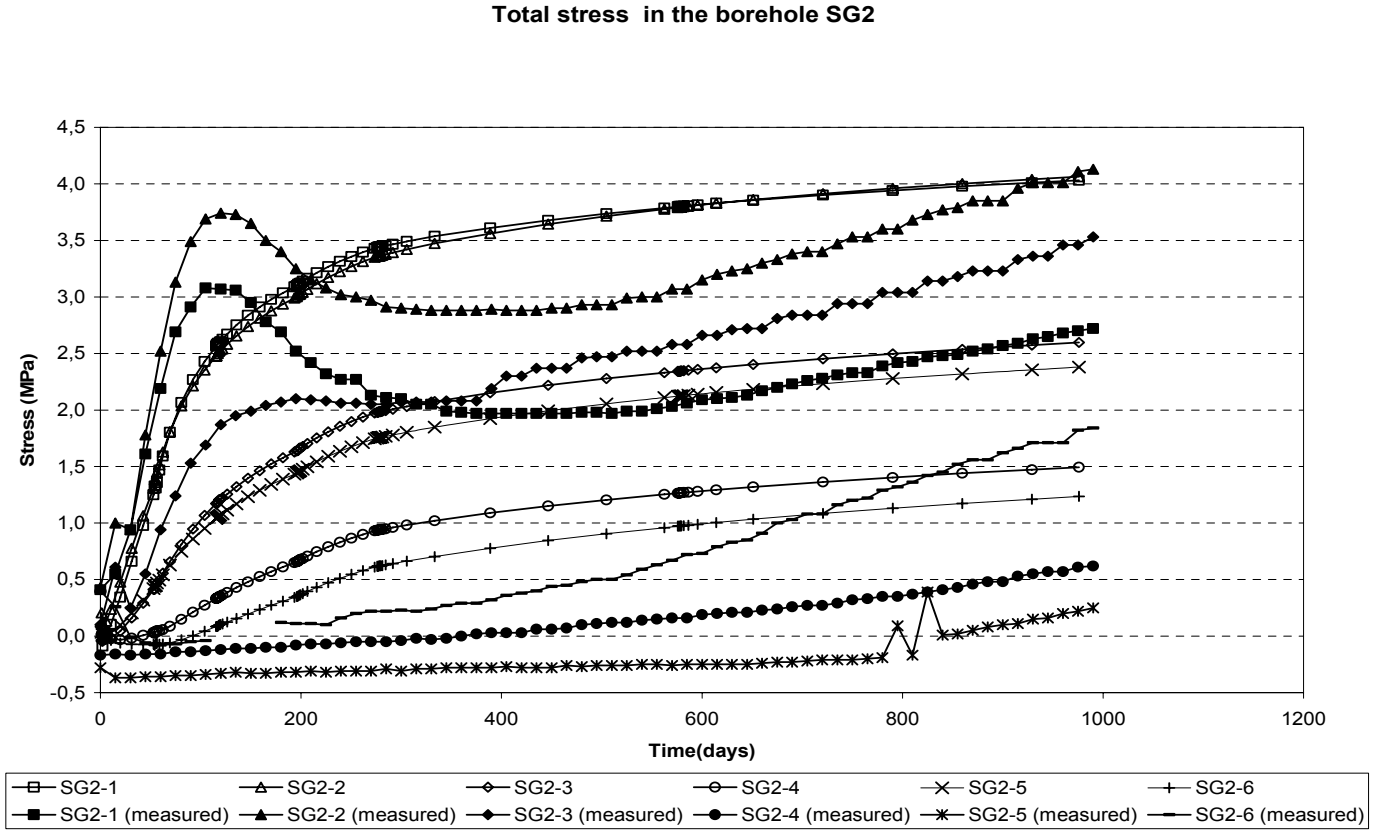

Figure 11-10. *Calculated and measured change in total stress in boreholes SG1 and SG2. Open symbols are calculated results and filled are measured.*

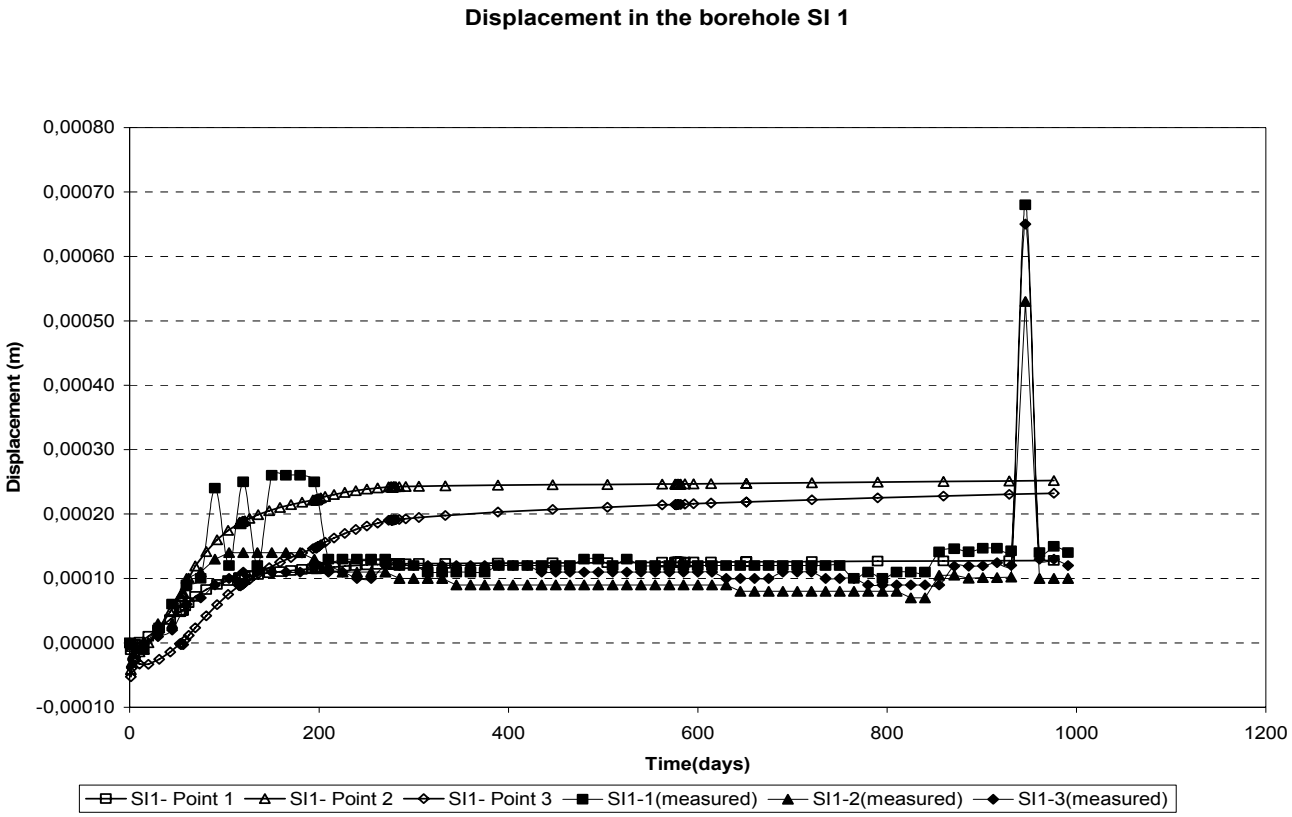

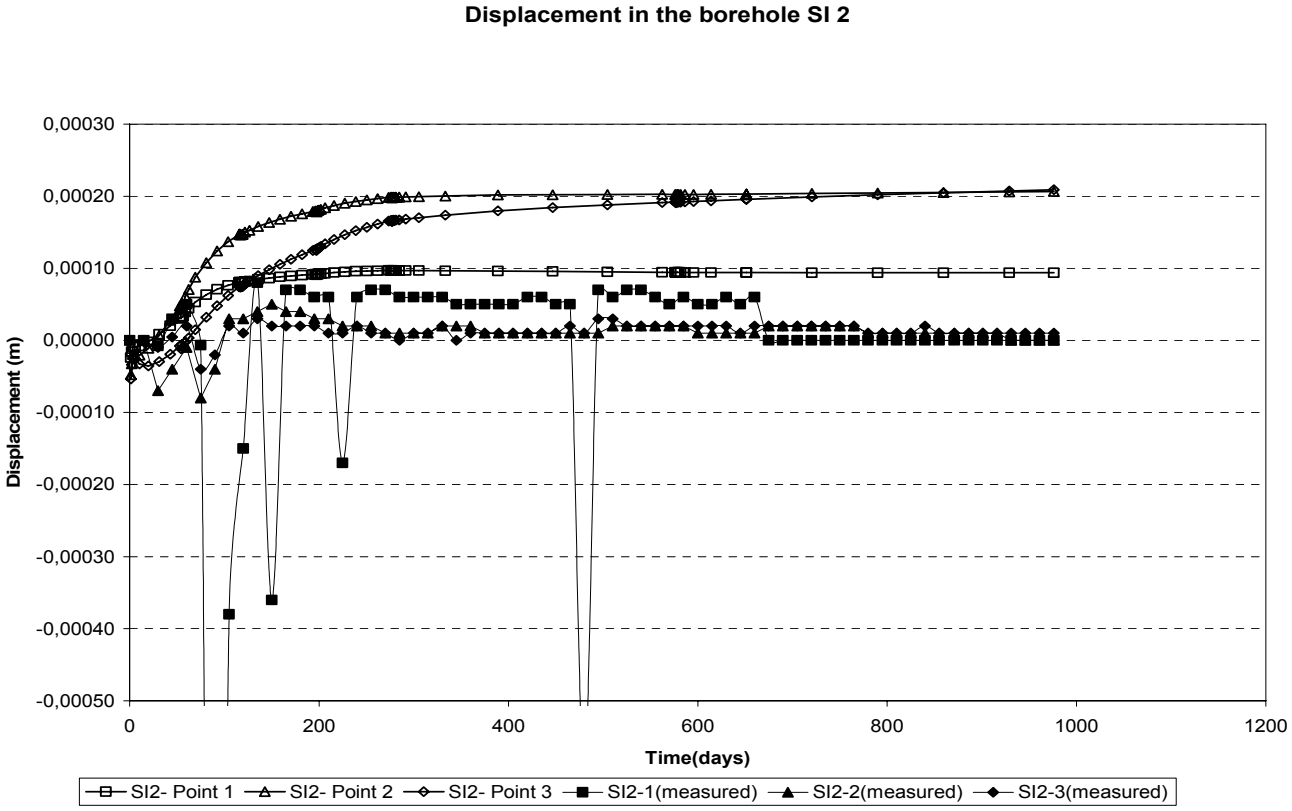

Figure 11-11. *Calculated and measured displacements in boreholes SI1 and SI2. Open symbols are calculated results and filled are measured.*

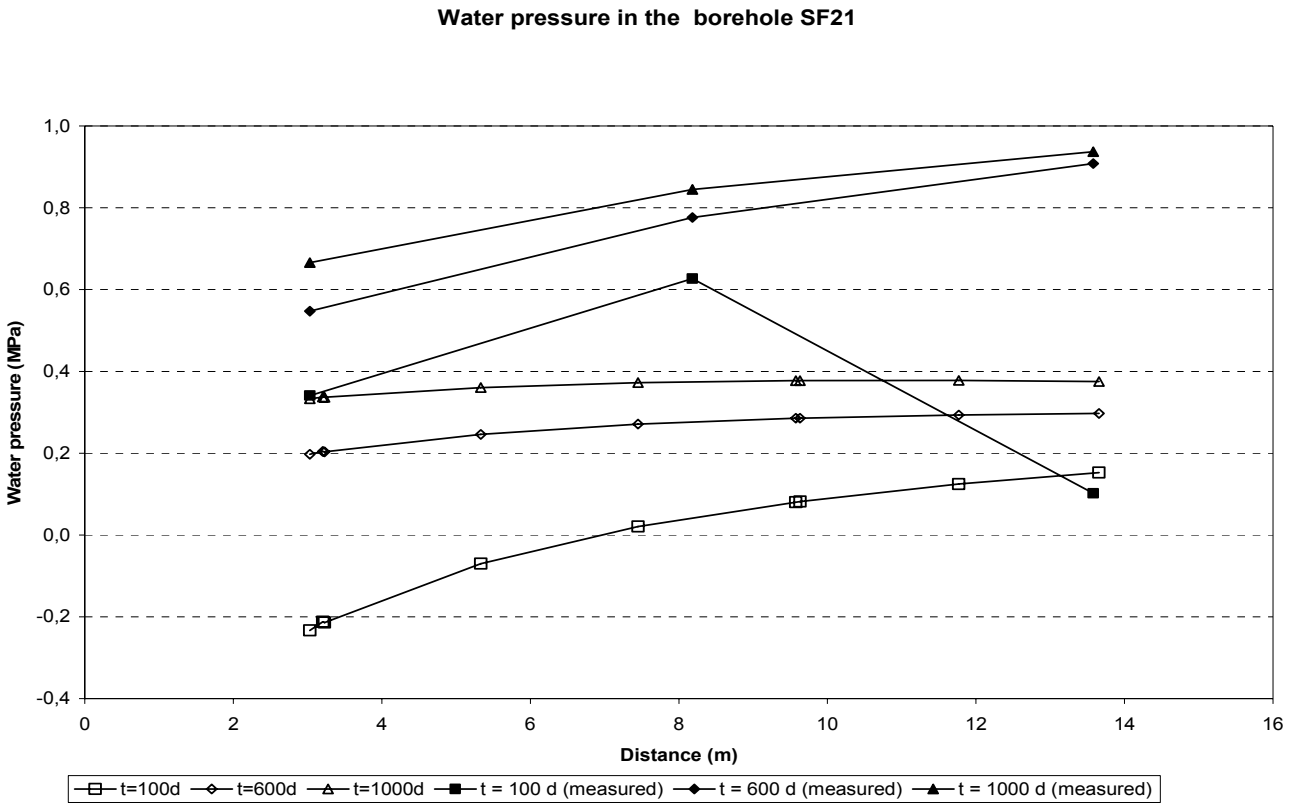

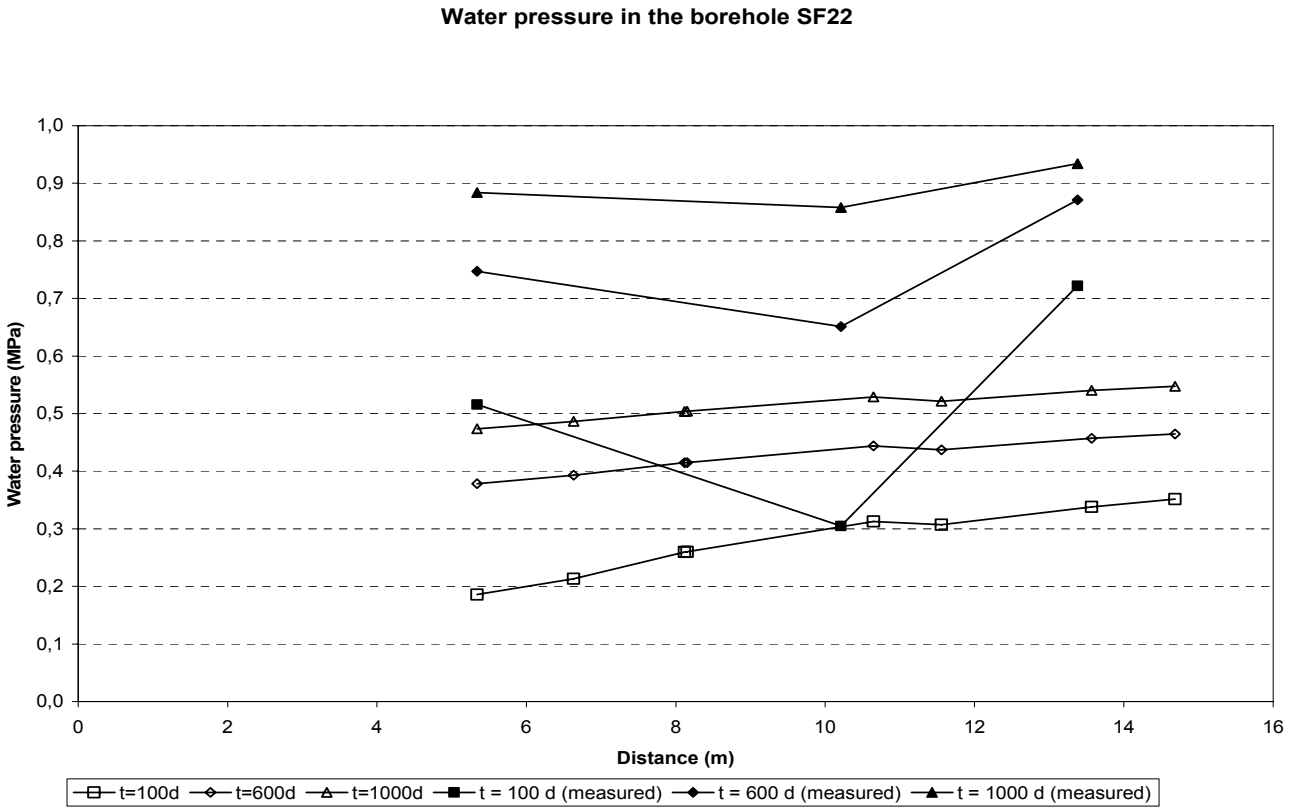

Figure 11-12. *Calculated and measured water pressure in boreholes SF21as a function of the z-coordinate and in borehole SF22 as a function of the y-coordinate. Open symbols are calculated results and filled are measured.*

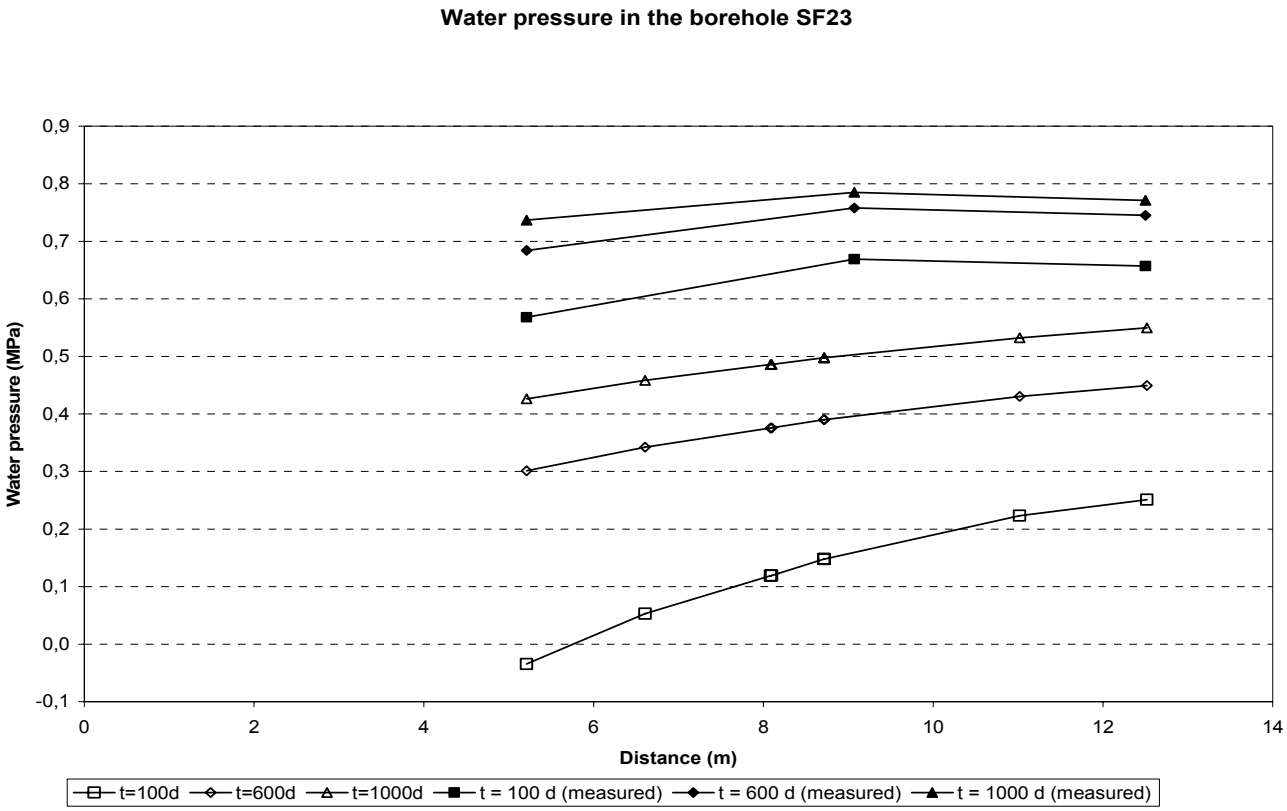

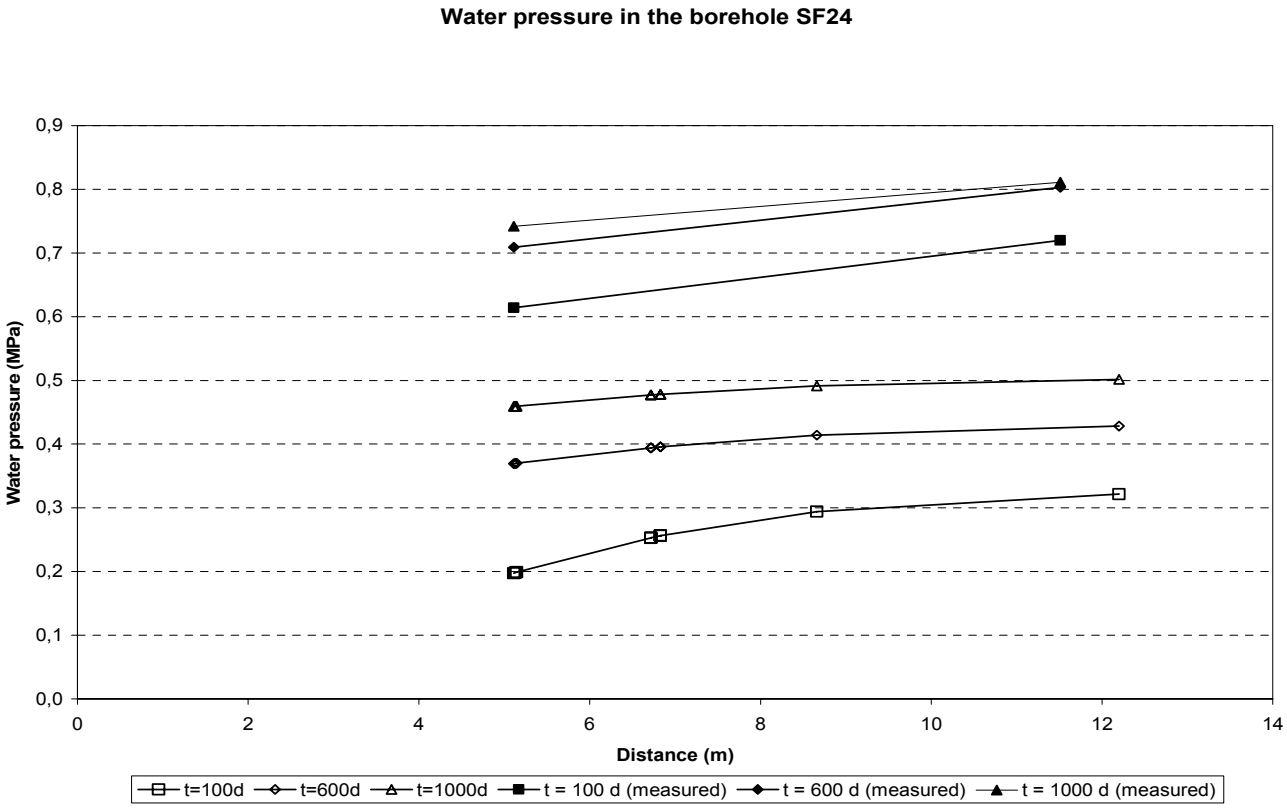

Figure 11-13. *Calculated and measured water pressure in boreholes SF22as a function of the z-coordinate and in borehole SF23 as a function of the y-coordinate. Open symbols are calculated results and filled are measured.*

APPENDIX 3

CONCEPTUALISATION OF GEOLOGICAL FEATURES AT THE FEBEX SITE FOR GROUNDWATER FLOW MODELLING

DECOVALEX III TASK 1: MODELLING OF

FEBEX IN-SITU TEST

Jan-Erik Ludvigson

GEOSIGMA AB

Foreword

This document is prepared as a basis for the modelling exercise in DECOVALEXIII, Task 1:Modelling of FEBEX in-situ test at the Grimsel Test Site, Switzerland.

Contents

1 Introduction and scope

In the modelling exercise in DECOVALEX III, Task 1:Modelling of FEBEX in-situ test, Swedish Nuclear Fuel and Waste Management Co (SKB) is one of the partners, represented by Clay Technology.

The main object of this paper is to identify and characterise the most important geological features to be included in hydrogeological models of the FEBEX site scale and –experimental scale. In addition, the overall piezometric head conditions together with suggested initial conditions for the modelling are described.

An introduction to the DECOVALEX III: Task 1 together with basic data for the modelling has been compiled in a report to the partners called GENERAL SPECIFICATIONS. This document is called GS below.

In addition, selected reports were provided to each partner as further information to the modelling exercise. In some of the reports, certain chapters were excluded to hide pertinent information to the partners. These reports are listed at the end of this report.

2 Overview of the geology of the Grimsel and Febex area

The Grimsel Test Site is located at an elevation of 1730 m above sea level, about 450 m beneath ground surface in granitic rocks. A horizontal access tunnel (KWO tunnel), c. 1.2 km long, leads to the Grimsel Test Site (GTS). The GTS tunnel system includes a laboratory tunnel with a total length of almost 1000 m and test caverns and drifts. The laboratory tunnel has a diameter of 3.50 m.

The FEBEX area is located in the northern part of the Grimsel Test Site between the boreholes BOUS-85001 and –85002, see plan view in Figure 2-1 (plan at the level of GTS). Observe the North direction in this figure. The FEBEX drift is drilled with TBM (diameter 2.28 m) from the GTS-tunnel and located between the more recent boreholes FBX-95001 and FBX-95002, the tunnel being parallel to the latter borehole. The length of the tunnel is c. 70 m. The inner part of the drift has been explored by 19 shorter boreholes ("in-drift boreholes").

2.1 Regional geology at the Grimsel area

Figure 2-2 shows the major geological features in a surface exposure including the topographical conditions (contour 100 m) on a regional scale. Figure 2-3 shows a geological cross section of the Grimsel area with the major geological structures in relation to the KWO- (access tunnel) and GTS tunnels. According to GS, p.16, the FEBEX drift is located at the northern end of the GTS-tunnel and bounded by two main shear zones according to Figures 2-2 and 2-3. According to GS, p.28, "the most important geological features at the FEBEX drift area are two shear zones. Such shear zones constraint regional groundwater flow due to their "high" transmissivity and therefore, they constitute boundaries of the FEBEX environment". These two zones are below also called the Northern (N) and Southern (S) shear zone, respectively. The distance between these zones is about 150 m.

2.2 Local geology at the FEBEX area

The main features of the interpreted geological conditions in the FEBEX area are shown in Figure 2-4. The host rock consists of granites of different facies (Granite Aare). In this part of the Grimsel area, two fracture systems are the most important, i.e. the S1 +S2-system (shear zones) and the K2 +L-(and K1+L2)-system. The latter fracture zones are associated with dikes of lamprophyre which are important from a hydraulic point of view. According to Pardillo (1997) the average orientations of these fracture systems are:

S1: strike/dip: N50E/80E $\Rightarrow$ dip direction/dip: 140/80

S2: strike/dip: N65E/75E $\Rightarrow$ dip direction/dip: 155/75

Thus, it only differs 15 degrees in strike of these two fracture sets. The strike (and dip direction) of the other fracture system in the area is generally:

K2 + L: strike: N110-135E ⇒ dip direction: 200-225

K1 + L2: strike: N135-150E ⇒ dip direction: 225-250

The latter zones have a sub-vertical dip (80-90W). According to GS (p.16) the following geological features are considered relevant for regional groundwater flow:

shear zones of strike/dip: N50-60E/80-90E and

fracture zones and lamprophyre dikes of strike/dip: N115-130E/80W

Thus, the two sets of fracture systems are almost perpendicular and sub-vertical.

According to GS, p.16, shear zones are of considerable thickness at the area (5-20 m). At the intersection with tunnels, they display major outflows indicating their relevance as preferential flow paths. Lamprophyre dikes have also considerable thickness (up to several meters). A preferential flow path within these dikes is the contact surface between the lamprophyre and the host rock. Thus, concentrated outflows have been observed at these surfaces at their intersections with the tunnels and drifts. Both shear zones and lamprophyres are traceable from tunnels to surface outcrops. Some of the thickest lamprophyre dikes contain smaller fractures parallel to the dikes. Thus, the hydraulic conductivity of the dikes may be anisotropic. Perpendicular to the dike direction the hydraulic conductivity of the dikes is low.

Figure 2-5 shows the main local geological features observed in the tunnels and borehole cores. As stated in GS, p. 20 “In this figure, the N boundary of the FEBEX does not show up. However, the S boundary can be easily deduced by the density of fractures, which constitute the shear zone”. The latter zone intersects borehole BOUS-85002 at c. 10 m with a c. NE direction. Also, the lamprophyres involved (black) can be traced between the FEBEX drift and the GTS tunnel. Such dikes also intersect borehole FBX-95002 at c. 50 m (NW-fractures). Furthermore, a shear-breccia zone intersects the latter borehole at c. 25 m and the FEBEX tunnel at c. 20 m. The latter two features are very important from a hydraulic point of view, see below.

It is uncertain if the Northern shear zone is intersected by borehole BOUS-85001 (it is not stated explicitly in any of the listed reports). However, according to Pardillo et al (1997) it is probable that the Northern shear zone intersects this borehole.

Figures 2-6 and 2-7 in GS show geological maps of the FEBEX drift between 0.0 and 70.0 m and a detailed map of 50.5- 70.0 m, respectively. The figures show that the shear-breccia zone intersects the drift at c. 20 m and that lamprophyre dikes occur at c. 55 m (0.25 m thick) and at c. 60 m (c. 1.5 m). Both the shear-breccia zone and the dikes are sub-vertical.

3 Most important geological features at the Febex area

Based on a synthesis of all available material, Guimera et al. (1998) identified the following geological features, which are considered relevant for groundwater flow at the Febex site scale and experimental scale. These features are shown in Figure 2-4.

3.1 Febex site scale

- **The N and S shear zones**, which constitute outer boundaries to the FEBEX site. They are of regional relevance and inflows towards the KWO and GTS tunnels are important, indicating relatively "high" transmissivity. The thickness of these zones ranges from 10 to 20 m at the tunnel intersections. The S shear zone is well exposed at the GTS tunnel and also intersects at c. 10 m in BOUS-85002. The N shear zone only intersects the KWO tunnel (N of the GTS tunnel). The measured inflows at the tunnel intersections of these zones are shown in Table 6-1.

- **The shear-breccia zone** intersected by the FEBEX-drift at c. 20 m and by boreholes FBX-95001 and 95002, BOUS-85002 and by in-drift borehole SF24. Its hydraulic importance was manifested by hydraulic interference tests and during the construction of the FEBEX drift. Once the TBM intersected this structure, the pressure in borehole intervals dropped to almost atmospheric pressure. The inflows at the FEBEX drift is important, see Table 6-1.

- **Lamprophyre dikes**, especially that intersected at c. 55 m in the FEBEX drift. The contact surface between the dikes and the host rock constitute preferential flow paths. One of the dikes intersects borehole BOUS-85002 at c. 10 m (as the S shear zone). Thus, the dike system is connected to at least one of the bounding shear zones.

- **Granite rock mass**. Constitutes the host rock. It is affected by several (internal) fracture systems forming a rather complex fracture network. However, the suggested model approach (continuum model with discrete fracture zones) prevents from a discrete characterisation of the host rock. Due to the general shistosity of the rock (sub-vertical) the hydraulic conductivity in the vertical direction is likely to be increased, c.f. Table 6-1.

3.2 Febex experimental scale

At the scale of the FEBEX experiment, two additional small-scale fractures should be included according to Guimera et al. (1998).

- "En-echelon" fracture intersected at c. 52 m of the drift. The fracture has proven to be relevant during cross-hole tests in the in-drift boreholes and during seepage monitoring at the FEBEX drift (Guimera et al., 1998).

- "Normal" fracture intersected by in-drift borehole section SJ5-3 and SB23-1, see Figure 2-1. Like the above fracture, this fracture is only relevant for flow at a very local scale. Its extension is few metres, yet it does not intersect surrounding boreholes at the bottom of the drift such as FBX-95002. It is likely connected to a fracture zone which appears at the bottom, left parament of the drift, whose inflows presented some problems during bentonite placement (Guimera et al.,1998).

4 Conceptualisation of most important geological features at the Febex area

4.1 Febex site scale

A simplified conceptualisation of the most important geological features for groundwater flow modelling at the Febex site is presented in Appendix 1. The conceptual model is based on the geological interpretation in boreholes and in the Febex tunnel by Pardillo et al., (1997) and the identification of the most important geological features in modelling (Guimera et al., 1998). The location of the bounding Northern shear zone is uncertain. In the conceptual model the latter zone is assumed to be parallel to the S shear zone and located at a distance of c. 150 m from this zone. Only two of the lamprophyre dikes are included in the model. It should be observed that the intersections of the geological features with the boreholes and tunnels are not exact in Appendix 1 but only approximate. Otherwise, the figure is to scale.

The KWO tunnel constitutes the Eastern boundary of the model. The Western boundary is uncertain. It is assumed that all fracture zones and dikes extend to the model boundaries. The orientation of the features is given as strike/dip with a dip of 90 degrees corresponding to the vertical.

4.2 Febex experimental scale

Possible conceptualisations of the additional small-scale fractures described in Section 3.2 are shown in Appendix 2. Also selected "in-drift" boreholes are shown. The conceptualisations of the fractures are consistent with the information provided by the geological core mapping of the in-drift boreholes and the tunnel mapping reported by Pardillo et al. (1997), c.f. Figure 2-7 together with the information from the interference tests reported by Guimera et. al (1998). However, other (similar) conceptualisations are also possible. All fractures have been conceptualised as circular discs, concentric to the center axis along the Febex tunnel. The radii of the fractures are uncertain but are adjusted (minimised) in order to obtain intersection with the actual in-drift borehole sections reported by Guimera et al. (1998) for the interference tests.

The conceptualised "en-echelon" fracture is located at c. 57 m in the (center of the) tunnel between the two lamprophyre dikes with a strike of c. N155E and a dip of c. 70° towards W. This orientation is similar to the orientation of the dikes. The radius of the fracture is chosen in order to intersect the actual in-drift borehole sections SF14-3, SK2-2 and SF13-2 together with borehole section FBX-2-4 as reported by Guimera et al. (1998). The minimal radius of the fracture is thus c. 10 m.

The “normal” fracture was conceptualised as an almost vertical plane, located at a distance of c. 1 m in front of (and normal to) the tunnel. The assumed strike of the fracture is c. N170E (almost N-S), the dip c. 80° towards E and a radius of at least 7 m. This fracture intersects in-drift borehole sections SJ5-3 and SB23-1 as reported during the interference tests by Guimera et al (1998). The normal fracture is assumed to be intersected by another fracture, located in the tunnel at c. 69 m. The assumed strike of the latter fracture is N120E and the dip c. 25° towards W. The radius of the connecting fracture is assumed to be at least 5 m. The orientations and extension of the interpreted fractures are shown in Table 4-1.

Table 4-1. Orientations and extension of the assumed fractures in Febex experiment scale. Intersection with tunnel refers to the position along the center axis of the tunnel.

Fracture	Dip/strike	Intersection with tunnel (m)	Minimal radius of fracture (m)
En-echelon	N155°E/70°W	57	10
Normal	N170°E/80°E	72.5	7
Connecting fracture to Normal	N120°E/25°W	69.5	5

5 Piezometric head conditions at the Febex area

5.1 Febex site scale

Previous regional modelling has evidenced that topography is the main diving force for groundwater flow at the Grimsel area (GS, p.24). The topography is shown in Figure 2-2. The piezometric head values in intervals of the long boreholes around the Febex drift, measured before and after the drilling of the drift, together with the estimated transmissivity of the intervals are listed in Table 5-1. Borehole FEBEX 95.002 was re-instrumented after the drilling of the drift. The orientation (strike/dip) of the BOUS boreholes is N290°E/15°W (sub-horizontal), both holes being 150 m long. The strike (azimuth) of FEBEX 95.001 and –95.002 is N275°E and N258°E, respectively. Both holes are approximately horizontal. The holes are 76 m and 132 m long, respectively.

The hydraulic head differences measured along borehole BOUS-85002 exceed 200 m over 150 m length which corresponds to a hydraulic gradient of 1.3 from the GTS tunnel into the rock if parallel flow is assumed (Guimera et al., 1998). Table 5-1 shows that the drilling of the drift only had a slight effect on the piezometric head in these boreholes.

5.2 Febex experimental scale

According to Guimera et al. (1998) the piezometric head distribution at the experiment scale is affected by both the regional flow regime and by the presence of the access and GTS tunnels and the Febex drift, the latter being more important. Regional flow is directed towards N-NW in a plan view. Figure 5-1 shows the observed piezometric head distribution around the Febex tunnel in a plan view and in a cross section.

Table 5-1. Results of hydraulic measurements at BOUS and FEBEX boreholes. T=transmissivity, h1=piezometric head measured before drift construction, h2= piezometric head measured after drift construction. From General Specifications (Table 6-1).

Interval (m)	T (m^2/s)	Head h1 (m)	Head h2 (m)
BOUS 85.001			
I1 (83.50-150.00)	$3.6 \cdot 10^{-10}$	1983.0	-
I2 (73.00-82.50)	$3.2 \cdot 10^{-9}$	1777.3	1778.6
I3 (11.50-72.00)	$3.9 \cdot 10^{-10}$	1759.5	1758.5
(1.00-150.00)	-	1783.6	-
BOUS 85.002			
I1 (114.00-150.00)	$8.3 \cdot 10^{-10}$	1909.3	1922.2
I2 (111.00-113.00)	$2.8 \cdot 10^{-8}$	1830.1	1852.9
I3 (90.00-110.00)	$2.7 \cdot 10^{-9}$	1818.6	1843.1
I4 (60.00-89.00)	$7.0 \cdot 10^{-8}$	1781.6	1783.0
I5 (54.00-59.00)	$1.6 \cdot 10^{-8}$	1791.0	1791.8
I6 (13.00-53.00)	$1.3 \cdot 10^{-7}$	1745.8	1745.4
(1.00-150.00)	-	1745.6	-
FEBEX 95.001			
I1 (67.00-76.70)	$3.3 \cdot 10^{-10}$	1788.5	1794.0
I2 (56.00-66.00)	$8.2 \cdot 10^{-11}$	1776.8	1778.5
I3 (42.00-55.00)	$6.8 \cdot 10^{-11}$	1772.2	1771.7
I4 (20.00-41.00)	$1.4 \cdot 10^{-10}$	1757.1	1748.1
I5 (8.00-19.00)	$>2.0 \cdot 10^{-7}$	1747.2	1731.1
FEBEX 95.002			
I1 (105.50-132.00)	$5.3 \cdot 10^{-10}$	1889.8	-
I1 (84.00-132.00)	-	-	1881.0
I2 (75.00-104.50)	$3.7 \cdot 10^{-10}$	1821.9	-
I2 (72.00-83.00)	$1.3 \cdot 10^{-10}$	-	1819.5
I3 (62.00-74.00)	$5.7 \cdot 10^{-10}$	1807.4	-
I3 (63.00-71.00)	$4.2 \cdot 10^{-10}$	-	1786.9
I4 (50.00-61.00)	$6.6 \cdot 10^{-10}$	1797.4	-
I4 (50.00-62.00)	$3.3 \cdot 10^{-10}$	-	1769.2
I5 (22.50-49.00)	$>2.0 \cdot 10^{-7}$	1747.0	-
I5 (43.00-49.00)	-	-	1729.5

6 Suggested initial conditions of hydrogeological models of the Febex area

Guimera et al. (1998) presents a set of parameter values of the fracture zones etc., which will constitute the initial conditions of the numerical model, see Table 6-1. "Such parameters need to be taken with caution since they will be calibrated with the site scale model" (Guimera et al. 1998). The rock mass hydraulic conductivity is assumed to be anisotropic due to the general shistosity of the rock, the directions being z (upwards), x (approximately the drift direction) and y (normal to x).

Also the observed inflows to the KWO- and GTS tunnels at the intersections with the N and S shear zones, respectively are listed in the table. In addition, the bulk inflows to the GTS and KWO tunnels are listed. The latter flows are assumed to represent the inflows to the tunnel section between the bounding shear zones. The bulk inflows to the Febex drift are hidden to the modelling partners.

Table 6-1. Initial hydraulic parameters of the FEBEX site. T and K units in m and s. Inflows in ml/min (From Guimera et al. 1998).

Zone	Scale	Parameter	value
N shear zone	Site scale	Transmissivity	$1.1 \cdot 10^{-8}$
		Inflow in KWO-tunnel	62.5
S shear zone	Site scale	Transmissivity	$1.1 \cdot 10^{-8}$
		Inflow in GTS-tunnel	23
Shear breccia zone	Site scale	Transmissivity	$6.9 \cdot 10^{-8}$
		Inflow in FEBEX-tunnel	33.3
Lamprophyre	Site scale	Hydraulic conductivity	$2.3 \cdot 10^{-10}$
"en-echelon" fracture	Experiment scale	Transmissivity	$2.3 \cdot 10^{-9}$
Normal fracture	Experiment scale	Transmissivity	$2.3 \cdot 10^{-8}$
Rock mass, K_x	Both scales	Hydraulic conductivity	$4.6 \cdot 10^{-12}$
Rock mass, K_y	Both scales	Hydraulic conductivity	$9.2 \cdot 10^{-12}$
Rock mass, K_z	Both scales	Hydraulic conductivity	$6.9 \cdot 10^{-11}$
Bulk inflows to FEBEX drift (experiment section)			hidden
Bulk inflows to FEBEX drift (no-exp. section, no shear zone)			hidden
Bulk inflows to GTS- and KWO-tunnels			27.8

7 References

The available references (or parts thereof) for this report are listed below.

DECOVALEX III, Task 1: Modelling of FEBEX in-situ test. GENERAL SPECIFICATIONS.

Amiguet J-L (1985): Grimsel Test Site. Felsenkennwerte von intaktem Granit. Zusammenstellung felsmechanischer Laborresultate diverser granitischer Gesteine. NAGRA, NIB 85-08, Sept.1985.

Falk L, Magnusson K-Å, Olsson O, Ammann M, Keusen H and Sattel G (1988): Grimsel Test Site. Analysis of radar measurements performed at the Grimsel Rock Laboratory in October 1985. NAGRA, NTB 87-13, Feb. 1988.

Fierz T (1996): FEBEX Instrumentation of BOUS 85.001 and 85.002, FBX 95.001 and 95.002 radial boreholes. Solexperts AG, 1008, Jul. 1996.

Guimerà J, Ortuno F, Vázquez E, Ruiz B, Martínez L, Carrera J and Meier P (1996): Pulse tests at "in-drift" boreholes. Performance and evaluation. UPC, 70-UPC-L-0-1001, Sept. 1996.

Guimerà J, Carrera J, Martínez L, Vázquez E, Fierz T, Buhler C, Vives L, Meier P, Medina A, Saaltink M, Ruiz B and Pardillo J (1998): FEBEX Hydrogeological characterization and modelling. UPC, 70-UPC-M-0-1001, Jan. 1998 (Only Chapters 3.3, 3.5-3.6).

Häring M O (1996) GTS/FEBEX: Supervision and interpretation of geophysical investigations. Boreholes FBX95.001 and FBX95.002. NAGRA, NIB 96-14.

Meier P, Fernández P, Carrera J and Guimerà J (1995): FEBEX – PHASE 1. Results of hydraulic testing in boreholes FBX 95.001, FBX 95.002, BOUS 85.001 and BOUS 85.002. UPC, Dec. 1995.

Pardillo J and Campos R (1996): FEBEX – Grimsel Test Site (Switzerland). Considerations respect to fracture distribution. CIEMAT, 70-IMA-L-2-05, Mar. 1996.

Pardillo J, Campos R and Guimerà J (1997): Caracterización geológica de la zona de ensayo FEBEX (Grimsel – Suiza). CIEMAT, 70-IMA-M-2-01, May. 1997.

Schneebeli M, Fluhler H, Gimmi T, Wydler H and Läser H-P (1995): Measurements of water potential and water content in unsaturated crystalline rock. Water Resour. Res., 31(8), 1837-1843, 1995.

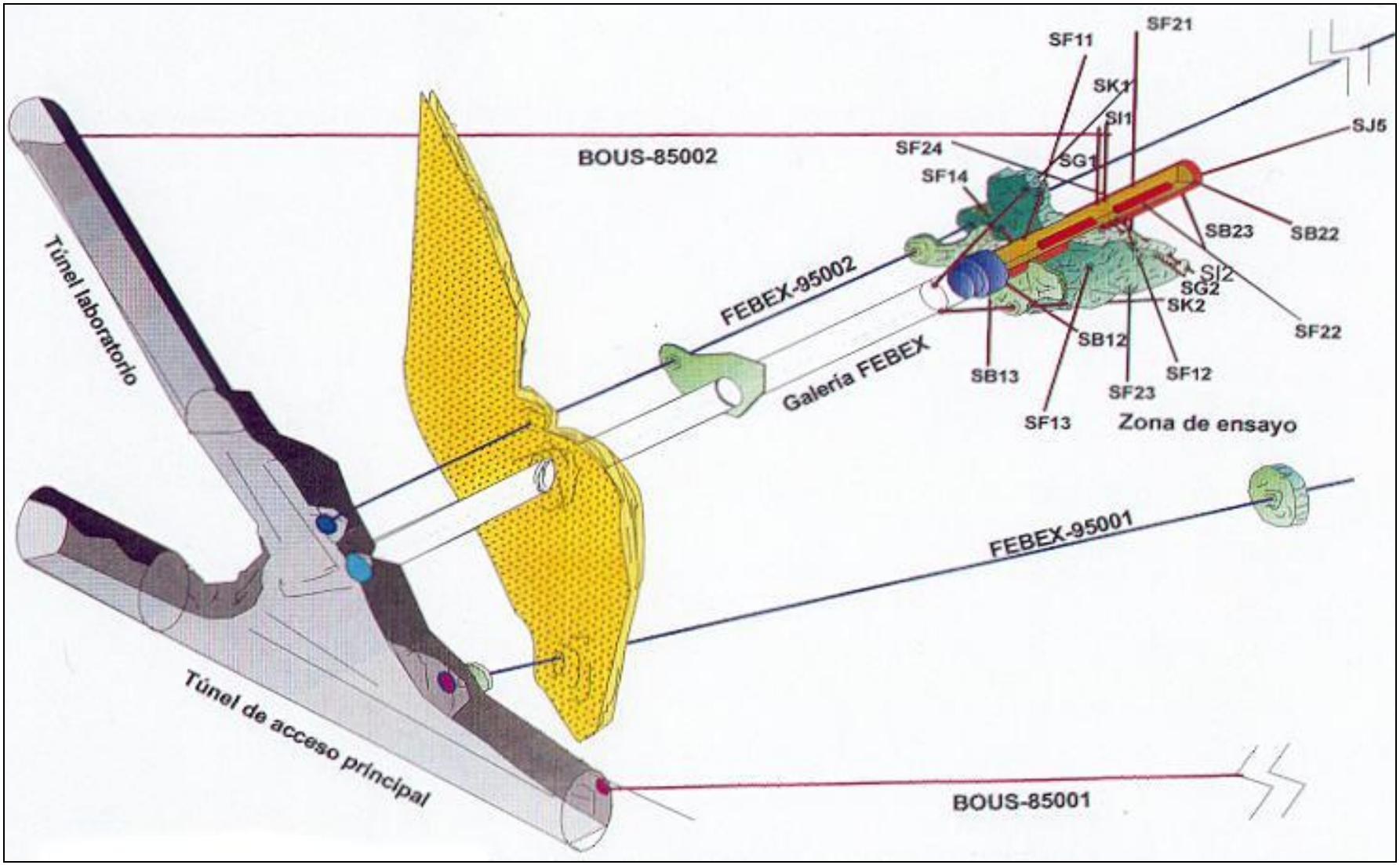

Figure 2-1. Perspective of the FEBEX drift and associated boreholes. (Pardillo et al., 1997).

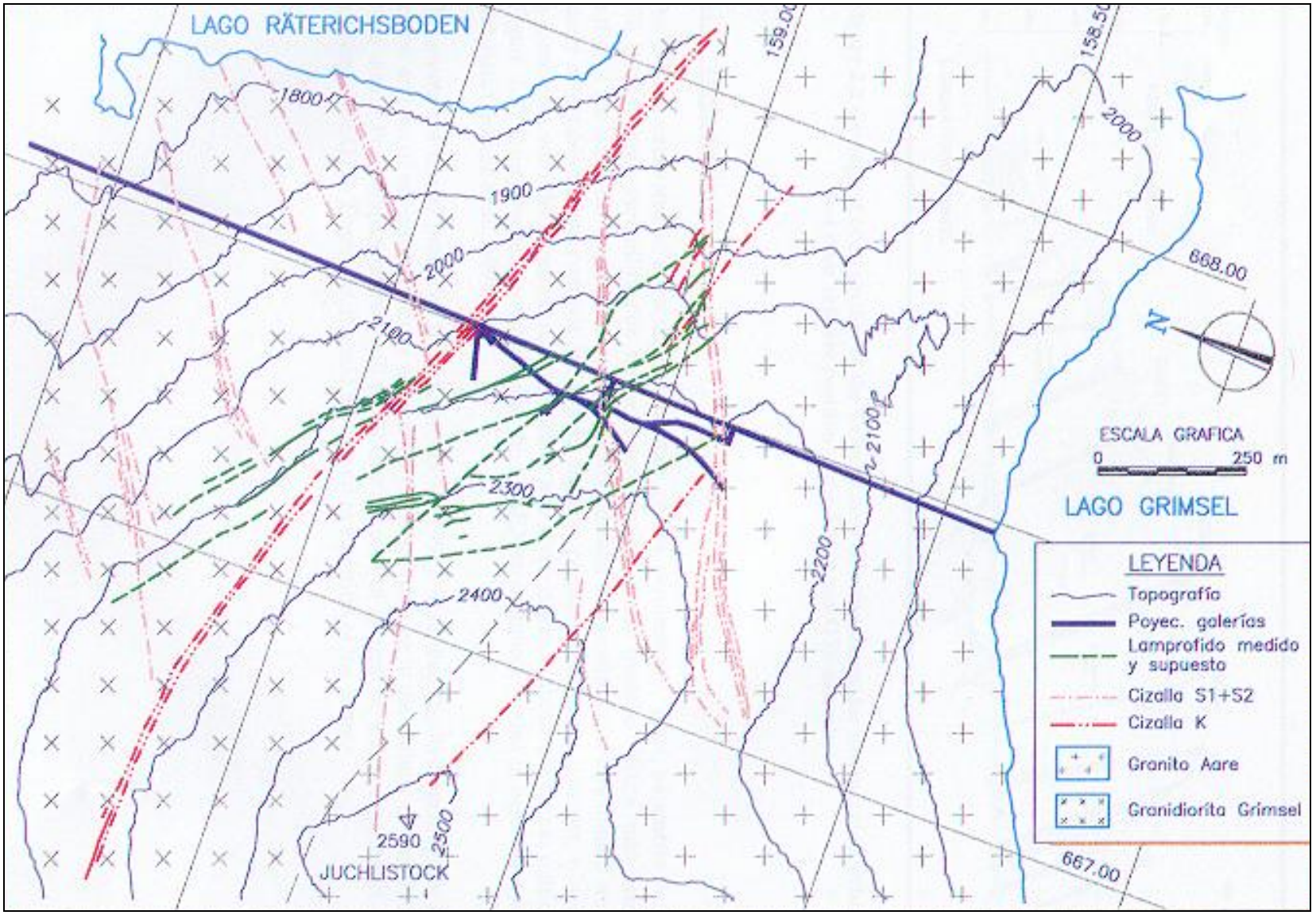

Figure 2-2. *Geological map of the Grimsel area (Guimerà et al., 1989).*

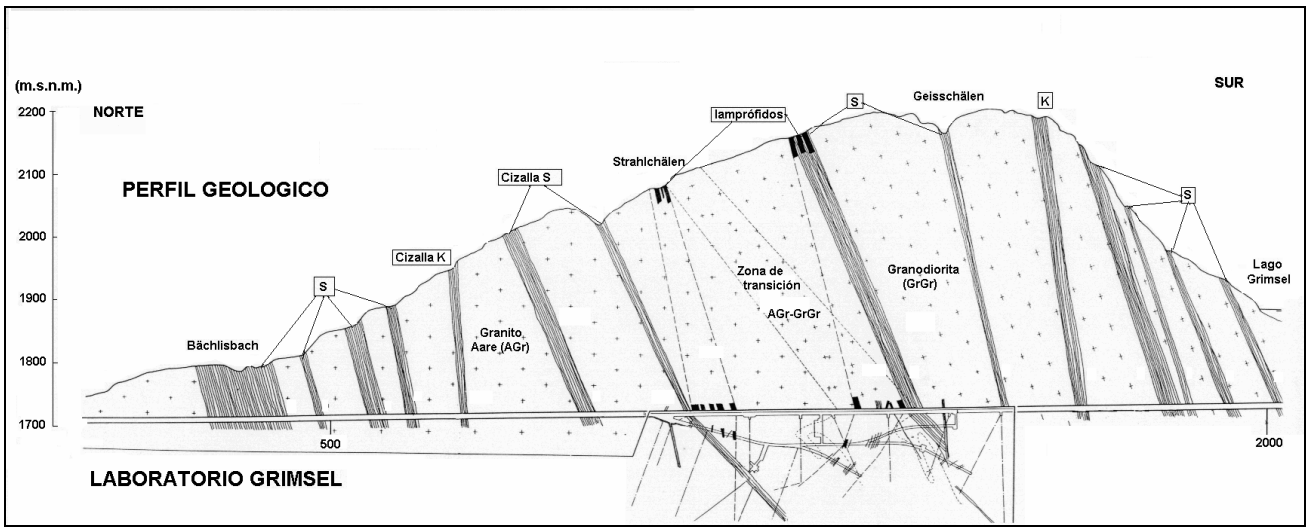

Figure 2-3. *Geological cross section of the Grimsel area showing the major geological structures and their relative position at the KWO and GTS tunnels. (Guimerà et al.,1998).*

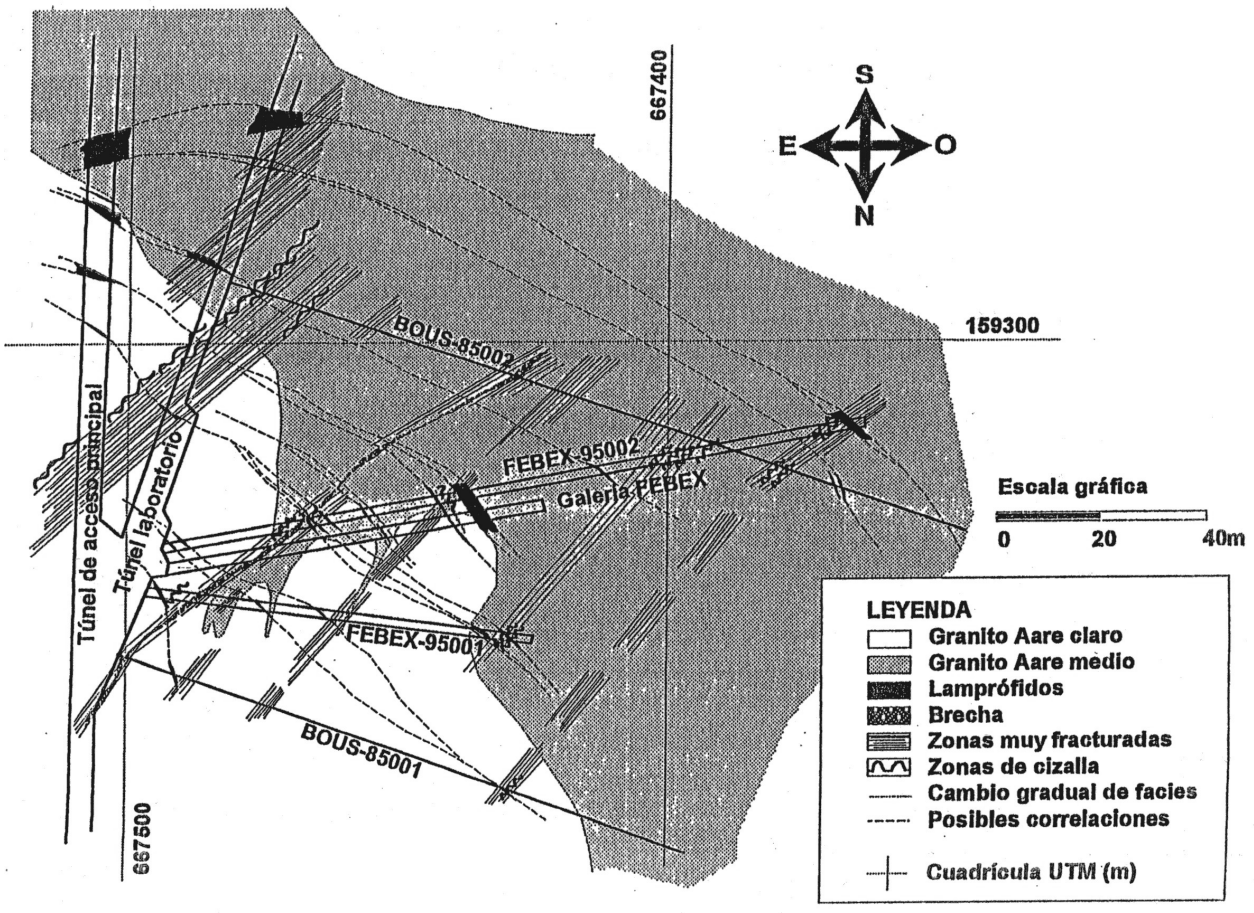

Figure 2-4. *Plan map of geological interpretation of the FEBEX area. (Pardillo et al., 1997).*

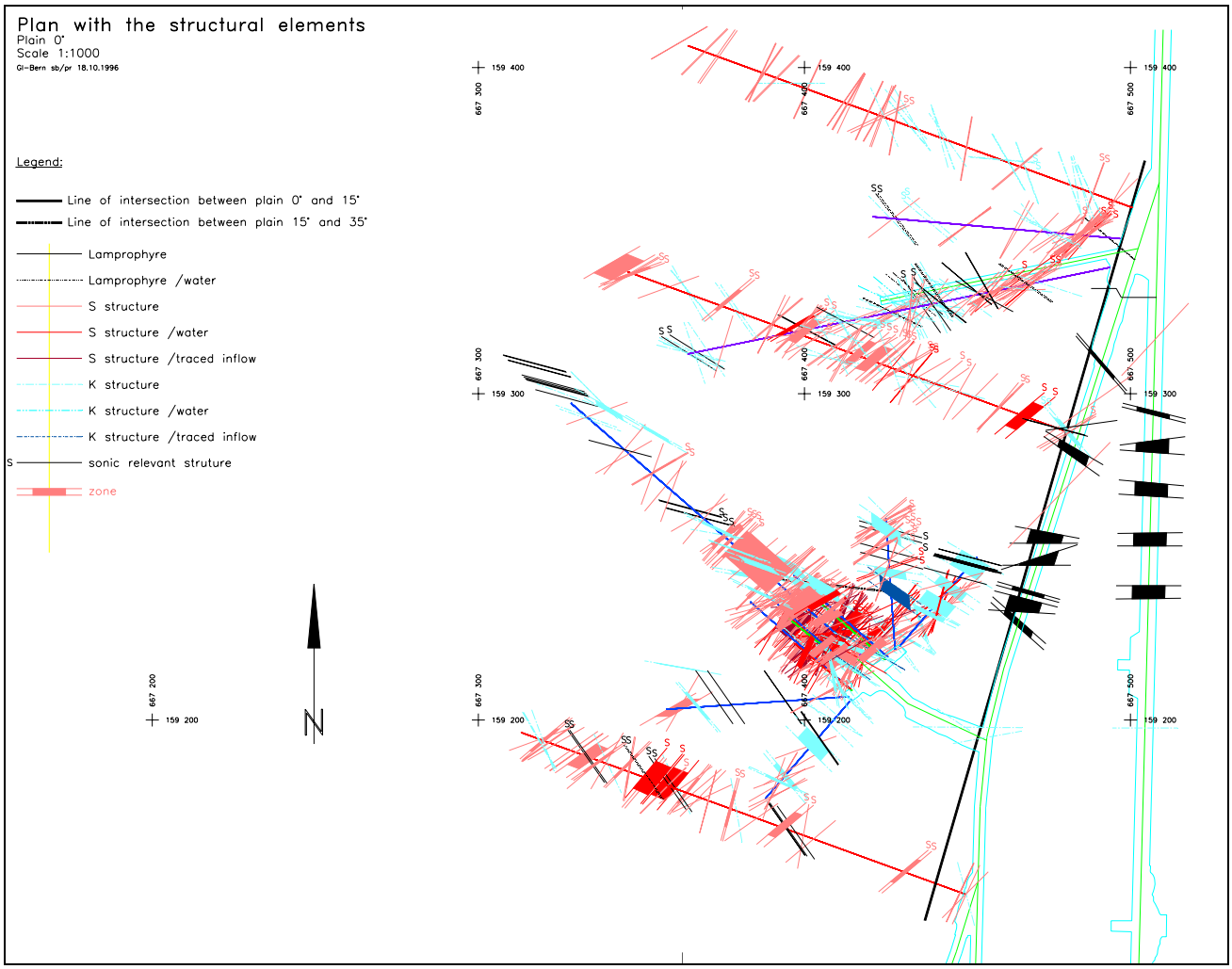

Figure 2-5. *Geological map of linear measurements and traces observed at borehole cores and tunnel walls in the BK and FEBEX areas (Guimerà et al., 1998).*

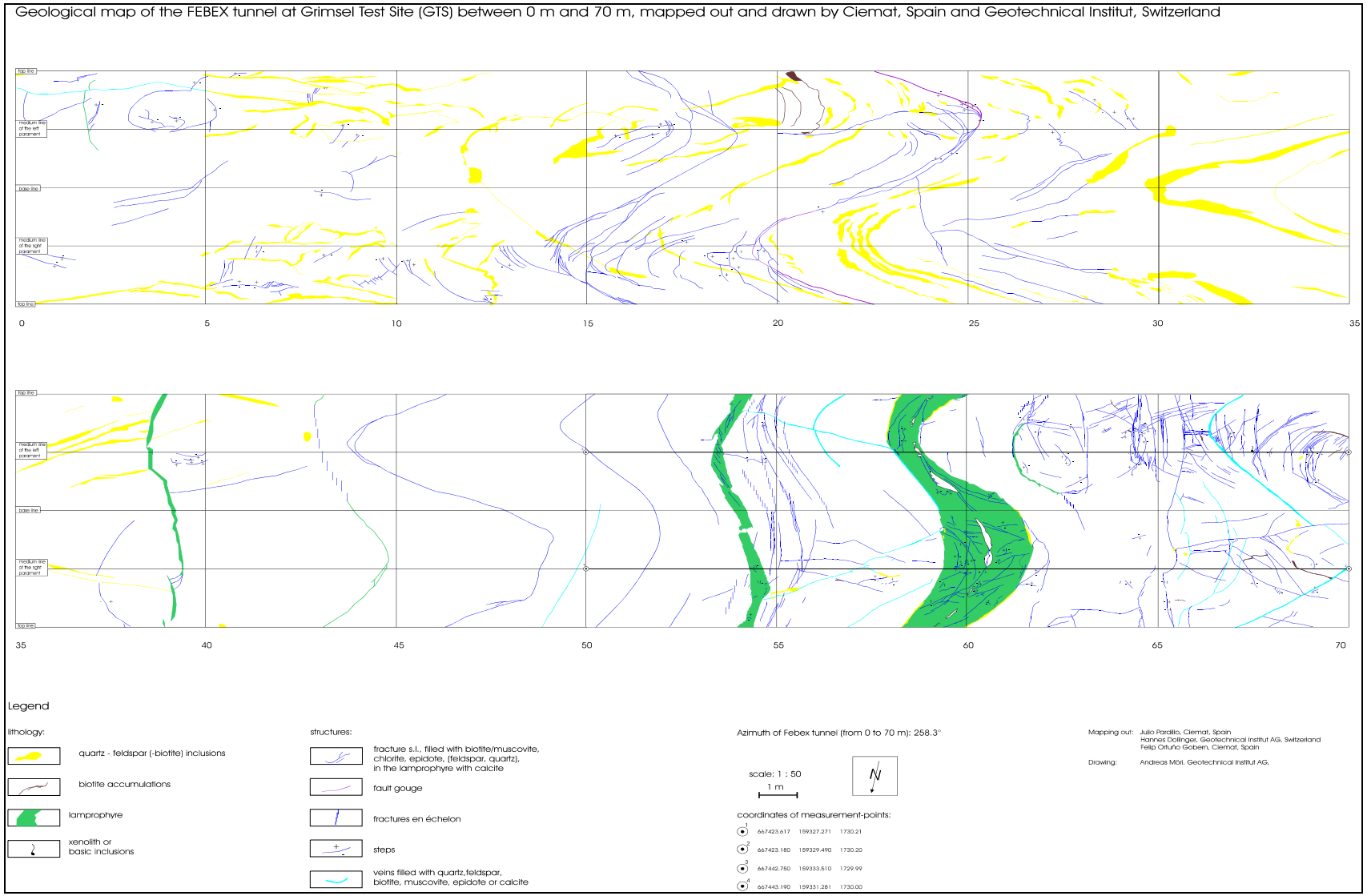

Figure 2-6. *Geological map of the FEBEX drift between 0.0 m and 70.0 m. (Pardillo et al., 1997).*

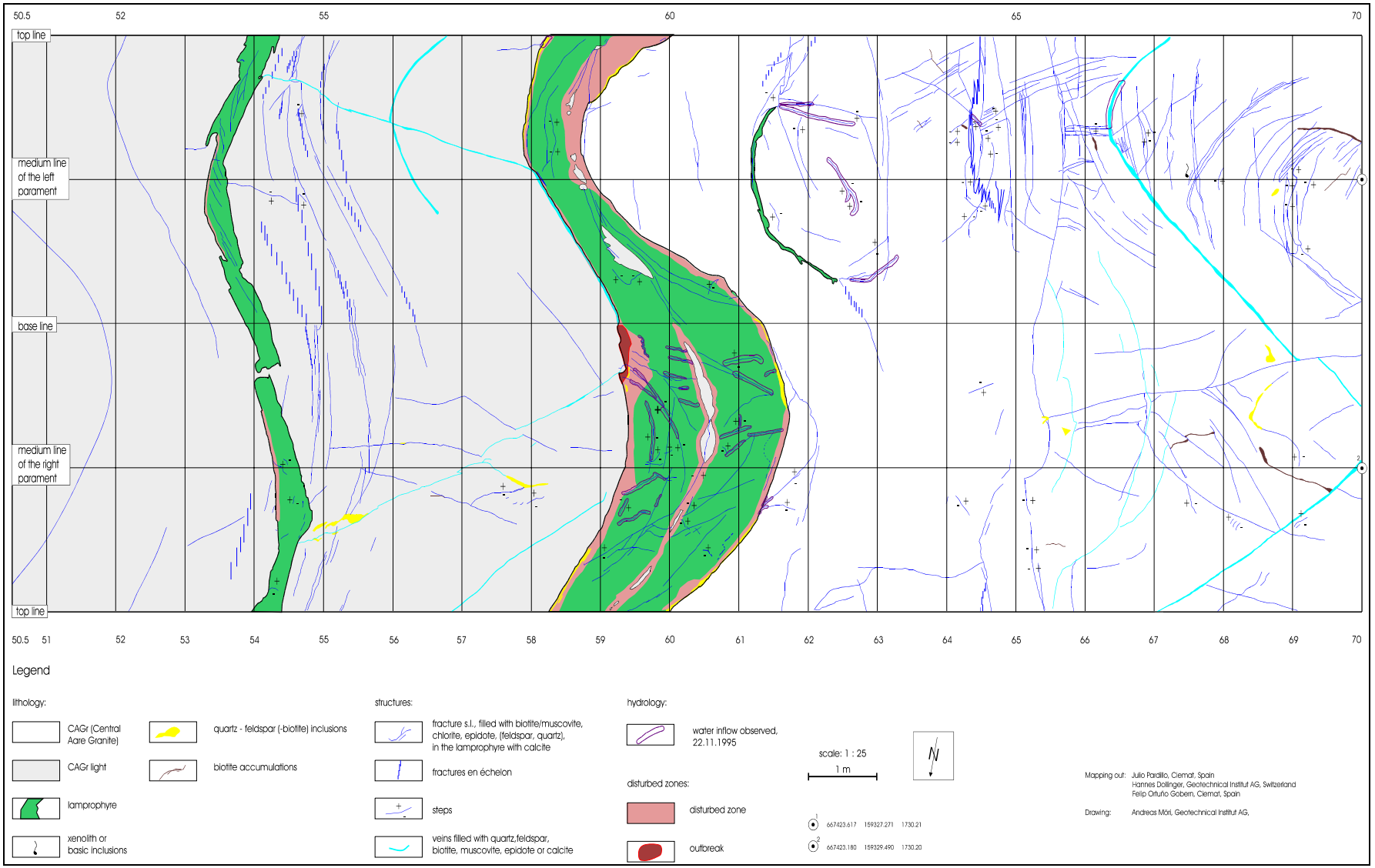

Figure 2-7. *Geological map of the FEBEX drift between 50.5 m and 70.0 m. (Pardillo et al., 1997).*

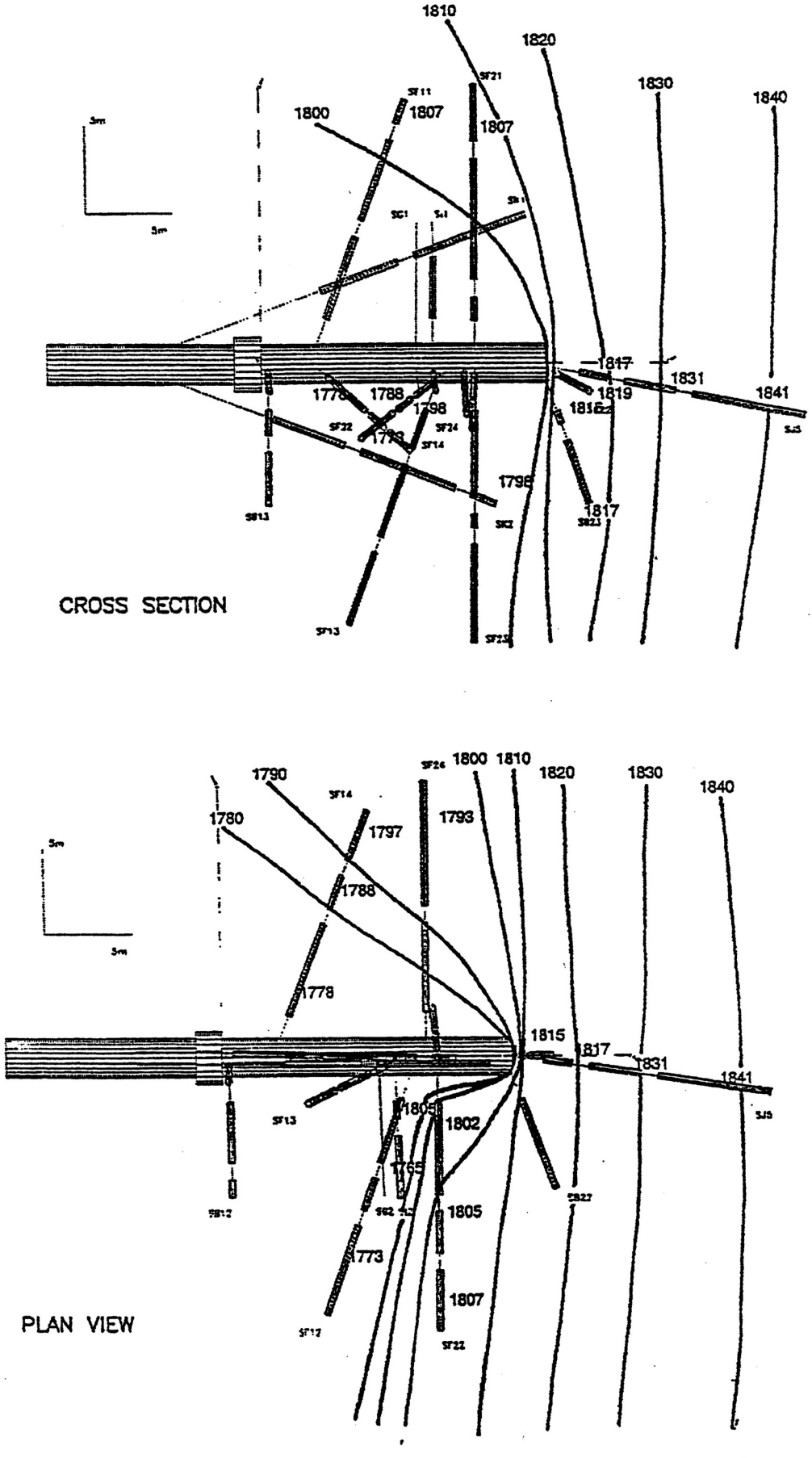

Figure 5-1. *Piezometric surface on FEBEX experiment scale. (Guimerà et al., 1998).*

FEBEX TUNNEL - Fracture zones

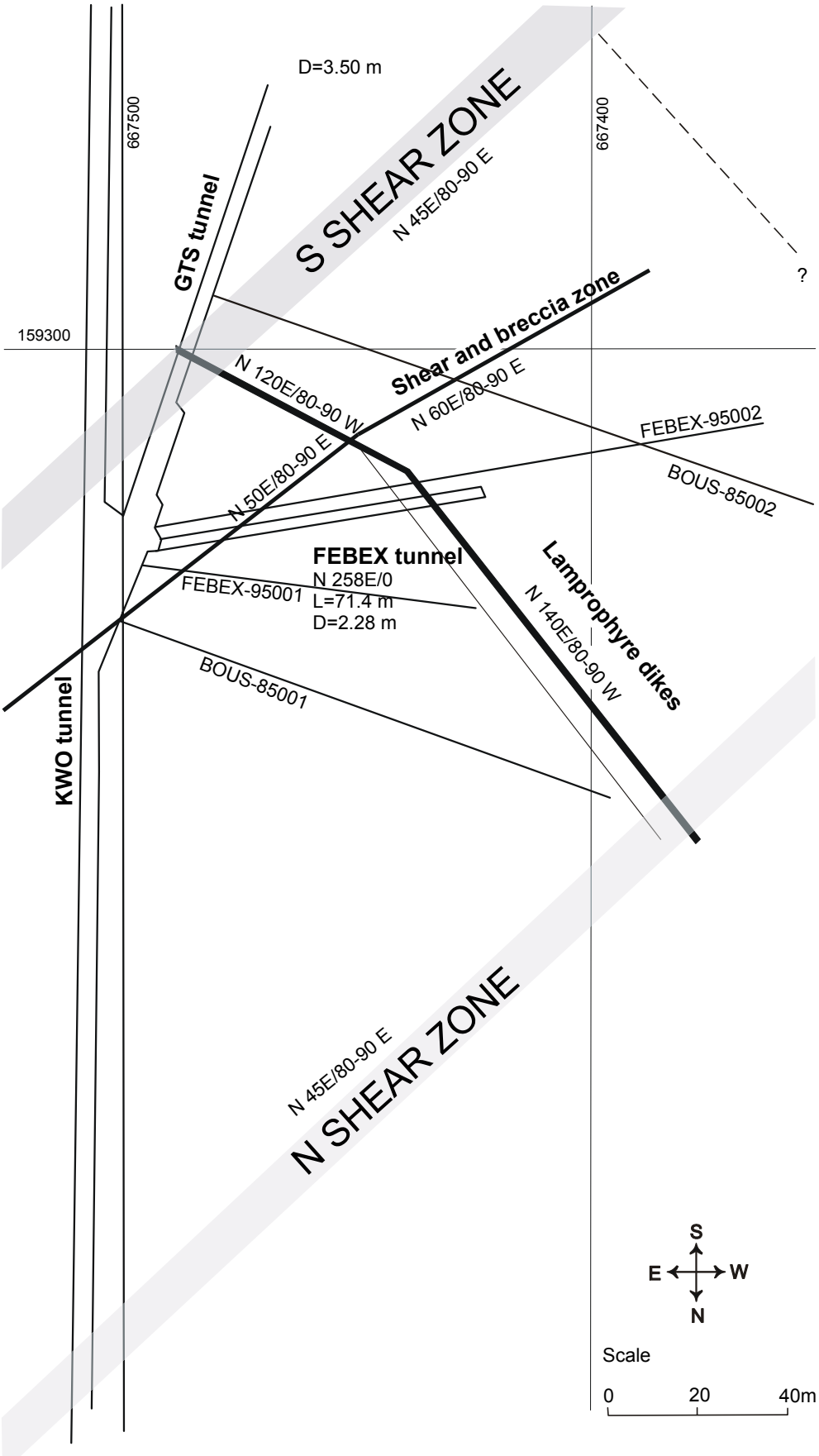

Appendix 2

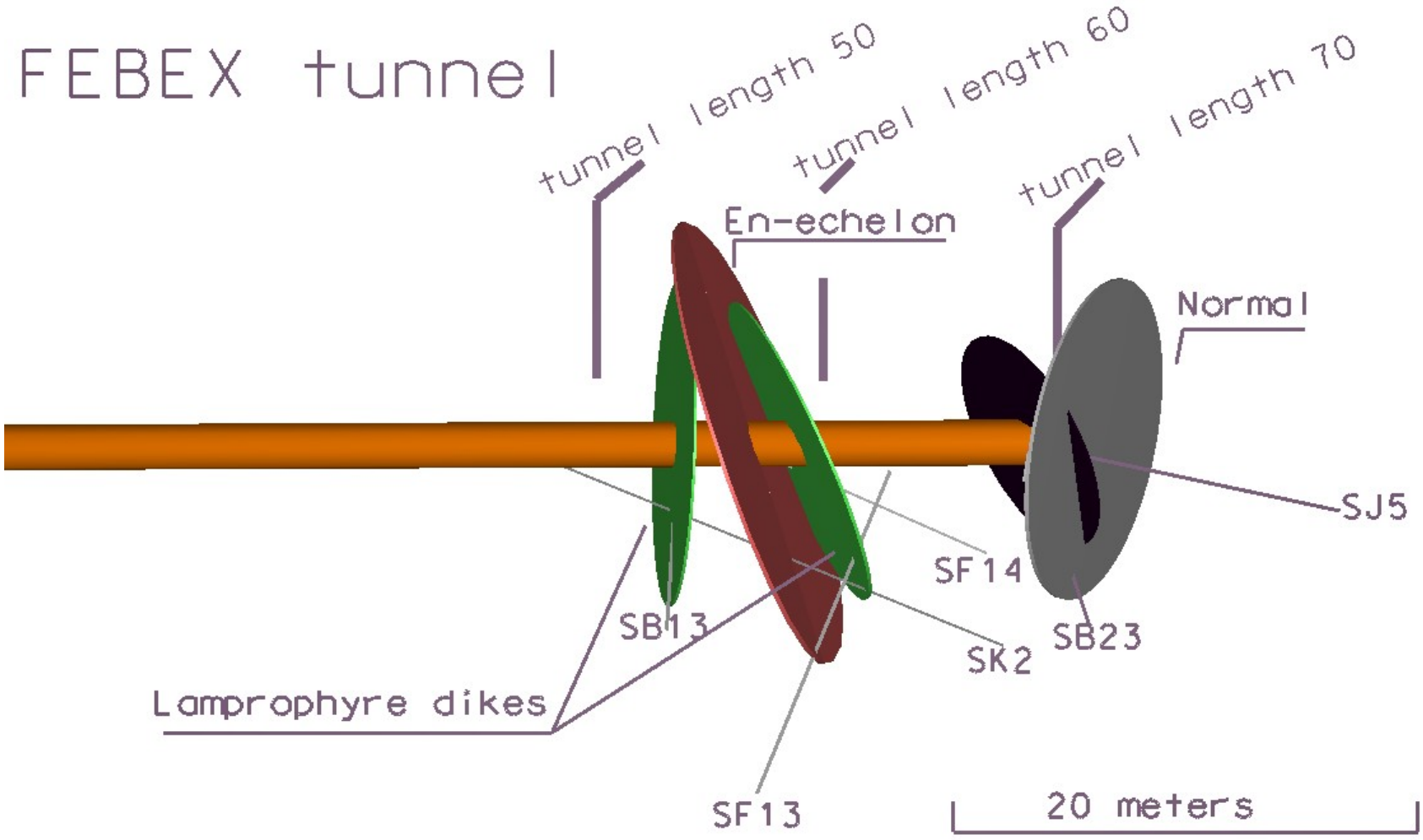
FEBEX tunnel
tunnel length 50
tunnel length 60
tunnel length 70
En-echelon
Normal
SJ5
SF14
SB13
SB23
SK2
Lamprophyre dikes
SF13
20 meters